Large Eddy Simulation of Leading Edge Film Cooling: Flow Physics, Heat Transfer, and Syngas Ash Deposition

Ali Rozati

Dissertation submitted to the faculty of the Virginia Polytechnic Institute and State University in partial fulfillment of the requirements for the degree of

Doctor of Philosophy
In
Mechanical Engineering

Committee Chair:
Dr. Danesh. K. Tafti

Committee Members:
Dr. Kenneth S. Ball
Dr. William J. Devenport
Dr. Mark R. Paul
Dr. Saad A. Ragab

December 4, 2007
Blacksburg, VA

Keywords: Large Eddy Simulation, Leading edge film cooling, Adiabatic effectiveness, Heat transfer coefficient, Blowing ratio, Deposition, Erosion, Syngas ash particle

Large Eddy Simulation of Leading Edge Film Cooling: Flow Physics, Heat Transfer, and Syngas Ash Deposition

Ali Rozati

ABSTRACT

The work presented in this dissertation is the first numerical investigation conducted to study leading edge film cooling with Large Eddy Simulation (LES). A cylindrical leading edge with a flat after-body represents the leading edge, where coolant is injected with a 30˚ compound angle. Three blowing ratios of 0.4, 0.8, and 1.2 are studied. Free-stream Reynolds number is 100,000 and coolant-to-mainstream density ratio is unity. At blowing ratio of 0.4, the effect of coolant inlet condition is investigated. Results show that the fully-turbulent coolant jet increases mixing with the mainstream in the outer shear layer but does not influence the flow dynamics in the turbulent boundary layer at the surface. As a result, the turbulent jet decreases adiabatic effectiveness but does not have a substantial effect on the heat transfer coefficient. At B.R.=0.4, three types of coherent structures are identified which consist of a primary entrainment vortex at the leeward aft-side of the coolant hole, vortex tubes at the windward side of the coolant hole, and hairpin vortices typical of turbulent boundary layers produced by the turbulent interaction of the coolant and mainstream downstream of injection. At B.R. = 0.8 and 1.2, coherent vortex tubes are no longer discernable, whereas the primary vortex structure gains in strength. In all cases, the bulk of the mixing occurs by entrainment which takes place at the leeward aft-side of the coolant jet. This region is characterized by a low pressure core and the primary entrainment vortex. Turbulent shear interaction between coolant jet and mainstream increases substantially with blowing ratio and contributes to the dilution of the coolant jet. As a result of the increased mixing in the shear layer and primary structure, adiabatic effectiveness decreases and heat transfer coefficient increases with increase in blowing ratio.

The dissertation also investigates the deposition and erosion of Syngas ash particles in the film cooled leading edge region. Three ash particle sizes of 1, 5, and 10 microns are investigated at all blowing ratios using Lagrangian dynamics. The 1 micron particles with momentum Stokes number St = 0.03 (based on approach velocity and cylinder diameter), show negligible deposition/erosion. The 10 micron particles, on the other hand with a high momentum Stokes number, St = 3, directly impinge and deposit on the surface, with blowing ratio having a minimal effect. The 5 micron particles with St=0.8, show the largest receptivity to coolant flow and blowing ratio. On a mass basis, 90% of deposited mass is from 10 micron particles, with 5 micron particles contributing the other 10%. Overall there is a slight decrease in deposited mass with increase in blowing ratio. About 0.03% of the total incoming particle energy can potentially be transferred as erosive energy to the surface and coolant hole, with contribution coming from only 5 micron particles at B.R.=0.4 and 0.8, and both 5 and 10 micron particles at B.R.=1.2.

To my parents

Acknowledgements

Current work is the outcome of the rewarding research in my graduate study and I would like to express my gratitude to my mentors, friends, and family who helped me with their advice and support during these years. I am truly and extremely grateful to my advisor, Dr. Danesh K. Tafti, without whom the success of this study would be impossible. His consistent presence in the times of need and his guidance and advice have helped me through the obstacles, improved the quality of my work, and trained me to be a successful researcher. I was privileged to have a continuous learning experience during my work under his supervision. I would also want to thank my committee members Dr. Kenneth Ball, Dr. William Devenport, Dr. Mark Paul, and Dr. Saad Ragab for their suggestions and reviews for this study.

I have been fortunate to work with the best colleagues one can hope for during these years. Special thanks to Aroon and Evan for all their help in my first years in the HPCFD lab. Also I would like to thank Shi-Ming, Anant, Pradeep, Mohammad, Keegan, Sai, Naresh, Kohei and Jose for their support and friendship. Having these friends made me look forward to coming to the lab and enjoy the work day after day.

Also many thanks to my friends in Blacksburg: Omid, Najm, Ali, Mohammad, Hooman, Nastaran, Reza, Nina, Hugh, Jonathan and many others. I have truly enjoyed their company and Blacksburg is a place with wonderful memories for me because of them.

Last, but certainly not the least, I would like to express my sincere gratitude for my family for their unconditional love and support at every stage of my life. I am grateful to my parents who are dearest to me and taught me honesty and perseverance, my brothers who have shown me how to have a keen mind and joyful life, and my grandparents who shared their wisdom with me. To them, I dedicate this work.

Table of Contents

List of Tables

List of Figures

Chapter 1 : Introduction

Gas turbine engines are widely used in aircrafts and land-based power plants and increasing their overall efficiency has been a key research topic in the turbomachinery industry. One common approach in achieving this goal is increasing the inlet temperature to the turbine section. However, due to potential damage to the blade surface, which normally has a lower melting temperature than the approaching hot gas, a number of protective measures have been developed to increase the durability of the blade and increase the lifespan of the engine. Currently, using Thermal Barrier Coatings (TBCs), and blade cooling techniques permit the increase of the turbine inlet temperature up to several hundred degrees above the blade material melting point. In general, cooling techniques fall into two categories, internal and external. Internal cooling is achieved by passing the relatively cooler bleed air from the compressor section (few hundred degrees cooler then the turbine inlet) through internal channels within the blade and removing the heat. To enhance the heat transfer in these channels, they are equipped with turbulators such as ribs and pin fins which alter the flow, increase mixing and heat transfer coefficients. The cool air then is exited into the main flow field through coolant holes distributed on the blade surface, covering it with a thin film, and preventing direct contact of the hot mainstream gas with the blade surface. Hence, external cooling is also known as film cooling.

Over past years, researchers have conducted numerous investigations on blade surface film cooling. These studies were carried out both experimentally and numerically to determine the cooling effectiveness, heat transfer coefficient, and influential parameters in improving the film cooling performance. A literature review shows that

experimental studies have been successful in measurements of film cooling effectiveness and heat transfer coefficients, but have lacked detailed flow measurements, which prevent a more comprehensive understanding of the film cooling phenomenon. With advances and developments in numerical tools and computing facilities in the last decade, Computational Fluid Dynamics (CFD) techniques have contributed to this area to compensate for the shortcomings of experimental studies. These techniques are capable of providing more detailed and comprehensive analysis of the flow physics and heat transfer mechanism, which can potentially lead to identifying important design parameters in the quest to improve the efficiency of film cooling.

As mentioned earlier, coolant holes are distributed over the entire blade surface and each surface component (blade tip, suction and pressure side, leading and trailing edge) are protected with film cooling. Optimizing the cooling effectiveness requires detailed investigation of the cooling mechanism for each component. A literature review reveals that studies on the leading edge region (which is the subject of current work) lacks such detailed data. While experimental studies are unable to provide detailed measurements of coolant-mainstream interaction near the wall which governs the cooling mechanism in this region, conventional CFD tools also fail to provide accurate and adequate data of the phenomenon. This is due to the highly complex non-canonical flow in this region with flow transition, anisotropic turbulence with secondary strains due to pressure gradients and surface curvature. Conventional CFD techniques generally use Reynolds Averaged Navier-Stokes (RANS) methods which are not capable of capturing these complex effects accurately and also do not provide the required time dependent data to analyze the dynamics of this phenomenon. On the other hand, application of Direct Numerical

Simulation (DNS) methods in this type of complex flow is prohibitive due to the computation cost. Therefore, Large Eddy Simulation (LES) technique is the most suitable tool which is more affordable compared to DNS. Application of LES minimizes the empiricism in turbulence modeling by limiting it to small and more universal scales and therefore provides accurate results when compared to RANS. Additionally, by providing access to temporal data, LES enables the dynamic analysis of the problem.

Despite the obvious advantages of LES, to date, only a few studies have applied this technique to an idealized flat plate film cooling flow. The work presented in this thesis is the first application of LES to leading edge film cooling. It is significant in that the leading edge region with compound angle injection is a challenging geometry to grid with a mesh, which maintains a high quality, to enable long term time integration. The contribution of the study is twofold; it pushes the state-of-the-art in the application of LES to a geometrically and physically complex flow, and provides unique, accurate and time dependent data of flow physics and heat transfer, which enables a much better characterization of the flow.

An additional topic of interest which is covered in this thesis deals with the use of alternate fuels based on coal gasification and the associated problem of residual ash deposition and erosion of turbine components in the hot gas path. In this context, the leading edge region is the most susceptible to damage where deposition of molten ash can block the film cooling holes and subsequently lead to failure by overheating. A literature review shows that past studies have placed *ad hoc* or field observed deposits on the blade surface or in film cooling holes and investigated the resulting effect on flow and heat transfer. There has been no study investigating the detailed dynamics of deposit

formation under representative hydrodynamic and thermal conditions in the leading edge region of a turbine blade with film cooling jets.

This thesis includes the first attempt at investigating the complex two-phase dynamics of deposition formation of residual Syngas ash particulate matter in the leading edge region of a simulated vane with film cooling. The study combines high resolution LES calculations for the carrier phase with detailed Lagrangian particle dynamics and investigates the effect of jet blowing ratio and particle size or particle Stokes number on deposition and erosion.

The dissertation includes four stand-alone journal manuscripts (in press and under review) which address the issues discussed earlier. Chapter 2 investigates the effect of the state of the coolant jet being fully turbulent versus laminar on the coolant-mainstream interaction, flow structures, adiabatic effectiveness, and heat transfer coefficient. In this article, the computational domain and boundary conditions are validated and established. Chapter 3 investigates the effects of coolant-to-mainstream blowing ratio on the flow physics and heat transfer, coherent structures, and turbulent statistics. This chapter analyzes the key parameters affecting the film cooling process. Chapter four couples the LES flow field calculation with Lagrangian particle dynamics to investigate the effects of blowing ratio and ash particle size on deposition and erosion at the leading edge with film cooling. Each chapter addresses the background, objective, problem statement, results, and conclusions of the topic being investigated.

Chapter 2 : Large-Eddy Simulations of Leading Edge Film Cooling: Analysis of Flow Structures, Effectiveness, and Heat Transfer Coefficient[1]

Abstract

A numerical investigation is conducted to study leading edge film cooling with Large Eddy Simulation (LES). The domain geometry is adopted from an experimental set-up of Ekkad et al. (1998) where turbine blade leading edge is represented by a semi-cylindrical blunt body with compound angle of injection. At blowing ratio of 0.4 and coolant to mainstream density ratio of unity, a laminar constant velocity and fully-turbulent coolant jet are studied. In both cases, the results show the existence of an asymmetric counter-rotating vortex pair in the immediate wake of the coolant jet. In addition to these primary structures, vortex tubes on the windward side of the jet are convected downstream over and to the aft- and fore-side of the counter-rotating vortex pair. All these structures play a role in the mixing of mainstream fluid with the coolant. The fully-turbulent coolant jet increases mixing with the mainstream in the outer shear layer but does not directly influence the flow dynamics in the turbulent boundary layer which forms within two coolant hole diameters of injection. As a result, the turbulent jet decreases adiabatic effectiveness but does not have a substantial effect on the heat transfer coefficient. The span-wise averaged adiabatic effectiveness agrees well with experiments for a turbulent coolant jet, without which the calculated effectiveness is over-predicted. On the other

[1] This chapter was published as an article in International Journal of Heat and Fluid Flow, "Large-Eddy Simulations of Leading Edge Film Cooling: Analysis of Flow Structures, Effectiveness, and Heat Transfer Coefficient", *in press*, Rozati, A., Tafti, D.K., Copyright Elsevier, 2007

hand, the heat transfer coefficient which is only a function of near wall turbulence, shows good agreement with experiments for both coolant jet inlet conditions.

Key words: Large Eddy Simulation, Leading edge film cooling, Adiabatic effectiveness, Heat transfer coefficient

Nomenclature

B.R.	Blowing Ratio (u_c/u_∞)
C_s	Smagorinsky constant
D	Leading edge diameter
d	Coolant hole diameter
H	Channel height
k	Thermal conductivity
L	Coolant hole length to diameter ratio
n	Normal wall distance
Nu	Nusselt number ($Nu = hD/k$)
Pr	Prandtl number ($Pr = \nu/\alpha$)
P	Spanwise pitch to hole diameter ratio
q''	Heat flux
R	Temporal autocorrelation
Re	Reynolds number ($Re = u_\infty D/\nu$)
S	Strain rate tensor
S	arc length along cylinder surface
T	Temperature
u	Cartesian velocity vector/streamwise velocity
U	Contravariant velocity vector
x	physical coordinates
θ	Nondimensional temperature ($\theta = (T-T_c)/(T_\infty-T_c)$)
ζ	computational coordinates

δ Boundary layer thickness in stagnation region

υ kinematic viscosity

τ Nondimensional time

Subscripts

aw adiabatic wall

b bulk

c coolant

t turbulent parameters

τ values based on friction velocity

∞ free stream

Superscripts

* dimensional parameter

2.1. Introduction

The overall thermal efficiency of gas turbine engines can be effectively improved by increasing the turbine inlet temperature. However, these high operative temperatures affect the durability of the blade. To prevent damage to the blades, a variety of cooling techniques have been developed. These techniques fall into two major categories; internal and external cooling. Both techniques use cold air extracted from the compressor section and pass it through channels within the blade (internal cooling), where tabulators such as ribs and pin fins are used to increase the rate of heat removal. The cooling air then is ejected into the mainstream through holes located on the leading edge, suction and pressure sides of the blade to provide a thin cold film of air which prevents the direct contact of hot gases with the blade surface (film cooling) [Han (2004)]. Although cooling

techniques increase the durability of the engine, the reduction in the operative fluid mass flow rate due to the air extraction from the compressor section is detrimental to the overall performance. This has led to numerous studies to determine factors which impact blade cooling in an attempt to optimize the process.

A considerable portion of these investigations are specific to leading edge film cooling. Due to the exposure to a high heat load, prediction of the flow field in this region is important and essential to blade durability. On the other hand the complexity of the flow field and geometry makes it complicated and difficult to study. Therefore, for the sake of simplification, many studies on the leading edge film cooling have represented the leading edge with a blunt body and a semi-cylindrical leading edge. Of the experimental studies, one can mention an early study by Mick and Mayle (1988), followed by a study of Mehendale and Han (1992), and studies by Salcudean et al. (1994), Ekkad et al. (1998), Ou and Rivir (2001), and Ekkad et al. (2004). A common conclusion from these studies is that increasing the mainstream turbulence is detrimental to film cooling effectiveness, but the negative effect is minimized at high coolant-to-mainstream blowing ratios. Heat transfer coefficient is not sensitive to mainstream turbulence but is affected significantly by coolant-to-mainstream blowing ratio. Adiabatic effectiveness is sensitive to the geometry and arrangement of the cooling holes, but overall, it decreases at high blowing ratios due to higher dispersion of the coolant and entrainment of mainstream gas between the coolant jet and blade surface due to lift off. The experimental studies of Cruse (1997), Yuki et al. (1998), and Johnston et al. (1999) used a half section of a blunt body with quarter of a cylindrical leading edge. A suction channel was located below the stagnation line to stabilize and fix the stagnation line in its

location. This experimental set up has been used to validate several numerical studies. Chernobrovkin and Lakshminarayana (1999) simulated this geometry utilizing a number of low Reynolds number k-ε models for turbulence closure. The results were in good agreement with experimental data. They identified four major vortices and explained their origins and their effects on effectiveness. Shyy et al. (1999) simulated the jets and free stream interaction around a low-Reynolds number airfoil leading edge. The SIMPLE algorithm was used with k-ε model with a low Reynolds number treatment to model the turbulence. The boundary condition at the hole exit was adopted from a previous study done by Thakur et al. (1999). Lin and Shih (2001) used Menter's k-ω shear stress transport (SST). The results were in reasonable agreement with experimental data. They identified the formation of separation bubbles caused by the hole-plenum interaction and horseshoe vortices which caused the hot gas entrainment. York and Laylek (2002a-b) used a realizable k-ε model in the Fluent code. Local and laterally averaged film cooling effectiveness was predicted but numerical results showed over-prediction in the region between the stagnation line and second row of holes when compared to the experimental data. They speculated that this discrepancy could be due to the unsteadiness about stagnation in the experiment, which was not taken into account. They also predicted the heat transfer coefficient which showed good agreement with experimental data at low blowing ratios.

In another study by Azzi and Lakehal (2001) two classes of k-ε model and Reynolds stress transport model were used to simulate both a flat plate and a symmetrical turbine blade. In the first case, a two-layer approach was used where a DNS-based one-equation model was applied in the viscous region and k-ε model was applied in the outer region. It

was found that the isotropic two-layer model under-predicted the lateral temperature distribution and resulted in lower effectiveness compared to the experimental data. To account for anisotropy effects, a factor was introduced with the eddy viscosity in the near wall one-equation model. In the second case, various quadratic and cubic explicit algebraic stress models combined with the DNS-based near wall region one-equation model were used. While the non-linear algebraic model provided somewhat better results, the best results were obtained from the two-layer method with anisotropic DNS based one–equation model in the near wall region. However, they suggested that this method needed a more refined mesh near the walls. Theodoridis et al. (2001) used a standard k-ε model with wall function to simulate a turbine blade film cooling without lateral injection. Turbulence intensity predicted in the stagnation region was not realistic. Turbulence anisotropy was found to be much less on the suction side compared to the pressure side. Applying the anisotropy correction of Bergeles et al. (1978) resulted in a much better prediction of temperature on the pressure side.

2.2. Objective of the Study

The literature review reveals that RANS models are partially successful in simulating film cooling. Eddy viscosity models under-predict the lateral spreading of the temperature field and the discrepancies with the experimental data increase at high blowing ratios. In leading edge film-cooling the additional physical complexity introduced by flow stagnation, free-stream turbulence, pressure gradients and flow acceleration, and boundary layer transition further limit the capability of RANS models as effective prediction tools. Optimizing film cooling requires a more fundamental

understanding of the phenomenon which can only be obtained by quantifying the time-dependent dynamic characteristics of flow and heat transfer. Large Eddy Simulation (LES) is capable of providing such data. The advantages of LES over RANS simulations are many, not the least among them, the elimination of the empiricism of RANS models. In spite of the need for this capability, a few studies such as Tyagi and Acharya (2003), Lui and Pletcher (2005), Iourokina and Lele (2005-2006), and Guo et al. (2006) have been conducted with LES for film cooling on a flat plate. In spite of being computationally challenging, the flat plate geometry alleviates a lot of the geometrical/meshing requirements and ensuing numerical complexities associated with leading edge film cooling. The objective of the proposed study is to push the state-of-the-art in the application of LES by extending it to leading edge film cooling to elucidate on the unsteady flow physics and heat transfer. This study investigates the effect of the coolant pipe inlet boundary condition on mixing and the resulting adiabatic effectiveness and heat transfer coefficient.

2.3. Solution Methodology

2.3.1 Computational Model and the Governing equations

The governing flow and energy equations are non-dimensionalized by a characteristic length scale which is the leading edge diameter of the cylinder (D^*), and a characteristic velocity scale given by the inlet free stream velocity (u^*_∞). Two characteristic temperature scales are incorporated: ($T^*_\infty - T^*_c$) in calculating the adiabatic effectiveness and $\frac{q''^*_w D^*}{k^*}$ in

calculating the heat transfer coefficient. The time dependent Navier-Stokes and energy equations are non-dimensionalized in transformed coordinates (Thompson et al., 1985) as:

Continuity:
$$\frac{\partial}{\partial \xi_j}\left(\sqrt{g}\overline{U}^j\right)=0 \tag{2.1}$$

Momentum:
$$\frac{\partial}{\partial t}\left(\sqrt{g}\overline{u}_i\right)+\frac{\partial}{\partial \xi_j}\left(\sqrt{g}\overline{U}^j\overline{u}_i\right)=-\frac{\partial}{\partial \xi_j}\left(\sqrt{g}(\vec{a}^j)_i\overline{p}\right)+\frac{\partial}{\partial \xi_j}\left(\left(\frac{1}{\mathrm{Re}}+\frac{1}{\mathrm{Re}_t}\right)\sqrt{g}g^{jk}\frac{\partial \overline{u}_i}{\partial \xi_k}\right) \tag{2.2}$$

Energy:
$$\frac{\partial}{\partial t}\left(\sqrt{g}\overline{\theta}\right)+\frac{\partial}{\partial \xi_j}\left(\sqrt{g}\overline{U}^j\overline{\theta}\right)=\frac{\partial}{\partial \xi_j}\left(\left(\frac{1}{\mathrm{Pr}\,\mathrm{Re}}+\frac{1}{\mathrm{Pr}_t\,\mathrm{Re}_t}\right)\sqrt{g}g^{jk}\frac{\partial \overline{\theta}}{\partial \xi_k}\right) \tag{2.3}$$

where $\vec{a}^i$ are the contravariant basis vectors[2], $\sqrt{g}$ is the Jacobian of the transformation, g^{ij} is the contravariant metric tensor, $\sqrt{g}U^j=\sqrt{g}(\vec{a}^j)_i u_i$ is the contravariant flux vector, u_i is the Cartesian velocity vector, and θ is the non-dimensional temperature.

The overbar in the continuity, momentum and energy equations denote grid filtered quantities. Re_t is the inverse of the non-dimensional turbulent eddy-viscosity and is obtained by the Smagorinsky model

$$\frac{1}{\mathrm{Re}_t}=C_s^2(\sqrt{g})^{2/3}\left|\overline{S}\right| \tag{2.4}$$

where $\left|\overline{S}\right|$ is the magnitude of the strain rate tensor given by $\left|\overline{S}\right|=\sqrt{2\overline{S_{ik}}\,\overline{S_{ik}}}$. The Smagorinsky constant C_s^2 is obtained via the dynamic procedure [Germano et al.

[2] The notation $\left(\vec{a}^j\right)_i$ is used to denote the *i-th* component of vector $\vec{a}^j$, $(\vec{a}^j)_i=\partial\xi_j/\partial x_i$

(1991)]. The turbulent Prandtl number is assumed to have a constant value of 0.5 [Moin et al. (1991)].

2.3.2 Numerical Method

The governing equations for momentum and energy are discretized with a conservative finite-volume formulation using a second-order central difference scheme on a non-staggered grid topology. The Cartesian velocities, pressure, and temperature are calculated and stored at the cell center, whereas contravariant fluxes are stored and calculated at the cell faces. A projection method is used for time integration. The temporal advancement is performed in two steps, a predictor step, which calculates an intermediate velocity field, and a corrector step, which calculates the updated velocity at the new time step by satisfying discrete continuity.

The computer program GenIDLEST (Generalized Incompressible Direct and Large-Eddy Simulations of Turbulence) used for these simulations has been applied extensively to study flow and heat transfer in stationary and rotating internal ducts, heat exchangers, etc. [Abdel-Wahab and Tafti (2004), Sewell and Tafti (2006-2007), Cui and Tafti (2002), Tafti and Cui (2003)]. Details about the algorithm, functionality, and capabilities of GenIDLEST can be found in Tafti (2001).

2.3.3 Experimental and computational geometries

The geometry is adopted from the experimental set up of Ekkad et al. (1998), where a cylinder (with a tailboard placed at the rear) represents the leading edge. Two rows of cooling holes are located ±15˚ from the stagnation line, each containing ten holes. The holes are at 30˚ and 90˚ inclination with span-wise and stream-wise direction,

respectively. Based on the characteristic length scale of cylinder diameter D^* (7.62cm), the channel height H^*/D^* = 10.0, hole diameter d^*/D^* = 0.063, hole length to diameter ratio L^*/d^* = 3.1, and span-wise pitch to hole diameter ratio P^*/d^* = 4.0 specifies the computational geometry. Detailed specifics of the test model can be found in Ekkad et al. (1998).

In the current paper two computational domains are used to represent this model. They are referred to as D-I and D-II from this point forward (see Figure 2.1). D-I has the dimension of 10×10×0.252 with the cylinder centered at (0,0,0). This domain has two rows of coolant holes on either side of stagnation. D-II is exactly half of the first domain, where a symmetry boundary condition is assumed along the stagnation line. In both, the tailboard is replaced by a flat after body, to alleviate the unnecessary complications which arise due to flow separation in the wake of the cylinder. This change is not expected to adversely affect comparisons with experimental data in the near field of coolant injection.

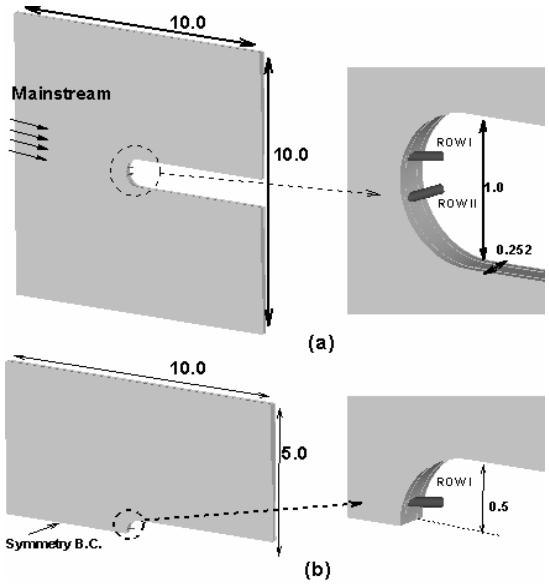

Figure 2.1 - Computational domains (a) D-I, (b) D-II

2.3.4 Flow and boundary conditions

The mainstream Reynolds number is 100,000 based on the cylinder diameter and mainstream velocity. Coolant to mainstream density ratio is assumed to be unity, as in the experiment. In the current study a blowing ratio of B.R. = 0.4 is applied. The mainstream inlet condition is a constant velocity profile (u_∞) with no free-stream turbulence (experiments had a nominal Tu=0.5%) and a convective outflow condition is applied.

Two different coolant pipe inlet conditions are tested. First a Constant Velocity Profile (CVP) with a value of 0.4 at the coolant pipe inlet (which gives a blowing ratio of 0.4) in the direction of the coolant pipe axis is applied. Second, the coolant pipe inlet assumes a time–dependent Turbulent Velocity Profile (TVP), which is obtained from an auxiliary fully developed turbulent pipe flow LES. The simulation results with CVP are used for comparison between domains D-I and D-II. Afterward, both pipe inlet conditions are applied to domain D-II to study their effects on the film cooling phenomenon.

On the outer channel walls, wall boundary conditions with zero heat flux are assumed. In calculating the adiabatic effectiveness, an adiabatic condition is imposed on the blade surface. With non-dimensional temperature defined as $\theta = \dfrac{T^* - T_c^*}{T_\infty^* - T_c^*}$, the coolant and mainstream temperatures are denoted by 0 and 1, respectively. In calculating the heat transfer coefficient, a constant non-dimensional heat flux of unity is imposed on the cylinder surface and the mainstream and coolant temperatures – here non-dimensionalized with $\dfrac{q_w''^* D^*}{k^*}$ – are set to zero. These selected conditions are consistent with the experimental conditions. As mentioned earlier, a symmetry boundary condition is imposed along the stagnation line for domain D-II.

In the current study we choose not to place a plenum (which would be computationally simpler) in order to have greater control and definition over the jet inlet conditions, both in the mean flow distribution and turbulent characteristics. For the second set of calculations with a time-dependent turbulent inlet profile, it is implicitly assumed that the coolant hole is sufficiently long for the flow to exhibit a fully-developed turbulent flow at the location where the inlet boundary condition is applied.

2.3.5 Fully developed time dependent turbulent coolant inlet boundary condition

Turbulent inflow conditions for the cooling pipe inlet uses scaled data from auxiliary simulations in a fully-developed pipe flow at an equivalent coolant jet Reynolds number. The auxiliary pipe flow simulations are carried out separately and validated with the experimental data of den Toonder et al. (1997). The pipe diameter is selected as the characteristic length scale and the pipe length is π. The grid consists of five blocks with a total resolution of 32×32×32×5 cells and has the same cross-sectional distribution and resolution as the coolant pipe, which provides 4-5 grid points in the distance of $y^+ = 10$ at the Reynolds number of 6,200 based on pipe diameter and bulk velocity of the flow.

Figure 2.2 shows the comparison of calculated and experimental stream-wise mean velocity and RMS fluctuation plotted in wall-coordinates in a fully-developed pipe flow at a bulk Reynolds number of 6,200 with available experimental data at 4,900 and 10,000 (and also 17,800 for mean velocity). Agreement with the experimental data is good, in spite of a relative coarse grid used in the cross-section, which was limited by the permissible resolution in the main simulation. For further validation of the results' accuracy, the calculated friction coefficient was compared to the Petukhov correlation for fully developed flows [Petukhov et al. (1970)] as:

$$f = 0.25\left(0.790\ln \mathrm{Re}_D - 1.64\right)^{-2} \qquad 3000 \le \mathrm{Re}_D \le 5\times10^6 \tag{2.5}$$

Results obtained from the simulation and correlation are 9.438×10^{-3} and 9.008×10^{-3}, respectively.

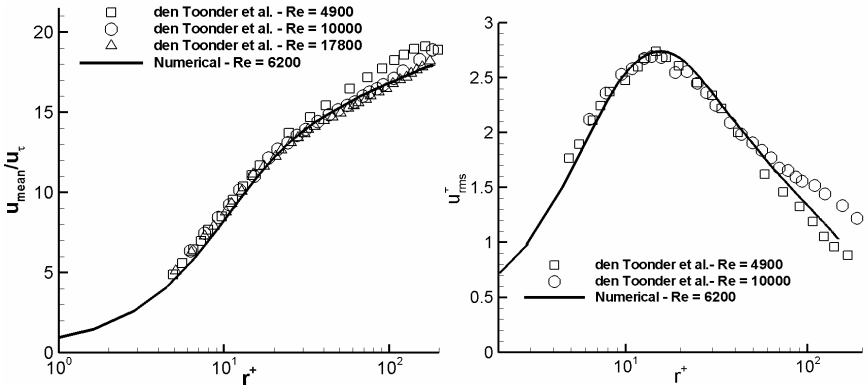

Figure 2.2 - Mean profile and turbulent statistics in an auxiliary turbulent pipe flow simulation. Numerical results are compared to experimental data of den Toonder et al.

A finite number of stored time-dependent frames from this auxiliary calculation are cycled at the inlet plane of the coolant pipe in the main simulation. To calculate the suitable number of frames, autocorrelations for the three velocity components (u,v, and w) are evaluated at the center of the pipe. As shown in Figure 2.3, the autocorrelation quickly falls to zero for all three velocity components within a non-dimensional time unit of 0.1. However, the turbulent signal in this time span does not give adequate resolution over a range of frequencies. Hence frames were stored for one non-dimensional time unit (50,000 frames) to represent the turbulence at the inlet to the coolant hole. The last 1,000 frames act as a buffer and are modified such that the last frame of one cycle correlates with the first frame of the next cycle. This ensures a smooth transition between the two cycles.

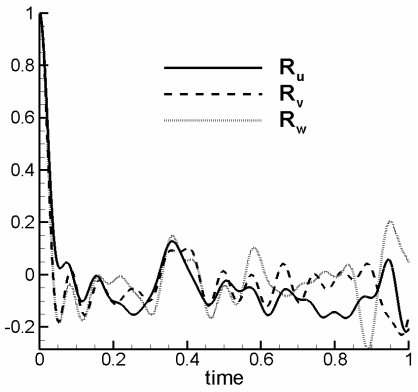

Figure 2.3 - Temporal autocorrelation for velocity components

Once the frames are calculated and stored, a transformation matrix is used to scale the velocity components according to the blowing ratio and align the resultant velocity vector with the coolant pipe axis. The scaling factor used is the velocity ratio between the coolant velocity and pipe flow mean velocity ($u_c/u_{mean,pipe}$). Figure 2.4 shows the effect of the inlet conditions CVP and TVP on the mean profile of the axial velocity in the coolant jet and turbulent kinetic energy at the exit plane of the coolant pipe. It is noted that the outward flow to the surface is negative by virtue of its direction, hence, the positive velocities at the windward side of the coolant hole indicate penetration of the mainstream flow into the coolant pipe, which is estimated to be about 0.3d for both cases. The infiltration of the mainstream into the coolant pipe pushes the coolant to the aft-leeward side of the hole from which it ejects with a high velocity. The exit mean profiles between the two pipe inlet conditions are similar, except for some differences near the windward side.

The exit distribution of Turbulent Kinetic Energy (T.K.E.) is noticeably different between the two cases. The T.K.E. at the exit is higher in case of TVP than it is for CVP.

The maximum T.K.E. increases up to 15% for TVP with higher values in the rest of the exit plane, versus 10% for the CVP condition.

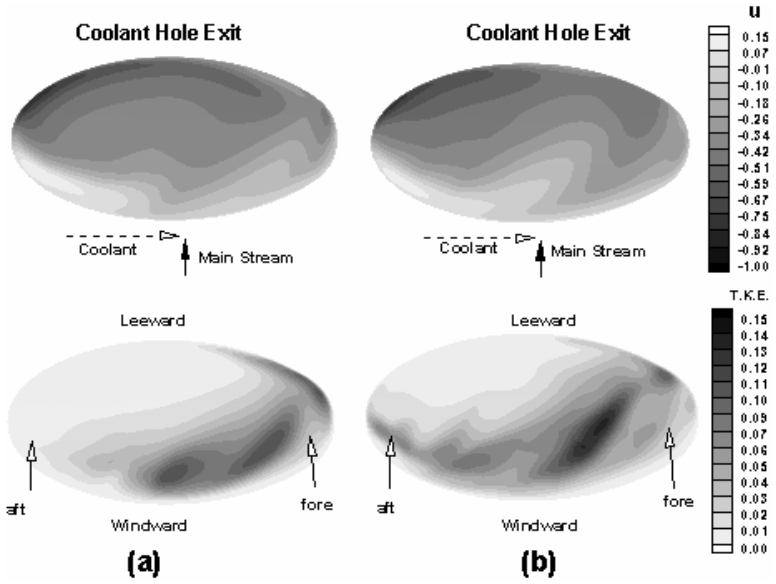

Figure 2.4 - Mean axial velocity and turbulent kinetic energy at exit plane of coolant pipe for (a) CVP and (b) TVP conditions

2.3.6 Grid properties

The complex geometry at the leading edge needs to be meshed with a high quality grid, with minimal skewness and discontinuities in grid size to maintain a good quality solution and prevent numerical instabilities from developing during time-integration. A factor which has a large influence on the grid generation process is the large variation in turbulent length scales between the coolant and external flow. Based on an external Reynolds number of 100,000, d^*/D^* = 0.063, and a blowing ratio of 0.4, the viscous length scale associated with near wall turbulence in the cooling jet is of $O(1\times10^{-3}d^*)$, whereas the external geometrical length scale is of $O(D^*)$, both of which have to be reconciled in the grid generation process.

The complex leading edge geometry is meshed by using a multiblock framework. While each block has a structured body-fitted mesh, an unstructured block topology is utilized. This method provides the flexibility of unstructured meshes with the good physical and computational properties of structured meshes. A multi-block grid, generated with Gridgen 15.07, consists of 124 blocks with 6,422,528 cells for domain D-I and 62 blocks with 3,211,264 cells for domain D-II. A non-conformal interface approach is used to relax the grid requirements far from the cylinder surface.

The grid resolution is tested *a-posteriori* by using the calculated local shear stress to find $y^+=yu_\tau/\nu$. The distribution of y^+ shows that the condition of $y_1^+<1$ is satisfied on the entire cylinder surface. Results also show that approximately 45 grid points lie within the boundary of coolant-mainstream interaction downstream of the coolant hole [Rozati and Tafti (2007)]. It is noteworthy that the resolution and grid spacing for domain D-II is identical with the upper half of domain D-I. Therefore, the justifying arguments on grid resolution for domain D-I are perfectly applicable for the second domain (D-II) as well.

2.4. Results and Discussion

The calculation was carried out on Virginia Tech's Terascale computing facility, SystemX, on 2.3 GHz PowerPC 970FX processors (124 and 62 processors for domains D-I and D-II, respectively). The non-dimensional time step was set to 3×10^{-5} and 2×10^{-5} for CVP and TVP conditions, respectively. Each time step took approximately 4.5*s* of wall clock time. The flow is allowed to develop for approximately 3 time units before sampling and averaging to obtain mean quantities is activated. Probes at various locations

in the jet and downstream of injection are monitored to estimate the time evolution of the flow.

2.4.1 Stagnation line dynamics

During the course of the computations with domain D-I, it was found that the stagnation line did not remain stationary at the center but moved for both coolant inlet conditions. Figure 2.5 shows the time evolution of the stagnation line for the two cases studied. The motion of the stagnation line is more gradual with the CVP condition than with the TVP condition, which is consistent with the fact that the TVP at the coolant inlet introduces more asymmetries into the calculation because of the turbulent nature of the jet. It is noted that the physical time during which this happens is less than 27 ms from startup, and could be a transient with the stagnation line returning to its location at steady state. The other possibility which cannot be discounted is that the stagnation line oscillates even after steady state is reached. In either case, to resolve this motion, which is on a much longer time scale than the turbulent time scale of jet-mainstream interaction (and is of primary interest in this study), would be prohibitively expensive.

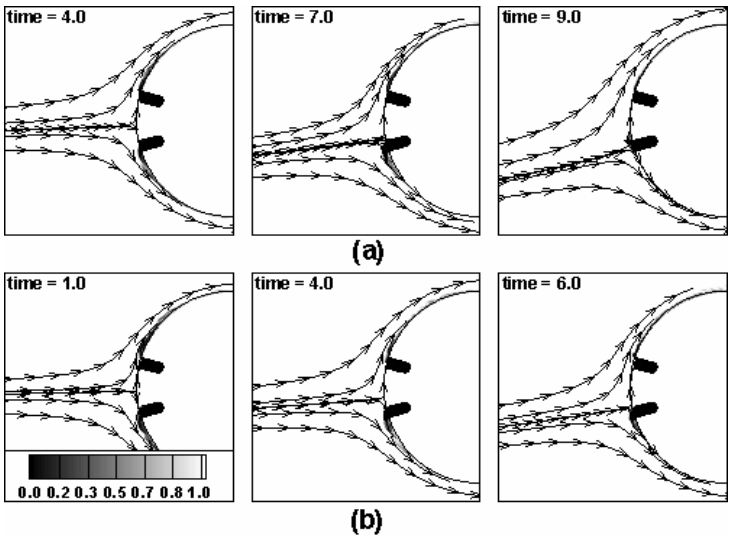

Figure 2.5 - Unsteadiness of stagnation line with (a) CVP and (b) TVP conditions

Many experimental studies have used a modified geometry, which only includes one half of the cylindrical leading edge with a suction slot to bleed-off the boundary layer and control the location of the stagnation line [Cruse (1997), Yuki et al. (1998), and Johnston et al. (1999)]. In doing this, an implicit assumption made is that the behavior of the coolant mainstream interaction pertinent to the adiabatic effectiveness and heat transfer coefficient on one side is unaffected by the dynamics on the other side. The same tact is followed in this study by assuming symmetry along the stagnation line (domain D-II).

To validate this assumption, the cross correlation between the flow field generated by the two jets is studied to assure that elimination of the bottom coolant row does not affect the characteristics of the top coolant row. Figure 2.6 shows the locations at which the flow is monitored. All points shown in Figure 2.6 are located at the jet centerline plane (z=0) and distributed downstream of the coolant hole as follows: P-1 and P-5 at s/d = 0, P-2 and P-6 at s/d = 1.25, P-3 and P-7 at s/d = 2.22, P-4 and P-8 at s/d = 3.75, and P-9 at s/d = 6.1. In domain D-I the same distribution of monitored points lies downstream of the

bottom coolant hole. While some of the points lie in the near wall region inside the turbulent boundary layer that develops after injection, others lie at the outer boundary of coolant-mainstream interaction. The cross correlation is calculated from: $R = \frac{\overline{u_1' u_2'}}{u_{rms1} u_{rms2}}$, where *1*, and *2* correspond to the top and bottom half of the cylinder, respectively.

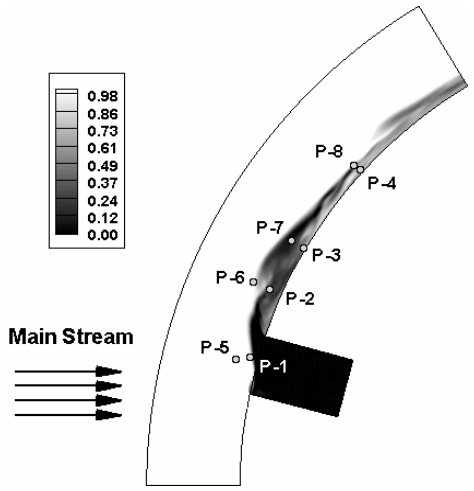

Figure 2.6 - Location of the monitored points downstream of the coolant hole. Temperature contours are shown

Table 2.1 shows the values of cross-correlation between the velocity components. Considering the full spectrum of results obtained over all the points, we can draw the conclusion that the generated turbulent fields have a very weak correlation between the two sides. Therefore, in the current study, a symmetric boundary condition along the stagnation line is imposed as described by domain D-II. The imposition of the symmetry boundary is further validated *a-posteriori* by comparing some key mean results obtained in D-II with D-I with the CVP coolant inlet condition. Comparisons of mean temperature and velocity profiles, adiabatic effectiveness and turbulent quantities validate that domain D-II is a good approximation to D-I.

Table 2.1 – Cross correlation between the two halves of Domain D-I

Probe #	Cross correlation of *u* fluctuation	Cross correlation of *v* fluctuation	Cross correlation of *w* fluctuation
1	0.1077	0.0430	0.0901
2	-0.1537	0.0604	-0.0684
3	0.0113	0.2338	0.0617
6	-0.0013	0.2009	0.2401
7	-0.0351	-0.1030	-0.0267
8	0.0673	-0.1506	0.0506

2.4.2 Turbulent Flow Features

The signal characteristics between D-I and D-II for CVP are compared at three selected locations (P-1, 4, and 8) in Figure 2.7. This figure shows the turbulent characteristics in the flow downstream of the coolant hole by presenting the stream-wise velocity fluctuations. Probes are placed near the surface to resolve the developing turbulent boundary layer and at the outer boundary of the shear layer resulting from the coolant-mainstream interaction (see Figure 2.6 for locations). Qualitatively, the signals exhibit the same unsteady characteristics between the two domains. The effect of the unsteady stagnation line is observed in domain D-I at P-1 and P-8 which is located in the jet-mainstream shear layer away from the surface. At time t = 4, the stagnation line starts to move towards the bottom coolant hole row, resulting in additional acceleration of the stream-wise velocity on the top section of the leading edge.

Flow development is also analyzed by study the stream-wise velocity fluctuations downstream of injection. At the hole center, P-1 characterizes the jet-mainstream interaction. As the coolant reaches 1.25 hole diameter downstream (P-2) from the hole center, the flow exhibits a strong turbulent behavior near the surface, which signals the development of a turbulent boundary layer. As the flow moves further downstream, the

stream-wise velocity accelerates and the intensity of the fluctuations decreases for P-3 and P-4.compared to P-2. Farther from the surface, one can observe the development of a turbulent shear layer between the coolant and mainstream (P-5, 6, 7, and 8).

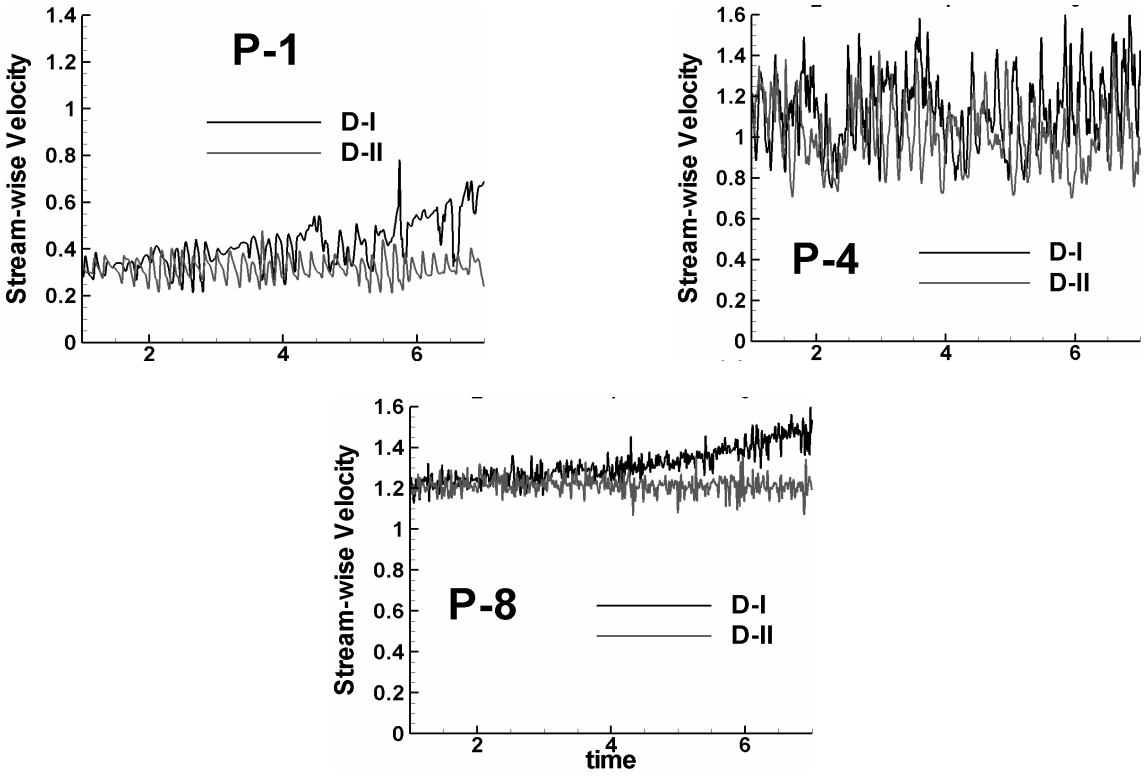

Figure 2.7 - Comparison of time history of stream-wise velocity for selected probes

Power Spectral Density (PSD) comparisons between CVP and TVP inlet conditions are made at points P-2 and P-6 (Figure 2.8). Point P-6, which lies in the outer shear layer between the jet and the mainstream, exhibits substantial difference in its turbulence content. While CVP has lesser turbulent content with energy concentrated in a few frequencies, TVP shows a much broader frequency content which is a result of the turbulence in the coolant jet. In general, it is observed that points which lie in the boundary layer near the surface are not affected greatly by the turbulence content of the

coolant jets as exemplified by P-2, whereas points which lie in the outer shear layer are influenced by the TVP inlet condition. From these observations it can be expected that the turbulence in the coolant jets will have an impact on jet-mainstream mixing in the outer shear layer, but will not directly influence mixing near the surface, which is dominated by the near wall entrainment in the wake of the jet.

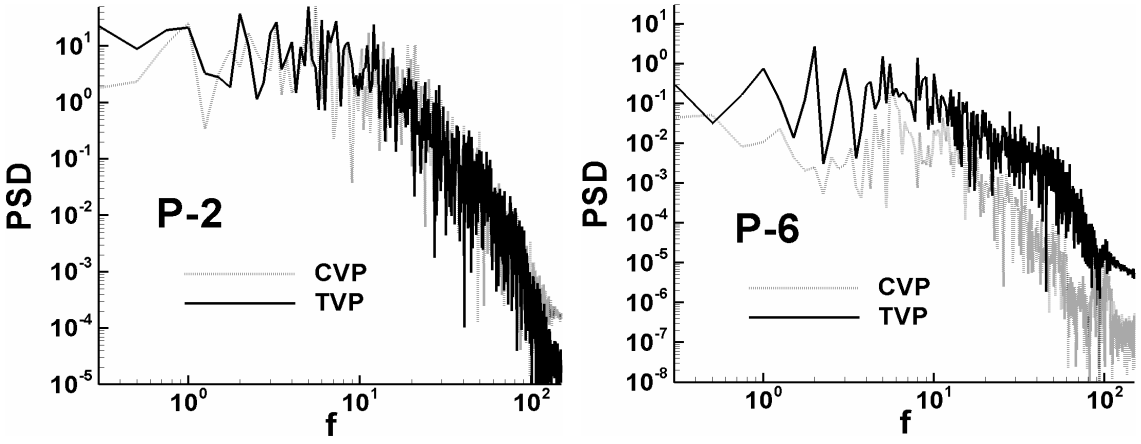

Figure 2.8 - Power Spectral densities of selected locations with CVP and TVP

It is noted that at P-6 with the CVP inlet, spectral peaks are observed between non-dimensional frequencies (based on D and u_∞) of 5 to 6. This characteristic frequency is observed at all the monitoring locations. On application of the TVP condition, in addition to the same characteristic frequency, f, between 5 and 6, which now is not as dominant as with CVP, additional energetic modes are also observed at f = 1, 2, 3 in the outer shear layer. These frequencies are a result of the artificial cycling introduced for TVP at f=1. To explore this aspect further, the PSD of the axial velocity in the coolant jet about 0.5D from its exit is compared to the experiments of den Toonder et al.(1997) (Figure 2.9). The frequency in this case is non-dimensionalized by the coolant flow bulk velocity and pipe diameter to match the experiments. While the experimental location is at y^+~12, the

approximate location in terms of y^+ in the coolant pipe is calculated to be 6. A number of low frequency peaks are observed in the spectrum, which are characteristic of the fundamental cycling frequency introduced at the pipe inlet. However, in spite of the energy being concentrated at select low frequencies, the energy distribution in the coolant jet is quite similar to the energy content in a fully-developed pipe flow. The similarity is more apparent when the experimental results are compared with the smoothed (averaged) numerical data[3].

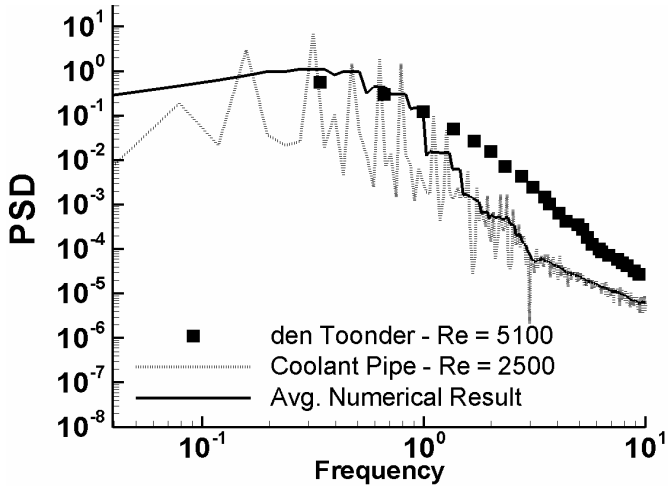

Figure 2.9 - PSD of axial coolant velocity at 0.5D from exit at $y^+ = 6$

2.4.3 Near wall coolant-mainstream mixing mechanism

The mixing mechanism of coolant and mainstream, coherent structures and their role in entrainment of hot gases underneath the coolant are similar for both domains, and for both boundary conditions at the coolant pipe inlet. To describe this process, the following definition is used to describe the location of flow/structures from this point forward: in the lateral direction, the side that the jet blows from is specified with prefix "aft" and the side the jet blows to, specified with prefix "fore". In the stream-wise direction along the

[3] To obtain the averaged data, Savitzky-Golay filter from Matlab is used.

blade surface, “leeward” is used to denote the downstream side of the jet and “windward” the upstream side of the jet. All distances are measured from the hole center. Figure 2.4 shows the notation used.

The dominant coherent structures for a classical jet in cross flow are: counter-rotating vortex pair in the wake of the jet, horseshoe vortex on the windward side of the jet, and shear layer vortices [Tyagi and Acharya (2003), Iourokina and Lele (2005)]. To identify the coherent structures in the present study, the vortex eduction technique proposed by Chong et al. (1990) is used. In this method, in regions dominated by vortical motion the velocity gradient tensor exhibits two eigen values which are complex conjugate. The magnitude of the eigenvalue is indicative of the strength of the vortex. The structures identified by this method are referred to as “coherent vorticity” in this paper, and the magnitude of the eigenvalue as the strength of the vortices. Figure 2.11 shows an instantaneous snapshot of coherent vorticity. An immediate observation is the complete absence of a horseshoe vortex. This is due to the combination of the low injection ratio and the compound angle injection. Pressure contours in planes normal to the surface and at the leeward-side of the hole at s/d=1.0, show a low pressure region at the hole centerline (Figure 2.10). This low pressure region is responsible for creating a strong counter rotating vortex pair which entrains hot mainstream gases underneath the coolant jet.

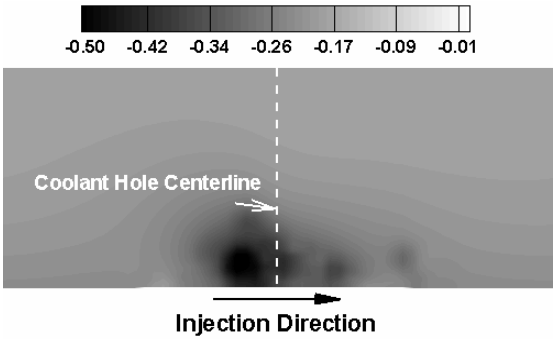

Figure 2.10 - Pressure contour at *s/d* = 1.0 downstream of the coolant hole

The primary structure forms immediately at the leeward edge of the hole (Figure 2.11) and is transported downstream to form packets of hairpin vortices. This agrees with the observations of Tyagi and Acharya (2003) for a jet in cross flow in a flat plate boundary layer. However, as we can see in the pressure contours in Figure 2.10, the strength of these counter rotating vortices is not equal, and the structure at the aft-side of the jet has considerably higher strength and size due to the lateral direction of coolant injection. Compared to a classical jet in cross flow, additional structures in the form of vortex tubes form at the windward side of the coolant hole. They are produced by the interaction of the transverse jet velocity and the mainstream flow. These vortex tubes bend towards the mainstream direction, on top of the hairpin vortices. It is noted that the vortex tubes are not stationary structures but constantly move fore-to-aft along the windward rim of the hole. Vortex tubes on the top of the jet break down quickly and assimilate with the vortex packet within 1- to 2 diameters downstream of the jet, while the structures at the aft- and fore-edge of the hole are stronger and directly participate in the jet-mainstream dynamics. One of these tubes is seen to extend at least 6*d* downstream of the jet, aiding the entrainment of hot gases.

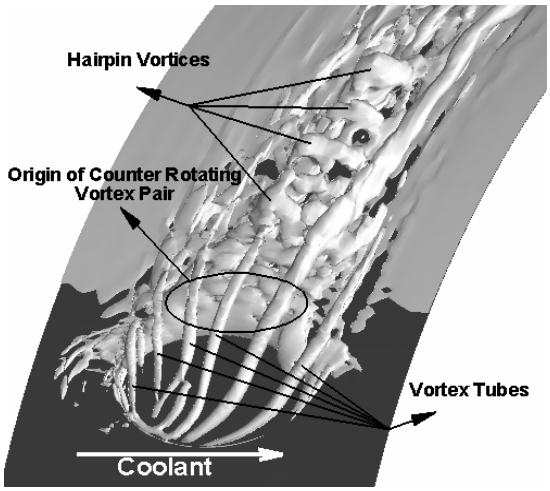

Figure 2.11 - Instantaneous coherent structures

Figure 2.12 explains the jet-mainstream interaction mechanism by means of instantaneous temperature contours and velocity vectors in planes normal to the blade surface and downstream of the jet. At *s/d* = 1.0, one can identify vortex tubes on the top and sides of the counter-rotating vortex pair. The strength of the main counter-rotating vortex aided by the outer vortex tubes near the aft-side causes the bulk of the hot gas entrainment. As the jet travels downstream (*s/d*=2.0), the strength of the primary counter rotating vortex decreases. Eventually at *s/d* = 4.0, the weak component of the counter-rotating vortex pair, at the fore-side of the jet, disappears. As mentioned earlier, vortex tubes travel on the top and sides of the primary vortex structure. The tubes located at the top join with the stronger component of the counter-rotating vortex pair and contribute to entraining hot gas into the coolant from the aft-side. Vortex tubes located at the sides of the primary structure remain intact and separate. At *s/d*=2.0, the vortex tube on the fore-edge of the coolant jet is seen to entrain hot gases. The side vortex tubes periodically cause the coolant flow to break off and join again with the main portion of the coolant jet.

Due to the lateral velocity component of the coolant, it is observed that at *s/d* = 6.0 the jet completely shifts to the fore-side.

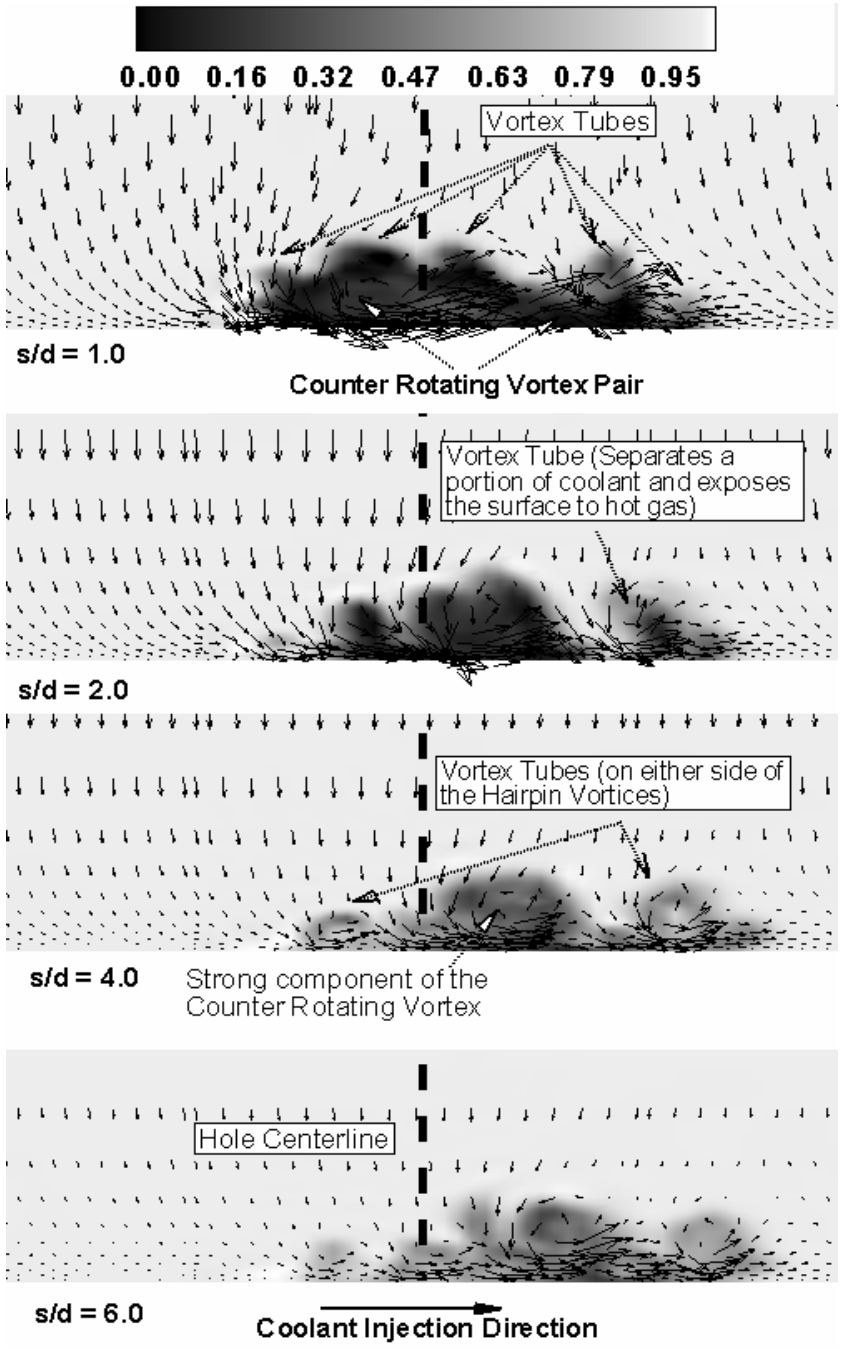

Figure 2.12 - Temperature contour and velocity vectors on cross sectional planes normal to the surface and downstream the hole

2.4.4 Mean profiles

Figure 2.13 shows the mean velocity profiles of flow parallel to the surface of the cylinder at 4 locations downstream of the coolant hole and along its centerline. The profiles are plotted versus the normal distance from the surface normalized by the coolant pipe diameter. The velocity distribution at *s/d*=1.0, in the immediate wake of the jet is characterized by a large velocity defect and the beginnings of a boundary layer which results from lateral flow entrainment into this region. At this location the maximum velocity at 0.325-0.35*d* from the surface is representative of the center of the coolant jet penetration into the mainstream and coincides with the location of minimum temperature (at jet centerline) in Figure 2.14. By *s/d*=2.0, a turbulent boundary layer is established as the mainstream flow accelerates. Interestingly, very minor differences are observed between CVP and TVP, chief among them being the slightly larger penetration of the coolant jet with TVP.

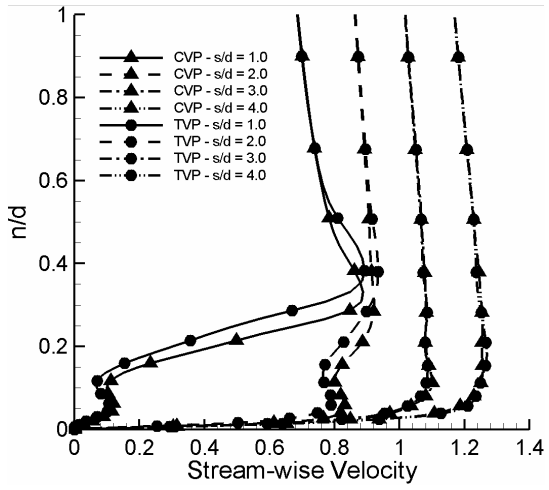

Figure 2.13 - Mean velocity profiles parallel to the surface of the cylinder

Figure 2.14 shows non-dimensional wall adiabatic temperature profiles at the centerline and downstream of the hole for the adiabatic effectiveness calculations. A high

wall temperature in Figure 2.14 implies lower effectiveness. At *s/d*=1.0, for both inlet conditions, CVP and TVP, the wall temperature is approximately 0.45-0.5. This confirms the strong unsteady hot gas entrainment underneath the coolant jet shown in Figure 2.12 at *s/d* = 1.0 and confirmed by the mean velocity profile in Figure 2.13. However, a notable difference between the two is the recovery of the wall temperature at *s/d*=2.0. While for the CVP inlet, the wall temperature decreases, pointing to coolant diffusing into this region between *s/d*=1.0 and *s/d*=2.0, with the TVP condition, the recovery does not occur and the wall temperature increases monotonically with stream-wise distance. Another notable difference between the two coolant pipe inlet conditions is the extent of the thermal mixing layer. A thicker thermal layer is present with TVP indicating more mixing between the coolant and mainstream. The enhanced mixing can also be deduced from the profiles themselves, which are somewhat flatter with TVP. The increased mixing with TVP is consistent with the earlier observation in Figure 2.8 that the outer shear layer between the jet and the mainstream is more turbulent.

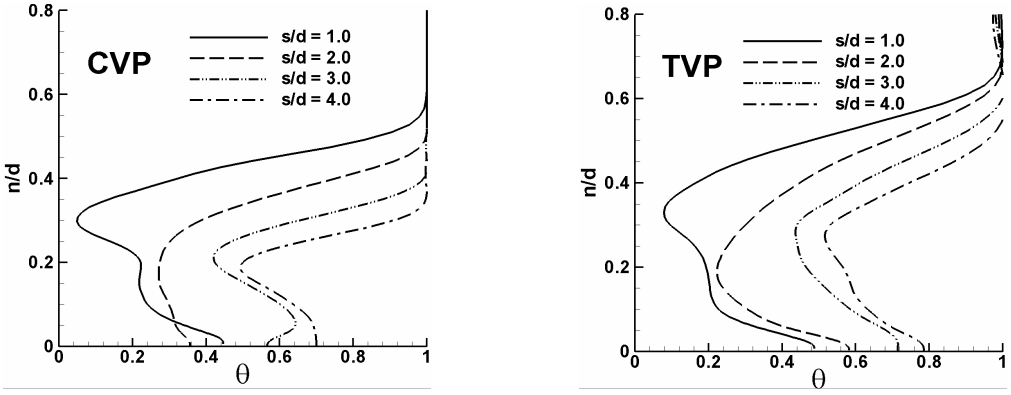

Figure 2.14 - Time averaged temperature profile normal to the wall at jet centerline for CVP and TVP conditions.

2.4.5 Turbulent statistics and kinetic energy

Turbulent kinetic energy behavior along the stream-wise direction is shown in Figure 2.15 and Figure 2.16 shows the *rms* distributions. The distributions are along the hole centerline, normal to the surface and are only shown at four locations, and as such do not give a complete picture but only aid in identifying the major features of the turbulent field. At s/d = 1.0, two peaks appear in the T.K.E distribution, one very close to the surface and another between 0.1-0.2d. The inner maximum close to the wall results from the strong lateral entrainment of fluid into the wake of the jet and is supported by the high values of w_{rms} at the same location. The outer maximum is a result of the interaction between the main body of the coolant jet with the mainstream. While this peak steadily decreases further downstream from the injection location as the coolant jet loses momentum, the inner peak increases up to s/d=2.0 and then settles down to a near constant value, typical of turbulent boundary layers between 0.015-0.02u_∞^2. A noticeable difference between CVP and TVP is observed in the T.K.E profiles in the outer part or in the region of jet-mainstream interaction. At all locations, TVP exhibits higher values of T.K.E. For example, at s/d=2.0 and n/d=0.2, the respective T.K.E. values are 0.018 versus 0.008 for TVP and CVP, respectively. This trend is present at all stream-wise locations and the differences are particularly evident in the outer part of the jet-mainstream interaction zone. These observations are consistent with earlier observations made in Figure 8 and Figure 2.14.

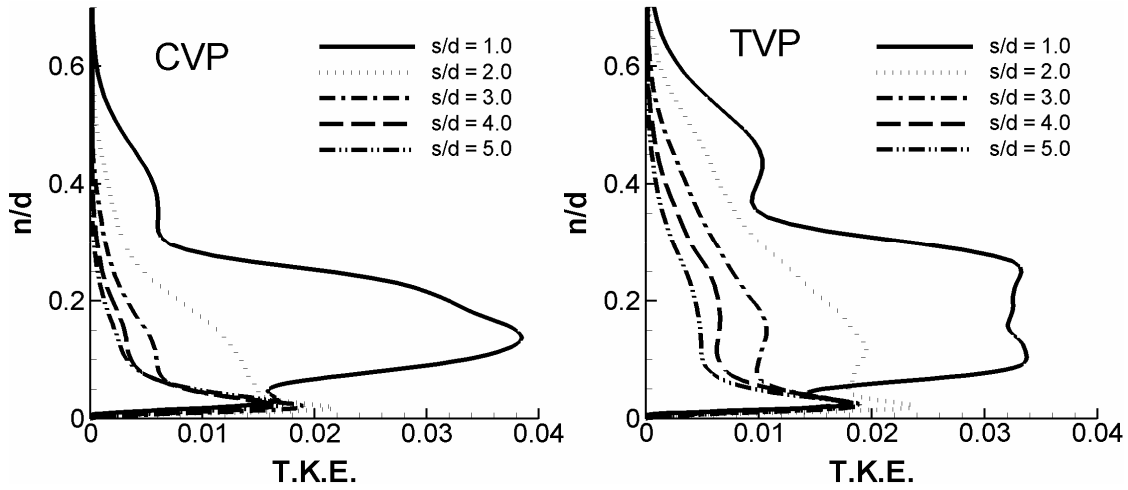

Figure 2.15 - T.K.E profile along stream-wise for CVP and TVP conditions

Turbulent statistics show maximum *rms* values at 0.2*d* from the surface in the region of coolant-mainstream interaction at the centerline (*z/D*=0.0) and *s/d* = 1.0 for u_{rms} and v_{rms}[4]. However, w_{rms} exhibits two peaks, representative of the jet-mainstream interaction and the turbulence generated by the lateral entrainment of hot gases in the near wall region. Further downstream, as in the T.K.E. profiles, the maximum *rms* values shift to the near wall region, where a turbulent boundary layer is developing. In the near wall region at *s/d* = 1.0, the turbulence exhibits strong anisotropy. While u_{rms} and v_{rms} values show somewhat similar values and profiles, w_{rms} shows a very different distribution and higher magnitude, due to the strong lateral entrainment. As the coolant travels downstream the stress components become more isotropic in the outer part. As it was observed in the T.K.E. profile, the *rms* values are higher farther from the wall with TVP condition and downstream of the coolant hole compared to the results with CVP condition.

[4] The directions of u_{rms} and v_{rms} coincide with the flow direction and the direction normal to flow, respectively, and not with the x- and y-axis.

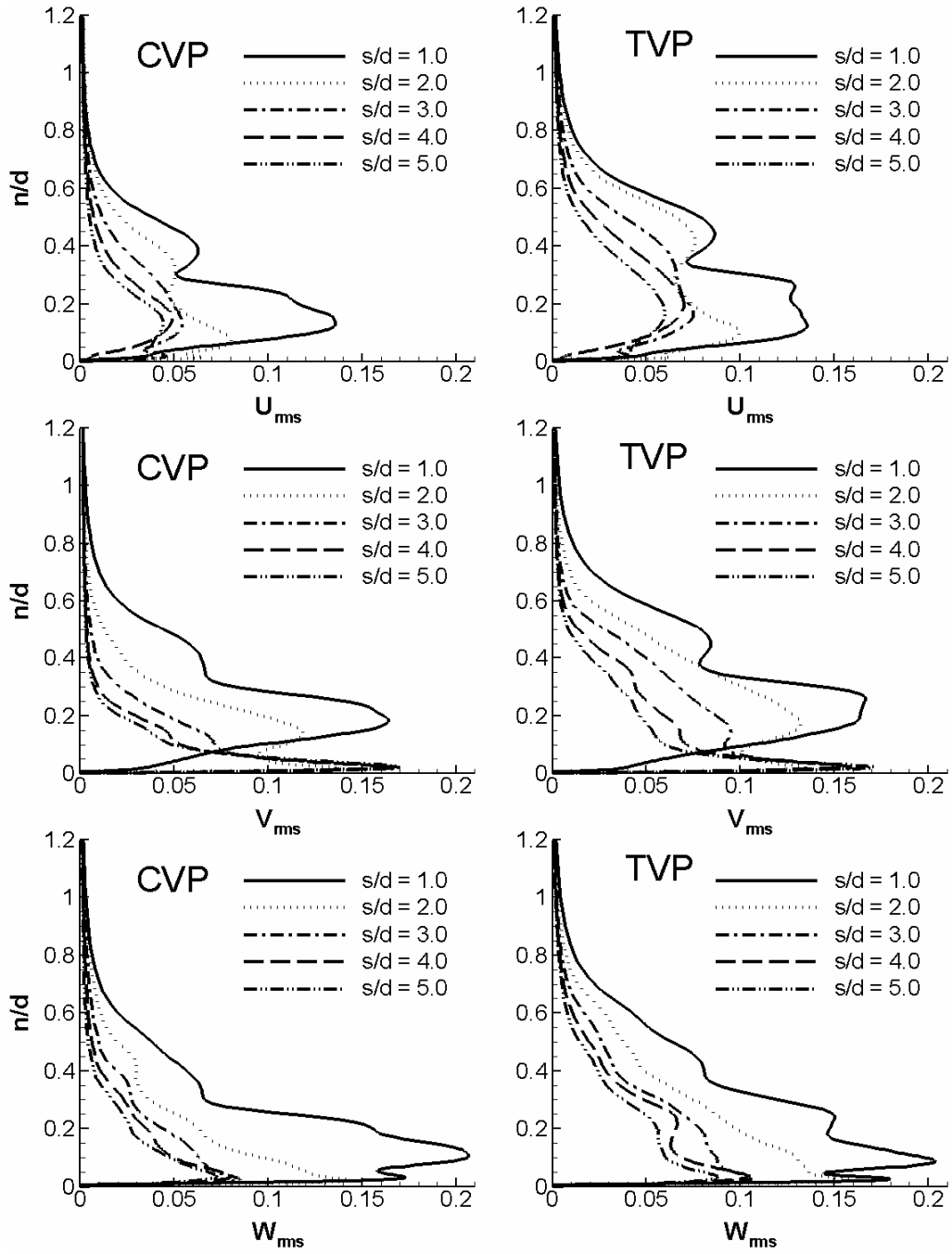

Figure 2.16 - Turbulent statistics' profile along stream-wise direction for CVP and TVP conditions

T.K.E. contours in the span-wise direction also give useful information on the effect of inlet turbulence on the effectiveness in Figure 2.17. The three locations correspond to the aft edge (z/D=-0.015), center (z/D=0.0) and fore side (z/D=0.015) of the coolant

hole. The contours show that the maximum values of T.K.E. occur at the leeward and aft-side of the coolant hole. The jet-mainstream interaction shear layer thickness is thicker and more elongated with the TVP condition. Also, the T.K.E. contained in the aft vortex tube and on the top center of the coolant hole have higher values with TVP condition. The higher T.K.E on the aft-side of the coolant jet results in more entrainment of mainstream fluid which results in lower adiabatic effectiveness distribution and narrower coverage. Conversely, on the fore side, the CVP condition results in higher T.K.E. values in the vortex tube.

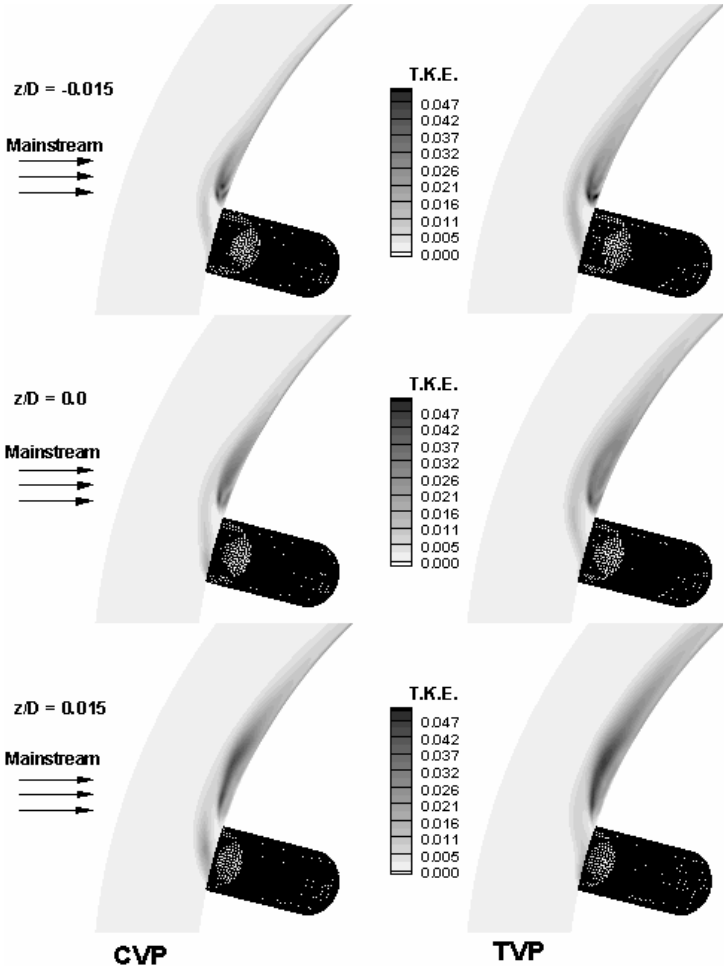

Figure 2.17 - T.K.E. contours in span-wise direction for CVP and TVP conditions

2.4.6 Adiabatic Effectiveness

Adiabatic effectiveness is used to quantify the attachment of the coolant to the blade surface given by:

$$\eta = \frac{T^*_{aw} - T^*_{\infty}}{T^*_c - T^*_{\infty}} \qquad \text{or} \qquad \eta = 1 - \theta_{aw} \tag{2.6}$$

Figure 2.18 compares the distribution of adiabatic effectiveness with TVP and CVP inlet conditions. At the low blowing ratio studied, the adjacent holes in the span-wise direction have no effect on each other and the coolant does not provide good coverage to the full pitch, but is washed down with the strong mainstream flow for both coolant pipe inlet conditions. In the near field immediately downstream of coolant ejection, the TVP condition results in lower effectiveness at the fore-lee side of the jet because of increased mixing with the turbulent jet. Another observed difference is the narrower spread of the jet on the leeside as it diffuses downstream with the TVP condition. A quantitative comparison with Ekkad et al. (1998) is made in Figure 2.19 which plots the span-wise averaged adiabatic effectiveness downstream of coolant injection. As observed earlier, the CVP condition calculates a higher adiabatic effectiveness than TVP, whereas the TVP inlet coolant condition compares very favorably with the experiments. While the experimental jet inlet conditions are not documented, it is our expectation that the coolant issuing from the exit will be turbulent due to the sharp shear layers which usually form at the entrance to the coolant pipe from the plenum.

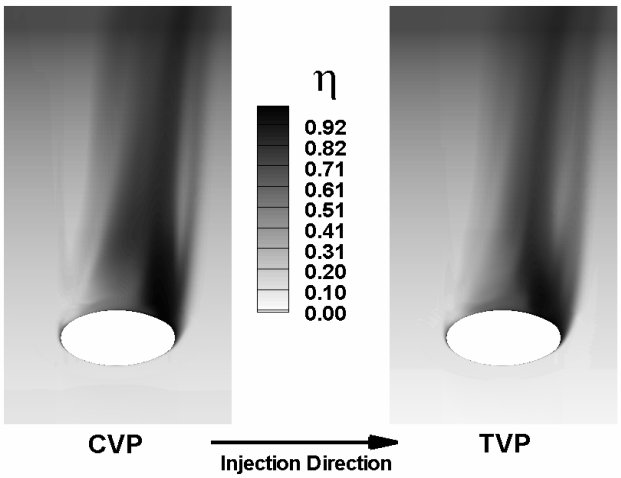

Figure 2.18 - Surface distribution of adiabatic effectiveness for CVP and TVP conditions

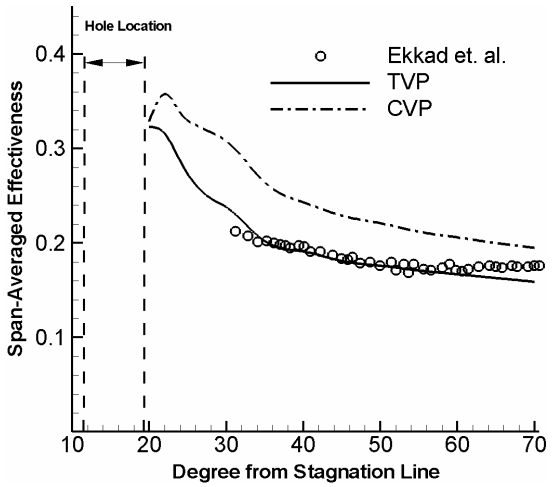

Figure 2.19 - Span-wise averaged adiabatic effectiveness distribution

2.4.7 Heat transfer coefficient

The heat transfer coefficient is expressed in terms of the Frossling number, $Nu/Re^{1/2}$. Based on the non-dimensionalization used, the Nusselt number is calculated as

$$Nu_i = \frac{1}{\theta_w - \theta_{ref}} \tag{2.7}$$

where θ_w is the wall temperature subjected to a non-dimensional heat flux of unity, and θ_{ref} is the reference temperature equal to the mainstream bulk temperature (θ_{ref} = 0.0). Figure 2.20 shows the surface distribution of Frossling number for the two coolant pipe inlet conditions CVP and TVP. Unlike the large differences in adiabatic effectiveness, minor differences exist between the two, which at first seems counter intuitive. However, as noted earlier in the distribution of turbulence, the TVP condition mostly affects turbulence in the outer layer and not so much near the wall. Hence, its effect on lowering adiabatic effectiveness comes from enhanced mixing between the coolant and the mainstream away from the surface which increases the adiabatic wall temperature. On the other hand, the heat transfer coefficient is strongly dependent on turbulence in the near wall region, which does not change substantially between the two cases (see Figure 2.15 and Figure 2.16). The conclusions reached are very similar to the effect of free-stream turbulence, which at low blowing ratios decreases the adiabatic effectiveness but has a small effect on heat transfer coefficients [Ekkad et al. (1998)].

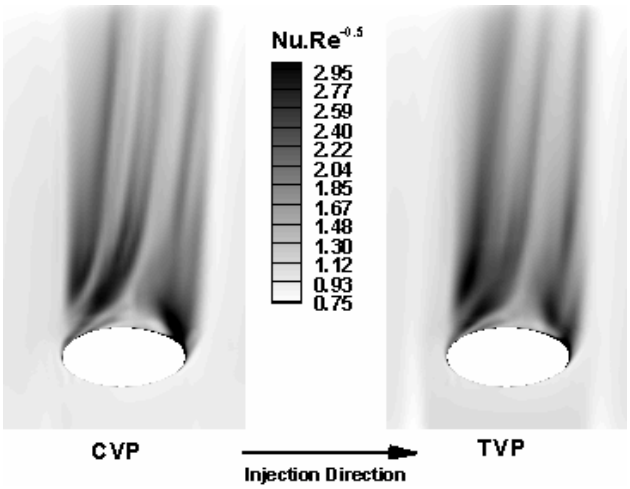

Figure 2.20 - Span-wise averaged adiabatic effectiveness distribution

Three regions of high heat transfer coefficients located at the aft and fore-side of the coolant hole are observed, all of which can be directly related to near wall coherent structures. Figure 2.21 shows the mean structures identified by taking the time mean of the instantaneous coherent vorticity magnitudes. The mean structures identified in the figure manifest the persistent instantaneous coherent vorticity. The region of high heat transfer which begins at the aft edge of the jet and which shifts towards the centerline of the hole in Figure 2.20 results from the entrainment dynamics of the stronger component of the counter-rotating vortex pair, which is represented by the blob of coherent vorticity immediately downstream of injection. The regions of high heat transfer coefficients at the fore and aft edges of the holes are a direct result of the instantaneous vortex tubes which are shown at these locations in Figure 2.11 and Figure 2.12. These structures are temporally persistent and have a strong identity in the mean and their proximity to the wall produces strong temperature gradients. A quantitative comparison is obtained with the spanwise-averaged Frossling numbers in Figure 2.22, which show excellent agreement.

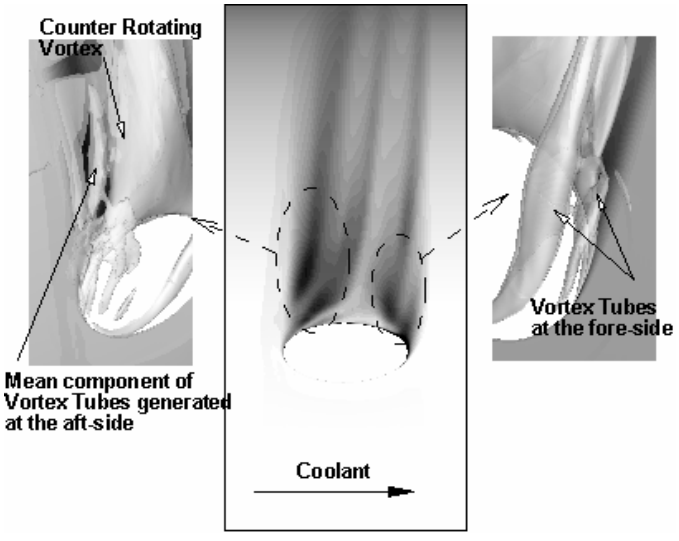

Figure 2.21 - Effect of mean coherent structures on heat transfer coefficient

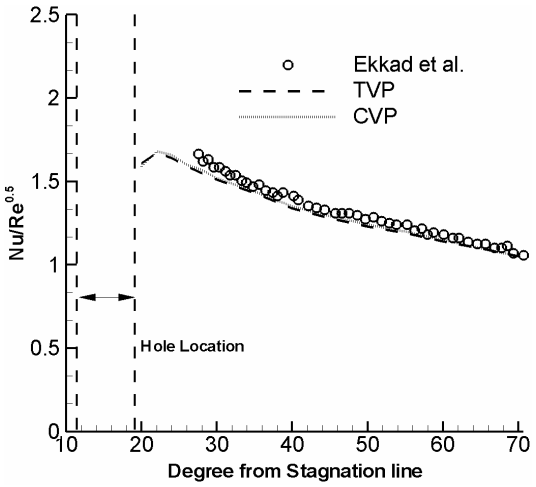

Figure 2.22 - Span-wise averaged Frossling number distribution

2.5. Summary and Conclusions

A representative leading edge film cooling geometry has been modeled with Large Eddy Simulation to analyze the coolant-mainstream flow interaction at a free stream Reynolds number of 100,000 and a blowing ratio of 0.4. Two rows of compound angle injection holes are located $\pm 15^{o}$ from stagnation. The calculation i) investigated the effect of coolant pipe inlet condition on film cooling effectiveness and heat transfer coefficient, ii) identified the important coherent structures and their effect on adiabatic effectiveness and the heat transfer coefficient, iii) described the coolant mixing process with the mainstream and main flow entrainment, and iv) provided turbulent statistics and detailed adiabatic effectiveness and heat transfer coefficient distributions.

The results show the existence of an asymmetric counter-rotating vortex pair in the immediate wake of the coolant jet. The driving mechanism for the formation of these vortices is a low pressure zone in the wake which entrains mainstream flow laterally into this region. The vortex on the fore-side of the jet is much weaker and quickly loses its identity within *s/d*=2.0 downstream of the injection. In addition to these primary

structures, the lateral injection of the coolant and its interaction with the mainstream flow result in the formation of tube vortices on the windward side of the coolant hole which are convected downstream over and to the aft- and fore-side of the counter-rotating vortex pair. While some of the vortex tubes merge with the counter-rotating vortex pair quickly, others located aft and fore of the jet maintain a separate identity and play a dominant role in the entrainment of hot gases and in augmenting the heat transfer coefficient.

Two coolant pipe inlet conditions are studied: a constant velocity profile at the inlet with no turbulence, and a turbulent profile. In the former, in spite of the absence of turbulence in the mainstream and the jet, the jet-mainstream interaction results in the flow becoming turbulent immediately downstream of the jet with the formation of a turbulent boundary layer. A characteristic low frequency interaction between the jet and the mainstream is clearly identified at a non-dimensional frequency (based on D and u_∞) between 5 and 6. On introducing turbulence in the coolant jet, mixing with the mainstream in the outer region of the jet is increased. However, the jet turbulence does not directly impact near wall turbulence which is dominated by three-dimensional entrainment in the wake of the jet. As a result, adiabatic effectiveness decreases due to greater mixing between the jet and the mainstream, whereas the heat transfer coefficient is not affected significantly.

The comparison of span-wise averaged adiabatic effectiveness and Frossling number showed excellent agreement with experimental data. Surface distributions of adiabatic effectiveness show that the coolant does not provide full coverage in the span-wise direction at the low blowing ratio studied. Surface distributions of time-averaged

Frossling number show that regions of high heat transfer coefficients can directly be related to coherent structures in the immediate wake of the jet.

2.6. References

Abdel-Wahab, S. and Tafti, D. K., 2004. Large Eddy Simulations of Flow and Heat Transfer in a 90º Ribbed Duct with Rotation - Effect of Coriolis and Centrifugal Buoyancy Forces. Journal of Turbomachinery 126, 627-636.

Azzi, A., Lakehal, D., 2001. Perspective in modeling film cooling of turbine blades by transcending conventional two-equation turbulence model. Proceedings of IMECE'01, November 11-16, 2001, New York, NY.

Bergeles, G., Gosman, A.D., Launder, B.E., 1978. The turbulent jet in a cross stream at low injection rates: A three-dimensional numerical treatment. Numerical Heat Transfer 1, 217-242.

Chernobrovkin, A., Lakshminarayana, B., 1999. Numerical simulation and aerothermal physics of leading edge film cooling. Proceedings of institution of mechanical engineers, 213-A, 03-118.

Chong, M.S, Perry, A.E., Cantwell, B.J., 1990. A general classification of three dimensional flow fields. Phys. Fluids A 2, No. 5, 765-777.

Cruse, M.W., 1997. A study of film cooling adiabatic effectiveness for turbine blade leading edges. M.S. Thesis, The University of Texas, Austin, Texas.

Cui, J. and Tafti D. K., 2002. Computations of Flow and Heat Transfer in a Three-Dimensional Multilouvered Geometry. Int. J. Heat Mass Transfer 45(25), 5007-5023.

den Toonder, J. M. J., Nieuwstadt, F. T. M., 1997. Reynolds Number Effects in a turbulent Pipe Flow for Low to Moderate Re. Journal of Physics of Fluids 9, No. 11, 3398-3409.

Ekkad, S.V., Han, J.C., Du, H., 1998. Detailed film cooling measurement on a cylindrical leading edge model: effect of free-stream turbulence and coolant density. Journal of Turbomachinery 120, 799-807.

Ekkad., S.V., Ou, S., Rivir, R.B., 2004. A transient infrared thermography method for simultaneous film cooling effectiveness and heat transfer coefficient measurements from a single test. Journal of Turbomachinery 126, 597-603.

Germano, M., Piomelli, U., Moin, P., and Cabot, W.H., 1991. A dynamic subgrid-scale eddy viscosity model. Phys. Fluids 3, 1760-1765.

Guo, X., Schroder, W., Meinke, M., 2006. "Large-eddy simulation of film cooling flows". Computers and Fluids, pp 587-6066

Han, J.G., 2004. Recent studies in turbine blade cooling. International Journal of Rotating Machinery. 10(6), 443-457.

Iourokina, I.V., Lele, S.K., 2005. Towards large eddy simulation of film cooling flows on a model turbine blade leading edge. 43rd AIAA Aerospace Science Meeting and Exhibit, 10-13 January 2005, Reno, Nevada.

Iourokina, I.V., Lele, S.K., 2006. Large eddy simulation of film cooling above the flat surface with a large plenum and short exit holes. 44th Aerospace Science Meeting and Exhibit, Jan 9-12 2006, Reno, NV.

Johnston, C.A., Bogard, D.G., McWaters, M.A., 1999. Highly turbulent mainstream effects on filmcooling of a simulated airfoil leading edge. ASME paper No. 99-GT-261.

Lin, Y.L., Shih, T.I.P., 2001. Film cooling of a cylindrical leading edge with injection through rows of compound angle holes. Journal of Heat Transfer 123, 645-654.

Lui, K., Pletcher, R.H., 2005. Large eddy simulation of discrete-hole film cooling in a flat plate turbulent boundary layer. 38th AIAA Thermophysics Conference, 6-9 June 2005, Toronto, Ontario, Canada, AIAA 2005-4944.

Mehendale, A.B., Han, J.C., 1992. Influence of high mainstream turbulence on leading edge film cooling heat transfer. Journal of Turbomachinery 114, 707-715.

Mick, W.J., Mayle, R.E., 1988. Stagnation film cooling and heat transfer including its effect within the hole pattern. Journal of Turbomachinery 110, 66-72.

Moin, P. Squires, K., Cabot, W., Lee, S., 1991. A Dynamic Sub-Grid-Scale Model for Compressible Turbulence and Scalar Transport. Phys. Fluids A, 3-11, 2746- 2757.

Ou, S., Rivir, R.B., 2001. Leading edge film cooling heat transfer with high free stream turbulence using a transient liquid crystal image method. International Journal of Heat and Fluid Flow 22, 614-523.

Petukhov, B.S., in T.F. Irvine and J.B. Hartnett, Eds., 1970. Advances in Heat Transfer. Vol. 6, Academic Press, New York.

Rozati, A., Tafti, D.K., 2007. Large Eddy Simulation of Leading Edge Film Cooling Part-I: Computational Domain and Effect of Coolant Inlet Condition. ASME Paper

No. GT2007-27689, Proceedings ASME Turbo Expo 2007: Power for Land, Sea and Air, May 14-17, 2007, Montreal, Canada.

Salcudean, M., Gartshore, I., Zhang, K., McLean, I., 1994. An experimental study of filmcooling effectiveness near the leading edge of a turbine blade. Journal of Turbomachinery 116, 71-79.

Sewall, E.A., Tafti, D.K., 2007. Large Eddy Simulation of Flow and Heat Transfer in the Developing Flow Region of a Rotating Gas Turbine Blade Internal Cooling Duct with Coriolis and Buoyancy Forces. Journal of Turbomachinery, *in press.*

Sewall, E.A., Tafti, D.K., 2006. Large Eddy Simulation of Flow and Heat Transfer in the 180º Bend Region of a Stationary Ribed Gas Turbine Blade Internal Cooling Duct. Journal of Turbomachinery 128, pp 763-771

Sewall, E.A., Tafti, D.K., Graham, A.B., Thole, K.A., 2006. Experimental validation of large eddy simulation of flow and heat transfer in a stationary ribbed duct. International Journal of Heat and Fluid Flow 27, 243-258.

Shyy, W., He, X., Thakur, S., 1999. Jets and free stream interaction around a low-Reynolds number airfoil leading edge. Numerical Heat Transfer, Part A, 35, 891-902.

Tafti, D.K., Cui, J., 2003. Fin-tube junction effect on flow and heat transfer in flat tube multilouvered heat exchangers. International Journal of Heat and Mass Transfer 46, 2027-2038.

Tafti, D.K., 2001. GenIDLEST – A Scalable Parallel Computational Tool for Simulating Complex Turbulent Flows. Proc. ASME Fluids Engineering Division, FED – vol. 256, ASME-IMECE, New York, 2001.

Thakur S., Wright, J., Shyy, W., 1999. Convective film cooling over a representative turbine blade leading edge. International Journal of Mass Transfer 42, 2269-2285.

Theodoridis, G.S., Lakehal, D., Rodi, W., 2001. Three-dimensional calculations of the flow field around the turbine blade with film cooling injection near the leading edge. Flow, Turbulence and Combustion 66, 57-83.

Thompson, J.F., Warsi, Z.U.A., Mastin, C.W. Numerical Grid Generation, Foundation and Applications. Elsevier Science Publishing Co., Inc., New York, New York 10017, 1985

Tyagi, M., Acharya, S., 2003. Large eddy simulation of film cooling flow from an inclined cylindrical jet. Journal of Turbomachinery 125, 734-742.

York, D.W., Leylek, J.H., 2002a. Leading edge film cooling physics: Part I – Adiabatic effectiveness. Proceedings of ASME Turbo Expo 2002, June 3-6, 2002, Amsterdam, The Netherlands, ASME paper No. GT-2002-30166.

York, D.W., Leylek, J.H., 2002b. Leading edge film cooling physics: Part I – Adiabatic effectiveness. Proceedings of ASME Turbo Expo 2002, June 3-6, 2002, Amsterdam, The Netherlands, ASME paper No. GT-2002-30167.

Yuki, U.M., Bogard, D.G., Cutbirth, J.M., 1998. Effect of coolant injection on heat transfer for a simulated turbine airfoil leading edge. ASME paper No. 98-GT-431.

Chapter 3 : Effect of Coolant-Mainstream Blowing Ratio on Leading Edge Film Cooling Flow and Heat Transfer[5]

Abstract

Large Eddy Simulation (LES) is used to analyze and quantify the effects of the coolant-to-mainstream blowing ratio in leading edge film cooling. A cylindrical leading edge with a flat after-body represents the blade leading edge, where coolant is injected with a 30˚ compound angle. Three blowing ratios of 0.4, 0.8, and 1.2 are studied. Free-stream Reynolds number is 100,000 and coolant-to-mainstream density ratio is unity. At B.R.= 0.4, three types of coherent structures are identified which consist of a primary entrainment vortex at the leeward aft-side of the coolant hole, vortex tubes at the windward side of the coolant hole, and hairpin vortices typical of turbulent boundary layers produced by the turbulent interaction of the coolant and mainstream downstream of injection. At B.R.=0.8 and 1.2, coherent vortex tubes are no longer discernable, whereas the primary vortex structure gains in strength. In all cases, the bulk of the mixing occurs by entrainment which takes place at the leeward aft-side of the coolant jet. This region is characterized by a low pressure core and the primary entrainment vortex. At B.R.=0.4, the fore and aft vortex tubes also contribute to entrainment. Turbulent shear interaction between the jet and the mainstream, which increases substantially with blowing ratio, also contributes to the dilution of the coolant jet as evidenced by the large increase in turbulent kinetic energy in the region of interaction. As a result of the increased mixing between coolant jet and mainstream, adiabatic effectiveness decreases

[5] This chapter is accepted for publication as an article in International Journal of Heat and Fluid Flow, "Effect of Coolant-Mainstream Blowing Ratio on Leading Edge Film Cooling Flow and Heat Transfer", *under review*, Rozati, A., Tafti, D.K., Copyright Elsevier, 2007

with an increase in blowing ratio. On the other hand, the increased turbulent intensities in the primary entrainment vortex result in an increase in the heat transfer coefficient.

Key words: Leading edge film cooling, Large Eddy Simulation, blowing ratio, adiabatic effectiveness, heat transfer coefficient

Nomenclature

B.R.	Blowing Ratio (u_c/u_∞)
C_s	Smagorinsky constant
D	Leading edge diameter
d	Coolant hole diameter
k	Thermal conductivity
l	Coolant hole length to diameter ratio
n	Normal to the wile
Nu	Nusselt number ($Nu = hD/k$)
Pr	Prandtl number ($Pr = \nu/\alpha$)
P	Coolant hole span-wise pitch
q''	Heat flux
Re	Reynolds number ($Re = u_\infty D/\nu$)
S	Strain rate tensor
s	Parallel to the wall
T	Temperature
u	Cartesian velocity vector/streamwise velocity
x	Physical coordinates
θ	Nondimensional temperature ($\theta = (T-T_c)/(T_\infty-T_c)$)
ζ	Computational coordinates
υ	Kinematic viscosity

Subscripts

aw	adiabatic wall
b	bulk

c coolant

t turbulent parameters

τ values based on friction velocity

∞ free stream

Superscripts

* dimensional parameter

3.1. Introduction

3.1.1 Previous Experimental Studies

Optimization of turbine blade film cooling requires the investigation of various flow and geometrical conditions and parameters. Amongst them, coolant-to-mainstream Blowing Ratio (B.R.) has a significant effect on the aero-thermal efficiency as well as durability of the turbine both by affecting the film cooling effectiveness, and controlling the bleed air from the compressor section. Previous experimental studies on flat plate film cooling by Sinha et al. (1991), Honami et al. (1992), Schmidt and Bogard (1996), Kelly and Bogard (2003), Saumweber et al. (2003), and Mayhew et al. (2004) show that flow pattern, temperature field and film cooling performance vary with the angle of injection, number of rows, coolant-to-mainstream blowing and density ratios, and free stream turbulence intensity level. General conclusions on the effect of B.R. from these investigations are: a) increase in B.R. decreases film cooling effectiveness especially in low free stream turbulence, however, it can be beneficial in high free stream turbulence; b) increase in B.R. increases the heat transfer coefficient.

Flat plate film cooling studies, although being extremely useful in understanding the phenomenon due to the simple geometry, are unable to accurately represent regions with combined curvature and mainstream acceleration such as the leading edge of a blade, where the highest heat transfer rates over the entire airfoil occur [Han et al. (2000)]. In most experimental studies, this region is modeled by a cylindrical leading edge with a flat after-body, where the coolant is injected into the main flow with a compound angle. Studies of Mehendale and Han (1992), Salcudean et al. (1994), Funazaki et al. (1997), Cruse et al. (1997), Yuki et al. (1998), Ekkad et al. (1998, 2004), Jahnston et al. (1999), Ou and Rivir (2001), and Mouzon et al. (2005) have investigated this type of representative leading edge under different B.R., mainstream turbulence and other parameters such as coolant-to-mainstream density ratio and wake effects. Overall conclusions on the effect of B.R. in these studies are similar to that of the flat plate: film cooling effectiveness decreases with increase in B.R. at low free stream turbulence; however this effect is minimal (or in some cases positive) at high free stream turbulence. Heat transfer coefficient always increases with B.R., although this augmentation is minimal at high free stream turbulence.

3.1.2 Previous Numerical Studies

While the experimental studies have provided valuable information on influential factors in film cooling, developments in CFD provide a strong tool to obtain a more comprehensive perception of this complex flow field. Lakehall et al. (1998) simulated the experimental study of Honami et al. (1992) with standard k-ε and a k-ε based two-layer model which resolved the near wall viscous region with a one equation model. While these models were able to capture many of the flow features, the former under-predicted

coolant lateral spreading and strength of the counter-rotating vortex, and the latter under-predicted jet vertical spread. Adami et al. (2002) studied flat plate film cooling with different shaped holes and a two equation k-ω model of Wilcox (1993) without wall function. They identified the secondary flow structures for the fan shape holes. Their result of lateral averaged adiabatic effectiveness was in good agreement with experimental data. Roy et al. (2003) used Detached Eddy Simulation (DES) to simulate the experimental model of Sinha et al. (1991). However, DES did not improve the accuracy of predicted effectiveness downstream of the coolant hole and RANS model provided a better answer, yet still under-predicted experimental data. Tyagi and Acharya (2003) used Large Eddy Simulation (LES) on a flat plate and results of velocity, temperature, and effectiveness profiles were in good agreement with experiments of Sinha et al (1991) and Lavrich and Chiapetta (1990). In addition to the previously reported counter-rotating vortex pair and roller vortices, they reported the formation of hairpin coherent structures downstream of the coolant hole. Muldoon and Acharya (2004) used Direct Numerical Simulation (DNS) to compare the terms of k and ε with the ones of a k-ε model on flat plate film cooling. As a result, a damping function for eddy viscosity was proposed. Liu and Pletcher (2005), Iourokina and Lele (2005, 2006), and Guo et al. (2006) also applied LES to flat plate film cooling.

The experimental set up of Cruse et al. (1997) has been simulated by Chernobrovkin and Lakshminarayana (1999), Shyy et al. (1999), Lin and Shih (2001), and York and Leylek (2002 a,b). Azzi and Lakehal (2001) and Theodoridis et al. (2001) also predicted the film cooling effectiveness and flow field in the leading edge. These studies used a variety of RANS models including two-layer k-ε model, k-ω shear stress transport model,

and standard k-ε models with near wall treatment with/without incorporated anisotropy treatments. The motive of these somewhat *ad hoc* modifications is the inadequacy of the standard RANS models in predicting anisotropic turbulence. Results were in acceptable agreement with measured data, although the typical under-prediction of coolant lateral spread still existed. Additionally, accuracy of some results was very sensitive to parameters such as the inlet turbulent length scale. Of the described numerical studies on film cooling, whether on flat plate or leading edge, only York and Leylek (2002) reported the predicted values of heat transfer coefficient. The discrepancies of the results increased with increase of the blowing ratio.

3.1.3 Previous LES Studies on the Leading Edge

In spite of assumptions of isotropy, eddy-viscosity RANS models have been reasonably successful in predicting film cooling flows in simple geometries to some extent. However, in addition to the shortcomings in flat plate geometries, they cannot consistently and accurately capture all the secondary effects of streamline curvature, strong accelerations and decelerations of the free-stream, and transition. The inadequacies are magnified at high blowing ratios and in predicting heat transfer coefficients. With the prohibitive cost of Direct Numerical Simulations (DNS) studies in complex geometries, LES is the optimal candidate, which not only minimizes the adverse effects of the empiricism in eddy viscosity models by limiting it to small, universal and much less energetic scales, but also captures the transient behavior of flow structures and heat transfer that RANS does not.

Previous studies by the authors [Rozati and Tafti (2006, 2007a,b,c)] were the first to analyze the flow field and heat transfer in the leading edge film cooling with compound

angle of injection using LES. In these studies, a cylindrical leading edge with a flat after body represented the blade with cooling holes located at ±15˚ from the stagnation line. Mainstream Reynolds number was 100,000 and coolant-to mainstream blowing ratios of 0.4 and 0.8 were studied. At B.R.= 0.4, the effect of coolant pipe inlet condition was investigated in detail by imposing two different profiles at the pipe inlet: constant velocity profile, and fully developed time-dependent turbulent profile from an auxiliary pipe flow calculation. Results showed that the coolant turbulence at B.R.= 0.4 only affected the shear interaction between coolant and mainstream interaction and not the very near wall region, which is affected more by the turbulence generated during lateral entrainment. As a result, the effectiveness reduced considerably due to more mixing in the outer jet-mainstream shear layer. However, the heat transfer coefficient, which is governed by the near wall turbulence, remained unaffected. Results were in good agreement with the experimental data of Ekkad et al. (1998).

3.2. Objective of the Study

The present study investigates in detail, the effect of blowing ratio in leading edge film cooling. In particular, differences in flow field and heat transfer are identified and quantified at three blowing ratios of 0.4, 0.8, and 1.2. Coolant-mainstream interaction, dynamics of coherent structures, mean turbulent and averaged values of the flow field, adiabatic effectiveness, and heat transfer coefficient are calculated and analyzed.

3.3. Domain and Boundary Specifications

3.3.1 Computational Domain

The computational domain is adopted from an experimental study of Ekkad et al. (1998). A cylinder with a tailboard represents the blade leading edge. Two rows of cooling holes are located at ±15˚ from the stagnation line with 30˚ compound angle. To avoid separation in the wake of the cylinder, the tailboard is replaced with a flat after body in the computational domain (Figure 3.1). The domain height and length in the experimental setup are $10D^* \times 10D^*$. In the computational domain, a symmetry boundary condition is applied along the stagnation line which reduces the height of the domain to $5D^*$ [Rozati and Tafti, (2007c)]. The diameter of the coolant pipe, $d^* = 0.063D^*$. In the current study, the coolant pipe is modified by increasing its length and embedding ribs close to the inlet to create a turbulent flow in the pipe. These modifications and their effects are explained in detail in section 3.5.1. The pitch between the two adjacent hole in each row is $P^* = 4d^* = 0.252D^*$.

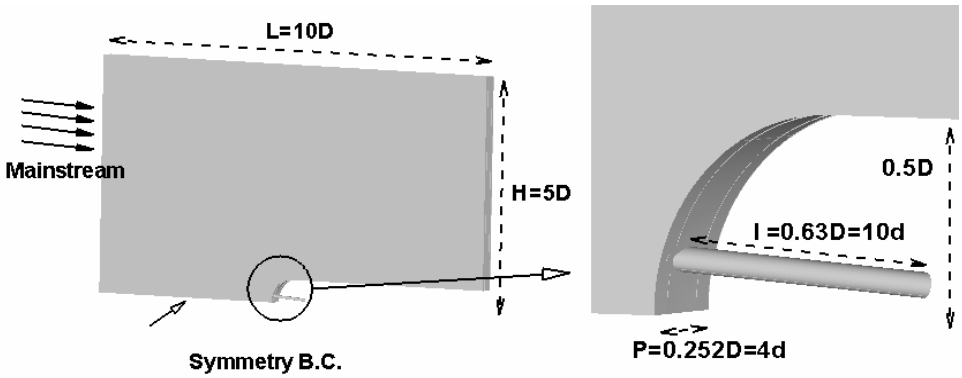

Figure 3.1 - Computational domain

3.3.2 Boundary Conditions

The free stream Reynolds number is 100,000 based on the cylinder diameter. As shown in Figure 3.1, a symmetry boundary condition is applied along the stagnation line. In previous work by the same authors [Rozati and Tafti, (2007c)] it was established that the application of this boundary condition does not affect the coolant-mainstream dynamics at each individual row of the cooling holes and the predicted results are effectively similar to that without the symmetry condition. This verification was made by comparing results of flow development downstream of the cooling hole, non-dimensional coolant-mainstream interaction frequency, and adiabatic effectiveness for both domains with and without the symmetry condition.

At the coolant pipe inlet, a constant velocity profile is applied, which is perturbed by multiple rows of ribs to simulate a turbulent pipe flow (see section 3.5.1). This constant velocity has non-dimensional values of 0.4, 0.8, and 1.2 when normalized by the free stream velocity. At the outlet section, which is approximately 80 jet diameters downstream of injection, a convective outflow condition is specified. A periodic boundary condition is applied in the lateral direction which simulates a row of holes. In calculating the adiabatic effectiveness, no-slip adiabatic wall condition is assumed and mainstream and coolant non-dimensional temperatures are set to unity and zero, respectively. To calculate the Nusselt number, a constant non-dimensional heat flux of unity is specified at the wall and both coolant and mainstream non-dimensional temperatures are zero.

3.3.3 Grid Properties

The multi-block grid contains 72 hybrid structured/unstructured blocks, where the structured blocks have an unstructured inter-block topology to benefit both from the flexibility of an unstructured mesh, and the advantages of a structured grid. Extensive care is dedicated to grid resolution in the stagnation region, coolant pipe near wall region, vicinity of the coolant pipe exit, and downstream of the coolant hole [Rozati and Tafti, (2007c)]. The grid has a total size of 3,866,624 cells where the finest resolution is of $O(1\times10^{-5}D^{*})$ and located at the vicinity of the coolant hole and normal to the blade surface. At B.R.=0.4, there are 45 grid points in the boundary layer region of coolant-mainstream interaction downstream of the coolant hole. Consequently, since the thickness of this layer increases with B.R., the number of grid points which lie within it becomes larger at higher blowing ratios of 0.8 and 1.2. *A-posteriori* results of non-dimensional wall distance ($y^{+}=yu_{\tau}/\nu$) at the first grid point from the wall are shown in Figure 3.2 for all investigated cases. It is noticeable that the regions of high/low y^{+} vary with the dynamics of the coolant-mainstream interaction at each B.R. However, this number clearly does not exceed the value of 0.7, which satisfies the condition of $y_1^{+}<1$ for an accurate LES study.

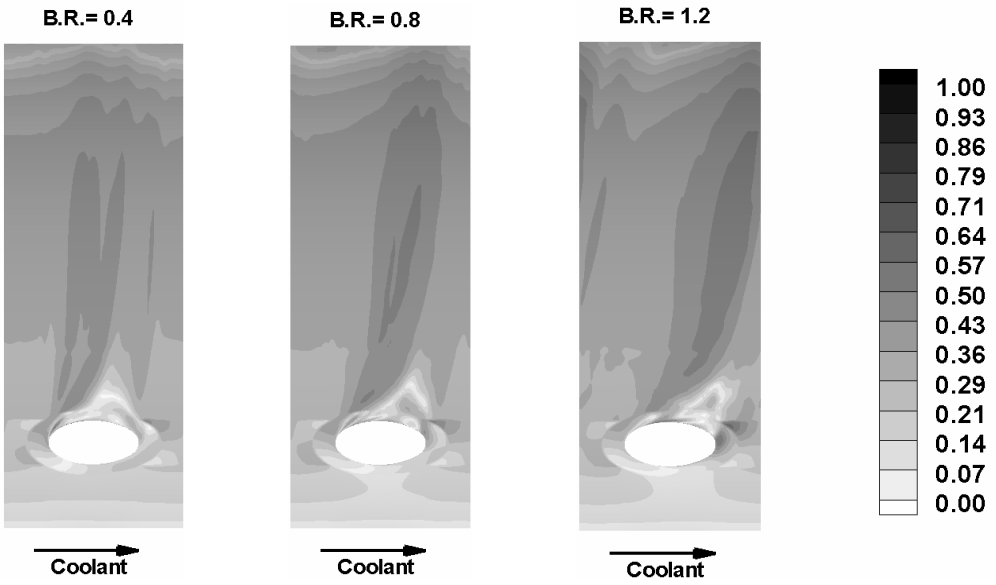

Figure 3.2 - Non-dimensional wall distance at the first grid point from the wall (y_1^+)

3.4. Solution Methodology

3.4.1 Governing Equations

The transformed non-dimensional governing incompressible Navier-Stokes and energy equations are derived based on the nomenclature of Thompson et al. (1985) as follows:

Continuity:

$$\frac{\partial}{\partial \xi_j}\left(\sqrt{g}\overline{U}^j\right)=0 \tag{3.1}$$

Momentum:

$$\frac{\partial}{\partial t}\left(\sqrt{g}\overline{u}_i\right)+\frac{\partial}{\partial \xi_j}\left(\sqrt{g}\overline{U}^j\overline{u}_i\right)=-\frac{\partial}{\partial \xi_j}\left(\sqrt{g}(\bar{a}^j)_i\overline{p}\right)+\frac{\partial}{\partial \xi_j}\left(\left(\frac{1}{\mathrm{Re}}+\frac{1}{\mathrm{Re}_t}\right)\sqrt{g}g^{jk}\frac{\partial \overline{u}_i}{\partial \xi_k}\right) \tag{3.2}$$

Energy:

$$\frac{\partial}{\partial t}\left(\sqrt{g}\bar{\theta}\right)+\frac{\partial}{\partial \xi_j}\left(\sqrt{g}\bar{U}^j\bar{\theta}\right)=\frac{\partial}{\partial \xi_j}\left(\left(\frac{1}{\mathrm{Pr}\,\mathrm{Re}}+\frac{1}{\mathrm{Pr}_t\,\mathrm{Re}_t}\right)\sqrt{g}\,g^{jk}\,\frac{\partial\bar{\theta}}{\partial \xi_k}\right) \tag{3.3}$$

Where U is the contravariant velocity vector, $\vec{a}^i$ are the contravariant basis vectors[6], $\sqrt{g}$ is the Jacobian of the transformation, g^{ij} is the contravariant metric tensor, $\sqrt{g}U^j=\sqrt{g}(\vec{a}^j)_i u_i$ is the contravariant flux vector, u_i is the Cartesian velocity vector, and θ is the non-dimensional temperature.

The over-bar symbol denotes grid filtered quantities. Re_t is the inverse of the non-dimensional turbulent eddy-viscosity and is obtained by the Smagorinsky model

$$\frac{1}{\mathrm{Re}_t}=C_s^{\,2}(\sqrt{g})^{2/3}\left|\bar{S}\right| \tag{3.4}$$

where $\left|\bar{S}\right|$ is the magnitude of the strain rate tensor given by $\left|\bar{S}\right|=\sqrt{2\bar{S}_{ik}\bar{S}_{ik}}$ .The Smagorinsky constant $C_s^{\,2}$ is obtained via the dynamic procedure [Germano et al. (1991)]. The turbulent Prandtl number is assumed to have a constant value of 0.5 [Moin et al. (1991)]. The governing equations of momentum and energy are discretized with a conservative finite volume formulation using a second-order central difference scheme. The temporal advancement is performed with a two-step, semi-implicit predictor-corrector algorithm. Detailed information can be found in Tafti (2001).

In non-dimensionalizing the governing equations, the cylinder diameter (D^*) and free stream velocity (u_∞^*) are used as the length and velocity scales, respectively. Two characteristic temperatures are used to non-dimensionalized the energy equation:

[6] The notation $\left(\vec{a}^j\right)_i$ is used to denote the *i-th* component of vector $\vec{a}^j$, $(\vec{a}^j)_i=\partial\xi_j/\partial x_i$

$\left(T_\infty^* - T_c^*\right)$ when calculating the adiabatic effectiveness, and $q_w''^* D^* / k^*$ when calculating the heat transfer coefficient.

3.4.2 Adiabatic Effectiveness and Nusselt Number

By definition, adiabatic effectiveness is a measure to quantify the coverage of the coolant over the blade surface. In this concept, the effectiveness is 100% if the adiabatic surface temperature is the same as the coolant temperature, and is zero if the adiabatic temperature is equal to the mainstream flow. When calculating the adiabatic effectiveness, the non-dimensional temperature is defined as $\theta = \left(T^* - T_c^*\right) / \left(T_\infty^* - T_c^*\right)$. Therefore, adiabatic effectiveness can be expressed as:

$$\eta = \frac{T_{ad,w}^* - T_\infty^*}{T_c^* - T_\infty^*} = 1 - \theta_{ad,w} \tag{3.5}$$

In calculating the Nusselt number, temperature (θ) is non-dimensionalized by $q_w''^* D^* / k^*$, where $q_w''^*$ is the constant heat flux at the wall. With these definitions, the local Nusselt number is obtained with

$$Nu_D = \frac{1}{\theta_w - \theta_{ref}} \tag{3.6}$$

where based on the free stream temperature, $\theta_{ref} = 0.0$.

3.5. Results and Discussion

The calculations are carried out on Virginia Tech's Advanced Research Computing (ACR) facility, System X, on seventy two, 2.3 GHz PowerPC 970FX processors. The non-dimensional time step is set to 3×10^{-5} for B.R. = 0.4, 2×10^{-5} for B.R. = 0.8, and

1×10^{-5} for B.R. = 1.2. Each time step takes approximately 4.5s of wall clock time. The flow is allowed to develop for approximately 3 time units before averaging process for time-mean quantities is activated for an additional 4 time units. The results explain the different features of the flow physics at each B.R. in detail, and quantify the differences in coolant-mainstream interaction, effectiveness, and heat transfer coefficient at three blowing ratios of 0.4, 0.8, and 1.2.

3.5.1 Coolant Pipe Flow

In a previous study [Rozati and Tafti, (2007c)], it was established that adiabatic effectiveness is highly sensitive to the coolant inlet flow condition. In spite of the absence of any experimental data pertaining to the state of flow in the coolant pipe, it was concluded from simulation results that the coolant flow was turbulent at B.R.=0.4. To replicate the corresponding turbulent flow conditions in the computational coolant pipe, fully developed turbulent inlet frames from an auxiliary pipe flow calculation were fed into the inlet of the pipe, at $3.1d^*$ upstream of the coolant pipe exit (which matched with the length of the pipe in the experiment of Ekkad et al., (1998)). The good agreement of experimental and numerical results of adiabatic effectiveness and heat transfer coefficient were indicative of the fact that the inlet frames provided a close replica of the flow condition in the experimental setup. The storage and complexity limited the number of the inlet frames to a total of one non-dimensional time unit (50,000 frames), which introduced an artificial non-dimensional forcing frequency of unity into the coolant turbulent spectrum. However, it was established that the presence of this frequency did not have any pronounced effect on the jet-mainstream interaction outside of the coolant pipe.

In the current study, an alternative method is utilized in which the turbulence is generated in the primary film cooling calculation by placing turbulators in the form of concentric ribs near the inlet of the coolant pipe. In order for the turbulence to resemble that of a fully-developed pipe flow, the length of the coolant pipe is increased to $10d^*$ to give sufficient time for the rib turbulence to recover into turbulence resembling fully developed flow. Three concentric ribs are placed in the pipe; the first rib is placed at $0.5d^*$ from the inlet and other two are located downstream at a pitch of $1.0d^*$. The width and height of the ribs are $0.115d^*$ and $0.147d^*$, respectively.

Figure 3.3 shows the comparison of the coolant pipe axial velocity power spectral density (PSD) for the coolant pipe with ribs (where turbulence is generated inside the coolant pipe) and the coolant pipe from the previous study where turbulent inlet frames were fed at the inlet. The location of the recorded signal is close to the coolant pipe exit into the mainstream at $y^+ \approx 12$, and B.R.=0.8. Three signals corresponding to the case with turbulent inlet frames (raw and smoothed) and the pipe with ribs are shown. The raw PSD is included to show the contamination of the spectrum at the cycling frequency of the frames and its superharmonics, whereas the smoothed signal is more representative of the spectral intensity. Comparison of the power spectra shows that the cycling frequency of the frames and its super harmonics are eliminated when the turbulence is allowed to develop by introducing the ribs, and at the same time also matches the spectral intensity of that signal.

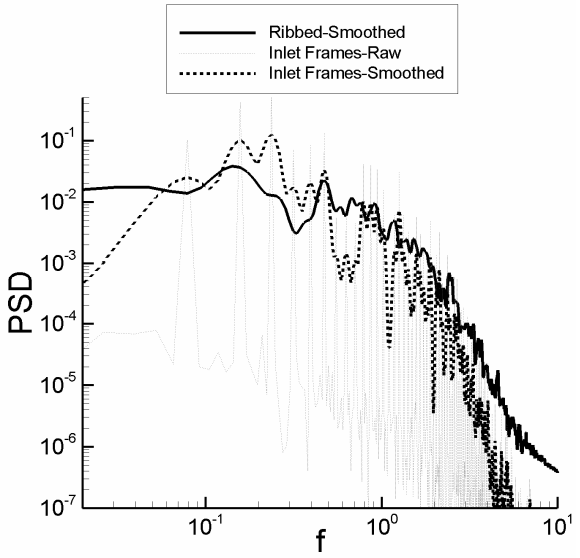

Figure 3.3 - Power spectra of coolant pipe axial velocity

Figure 3.4 shows the profile of numerically calculated u_{rms} and measured u_{rms} from an experimental study of a fully turbulent pipe flow [den Toonder et al., (1997)]. Numerical results are circumferentially averaged and are calculated at $1.5d^*$ from the coolant pipe exit into the mainstream. Distance from the wall (n) and values of u_{rms} are non-dimensionalized by coolant diameter and pipe bulk velocity, respectively. The dotted line illustrates the profile when turbulent frames were introduced at the coolant pipe inlet. Although the peak of the experimental fully developed pipe flow exhibits higher values, the results show the same order of magnitude, and same trend and behavior of a fully-developed turbulent pipe flow, where the peak of the u_{rms} moves towards the wall with an increase in the Reynolds number.

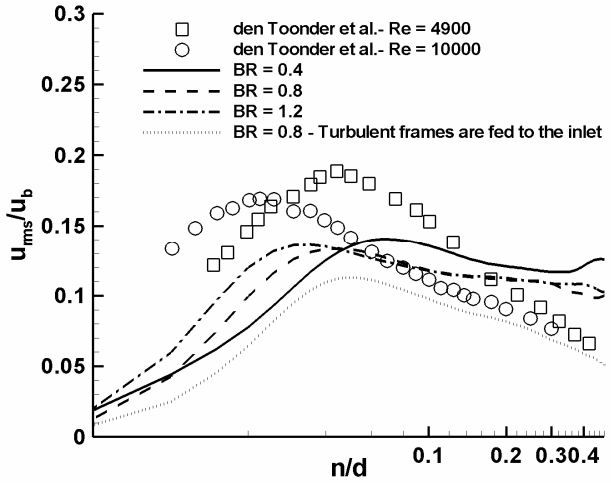

Figure 3.4 - Comparison of coolant pipe u_{rms} at $1.5d^*$ upstream of pipe exit with fully turbulent pipe flow

Since there is no evidence on the flow condition in the coolant pipe to imply whether or not a "fully developed" condition of the flow exists, except that the flow is turbulent and not laminar, in the present calculations the rib dimensions and length of coolant pipe are selected in a way that gives a close replica of a turbulent pipe flow. Figure 3.5 shows the comparison of calculated spanwise-averaged adiabatic effectiveness by using three coolant inlet conditions at B.R.=0.4. The adiabatic effectiveness is grossly over predicted when the coolant pipe has no turbulence, whereas the predictions are more in agreement with experiments when turbulent inlet frames are used or when ribs are used. Between the two, the agreement with experiments is better when inlet frames are used, but the differences for the most part are within 10%. A similar comparison at B.R. = 0.8 shows much better agreement between the two turbulent cases.

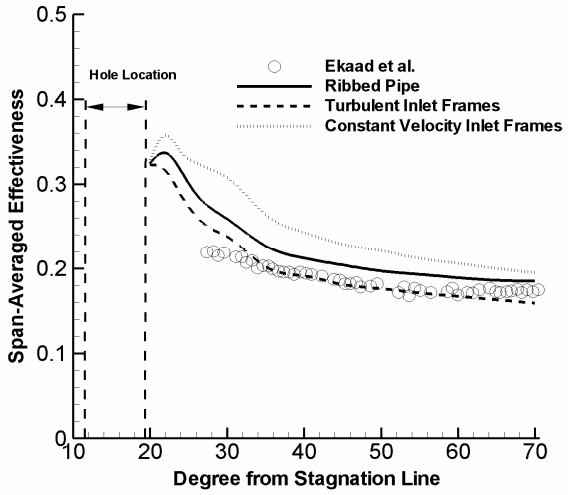

Figure 3.5 - Comparison of adiabatic effectiveness at B.R.=0.4 with experimental data for different coolant pipes

3.5.2 Coherent Structures

To identify the coherent structures in the present study, the vortex eduction technique proposed by Chong et al. (1990) is used. In this method, in regions dominated by vortical motion the velocity gradient tensor exhibits two eigenvalues which are complex conjugate. The magnitude of the eigenvalue indicates the strength of the vortex. The structures identified by this method are referred to as "coherent vorticity" and the magnitude of the eigenvalue as indicative of the "strength of the vortices". The following definition is used to describe the location of flow/structures: in the lateral direction, the side that the jet blows from is specified with prefix "aft" and the side the jet blows to, specified with prefix "fore". In the stream-wise direction along the blade surface, "leeward" is used to denote the downstream side of the coolant hole and "windward" the upstream side of it.

At low blowing ratio of 0.4, the instantaneous snapshot of coherent structures illustrates the formation of a primary vortex at the leeward, and vortex tubes at the

windward edge of the coolant hole (Figure 3.6a). These vortex tubes are instabilities that originate from the shear interaction of the lateral momentum of the coolant with the streamwise motion of the mainstream. Further downstream of the hole, they break into smaller eddies, and get assimilated into packets of hairpin vortices along with the primary vortex and transport downstream. With an increase in the blowing ratio, turbulence levels at the windward edge of the coolant hole rises, resulting in loss of coherency by which the vortex tubes form on a much smaller scale and have no preferential direction (Figure 3.6b,c). While at B.R.=0.4 the tubes at the fore-side (and to some degree aft-side) extend 2-3d^* downstream of the coolant hole and have a pronounced individual effect on flow dynamics, at higher B.R. the tubes degenerate into small scale turbulence. Another difference between coherent structures in BR=0.4, 0.8 and 1.2 is the increase in the strength of vortices. This is illustrated by the value of the vorticity iso-surface at each blowing ratio. Eddies form farther from the wall at B.R.=1.2 and have the smallest scales amongst the three cases, especially at the windward side of the coolant hole. It is also illustrated that the stronger lateral momentum of the coolant jet results in a larger lateral spread (Figure 3.6c).

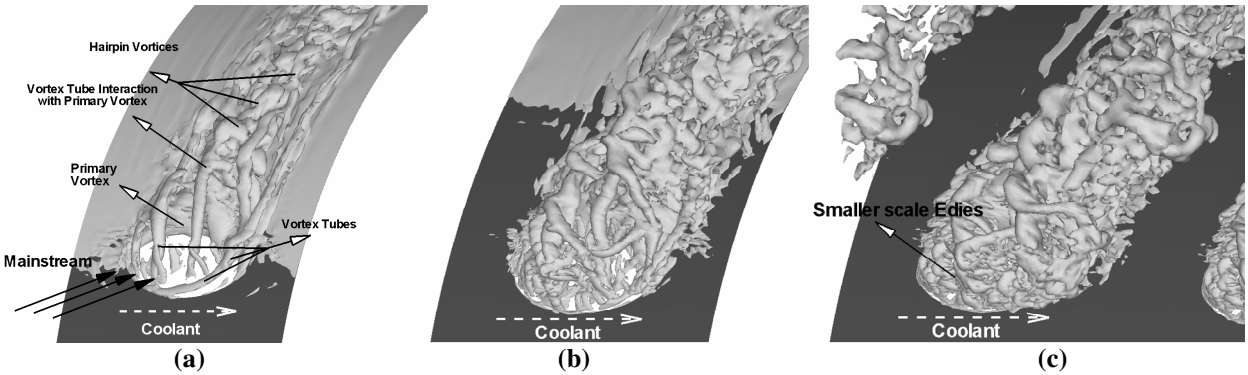

(a) **(b)** **(c)**

Figure 3.6 - Instantaneous coherent structures at (a) B.R. = 0.4 (iso-surface value = 10); (b)B.R. = 0.8 (iso-surface value = 20); (c)B.R. = 1.2 (iso-surface value = 30)

3.5.3 Dynamics of Entrainment

In any jet in cross flow situation, a low pressure region is created at the leeward of the jet which draws mainstream flow into this region, which leads to a decrease in the adiabatic effectiveness. Figure 3.7 shows the time averaged pressure distribution at $1.0d^*$ downstream of the coolant hole. *n/d* indicates the distance from the wall and *z/d* = 0.0 denotes the coolant hole centerline. It is evident that at the leeward edge of the coolant hole, a low pressure region forms in all three cases. In a classical jet in cross-flow (no compound injection), the low pressure region results in the formation of a symmetric counter-rotating vortex pair which entrains the flow from both aft- and fore-side of the coolant jet. In the presence of a compound angle, the low pressure region results in a primary vortex which draws the flow from the aft-side. At B.R.=0.4, a very weak additional counter-rotating vortex is discernible in the near field of injection adjacent to the primary entrainment vortex, which quickly dissipates. The primary vortex is the key element in hot mainstream gas entrainment underneath the coolant. The low pressure region increases in size as well as magnitude with an increase in the B.R. and moves further to the fore-side due to the stronger lateral momentum. Interestingly, the minimum non-dimensional pressure at the core of this region ($\left(p^* - p_\infty^*\right)/\rho^* u_\infty^{*2}$), has values close to the respective blowing ratios. Mainstream entrainment is also expected to become stronger as the pressure decreases with B.R.

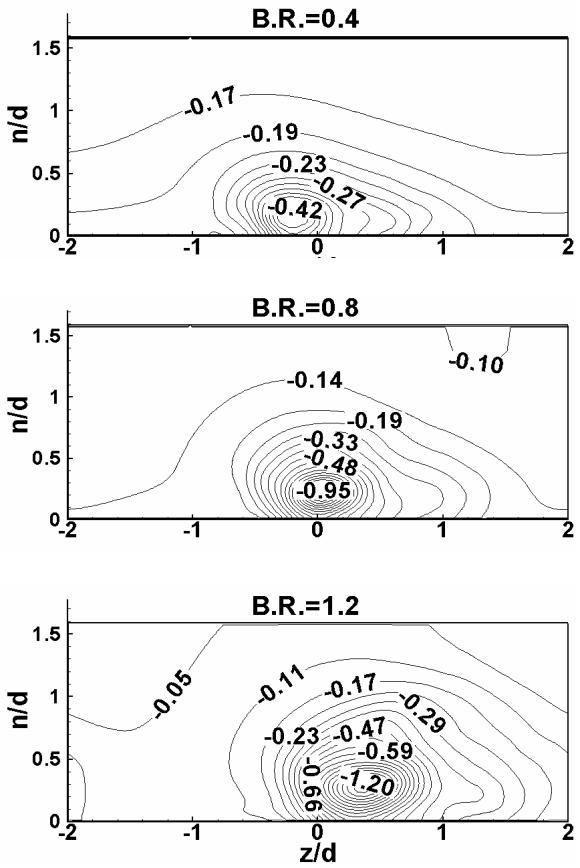

Figure 3.7 - Low (time-averaged) pressure region at s/d=1.0 downstream of the coolant hole

The dynamics of hot mainstream gas entrainment underneath the coolant is described with the aid of instantaneous snapshots of temperature distribution downstream of the coolant hole. Figure 3.8 shows two locations at *s/d*=1.0 and 3.0 for each B.R. The planes are normal to the surface and velocity vectors are projected onto the plane and represent the resultant normal and span-wise velocity components. The size of the velocity vector is indicative of its magnitude. At B.R.=0.4, the role of individual vortex tubes can be identified in the outer shear region and at the fore-side of the coolant hole. With increase of B.R., the individuality of these structures disappears. The effect of stronger lateral momentum at B.R.=1.2 results in the strong deviation of the coolant jet from the jet centerline at B.R.=1.2 when compared to B.R.=0.4. It is evident that entrainment which

mainly occurs from the aft-side of the coolant jet by the primary structure strengthens with increase in B.R. Mixing is also promoted by turbulent diffusion in the inner and outer shear layers between coolant and mainstream, which also increases with blowing ratio. Therefore, at *s/d*=3.0 the coolant still provides good coverage at B.R.=0.4, while at B.R.=1.2 it is not only detached from the surface but also considerably diluted by the combined effect of entrainment and turbulent diffusion.

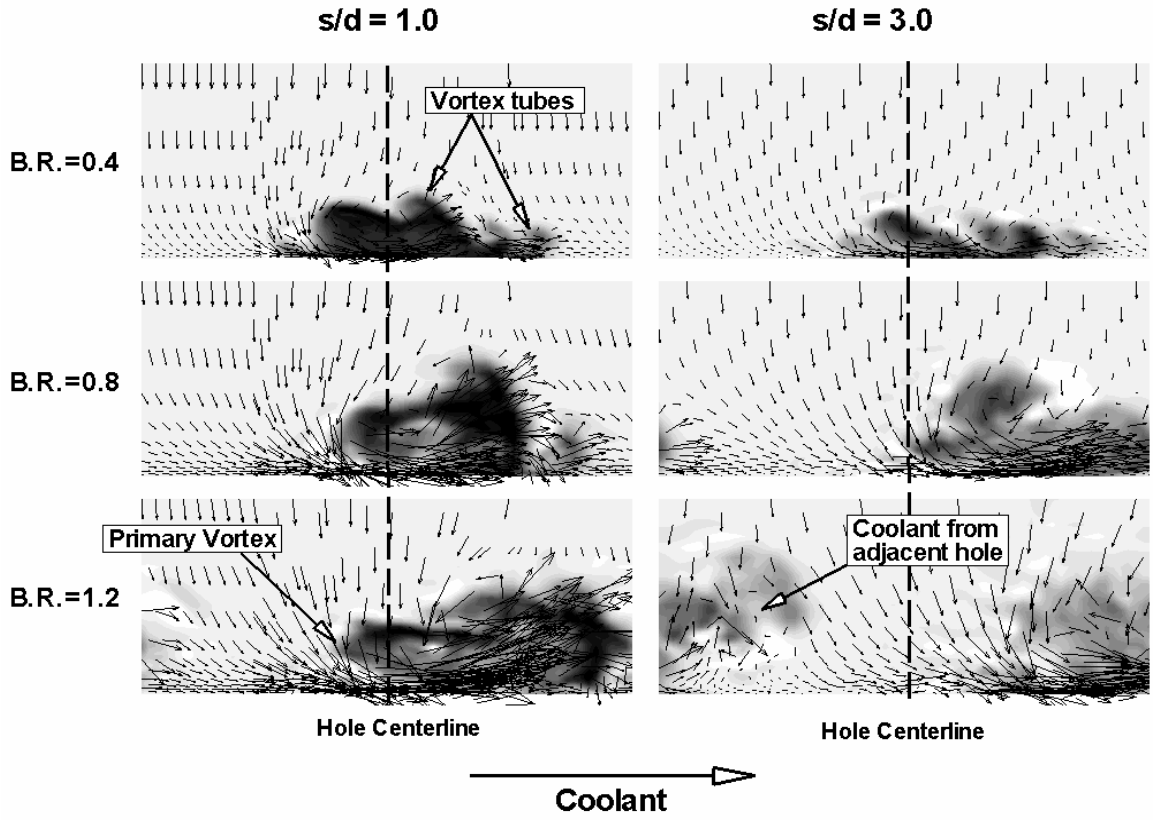

Figure 3.8 - Dynamics of Entrainment

To show the three-dimensional nature of entrainment, time averaged streamlines are imposed on the temperature iso-surface with value of 0.7 (to represent the coolant) at B.R.=1.2 (Figure 3.9). As illustrated, the primary vortex structure draws the mainstream flow underneath the coolant. At B.R.=1.2, the low pressure region is strong enough to

create a slight reversed flow, where the mainstream is drawn towards the fore-side and leeward edge of the coolant hole. It will be illustrated in the next section that the reverse flow effect is diminished at B.R.=0.4 due to the weakening of the low pressure region.

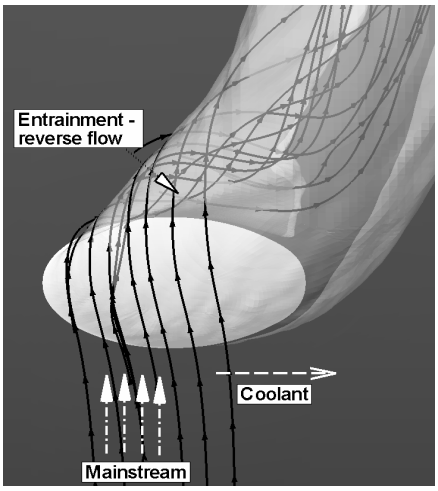

Figure 3.9 - Time averaged streamlines at B.R.=1.2

3.5.4 Mean profiles

The time averaged values of temperature and velocity contours at *s/d*=1.0 downstream of the coolant hole are presented in Figure 3.10. *n/d* indicates the normal distance from the surface and *z/d*=0.0 denotes the coolant hole centerline. Mainstream flow direction is into the page and coolant injection direction is aligned with *z/d* direction. *U*, *V*, and *W* are streamwise, normal, and lateral velocities, respectively. Time averaged temperature contours indicate that with increase of the B.R., the lateral momentum of the coolant pushes it further to the fore-side, and the vertical momentum pushes it further away from the wall. Lower blowing ratios provide a better coverage at the surface, as shown for the instantaneous results in Figure 3.8. It is evident that as B.R. increases, two regions of accelerated flow and reverse flow develop in the stream-wise direction. At B.R.=1.2, the effect of the low pressure region and reversed flow extends to

s/d = 3.0 downstream of the coolant hole. The high positive and negative values of the cross-stream velocity on the aft side result from the primary entrainment vortex. Coincident with this region are high lateral W-velocities. The high values of W at the fore side are due to the lateral momentum of the coolant jet, which increases with B.R.

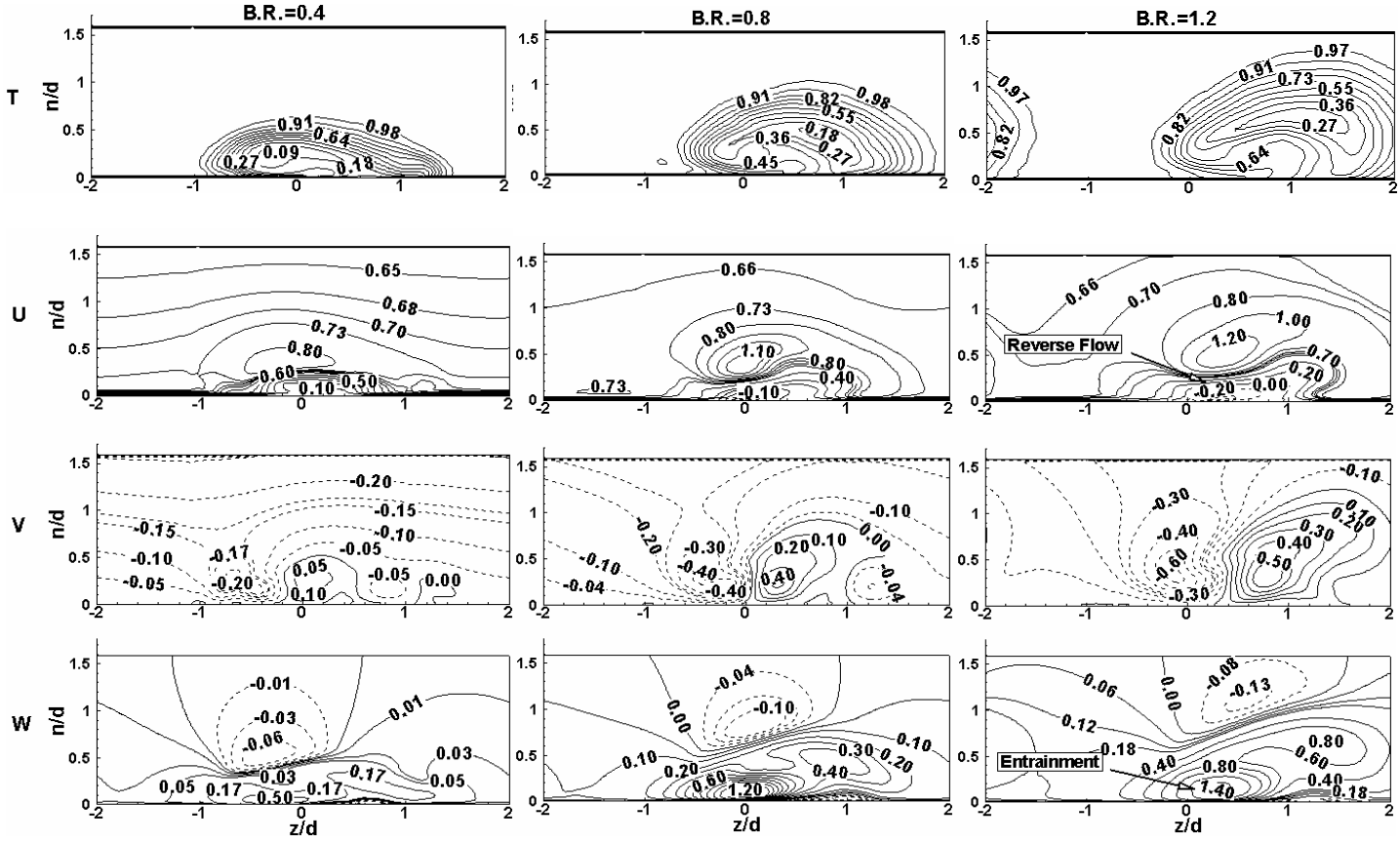

Figure 3.10 - Time averaged velocity and temperature contours s/d = 1.0 downstream the coolant hole

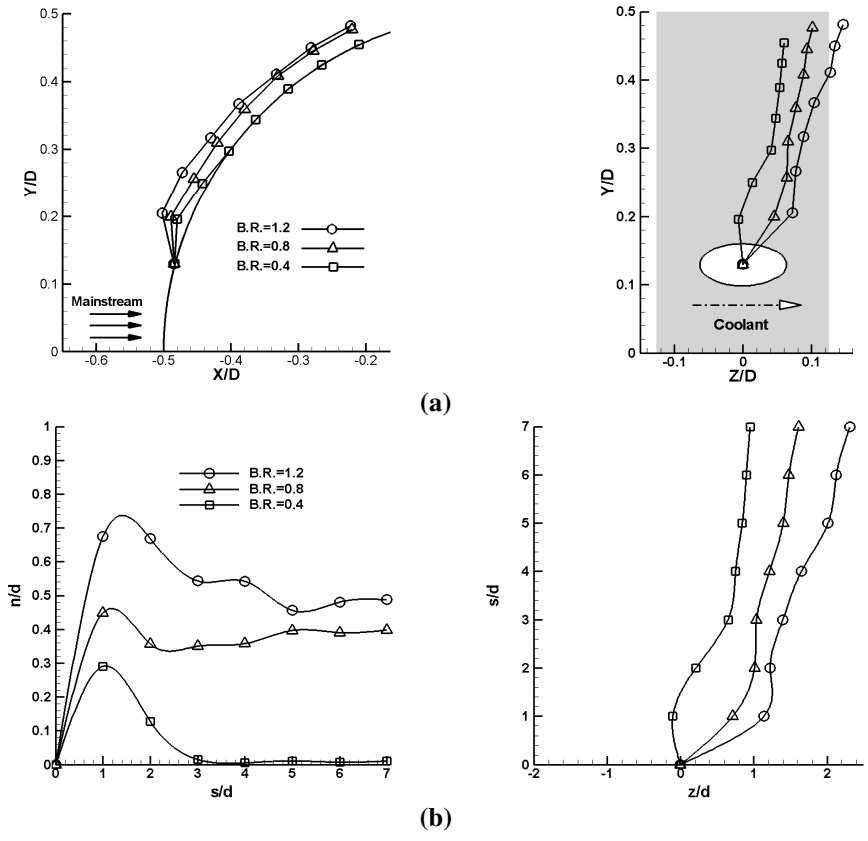

Figure 3.11 - Trajectory of the coolant jet; (a) *xyz* coordinate, (b) *snz* coordinate

The behavior of the coolant flow at different blowing ratios can be analyzed by the trajectory of the core of the coolant. Henceforth in the paper, the core of the coolant jet is defined as the location of the minimum time averaged temperature downstream of the coolant hole. For example, at B.R.=0.4 and *s/d*=1.0, this location is at *n/d*=0.3 and *z/d*=-0.1 (Figure 3.10). Figure 3.11 shows the trajectory of the core for each blowing ratio. The symbols in Figure 3.11a show the location of the core between *s/d*=0.0-7.0. The projection of the coolant path on *x-y* plane (Figure 3.11a) clearly shows that the coolant is lifted off the surface at the leeward edge of the hole and is immediately pushed down to the surface by the mainstream momentum at B.R.=0.4. However, at B.R.=0.8 and 1.2 the coolant core stays away from the wall even at *s/d*=7.0. Although the distance from the

wall is about the same for these two blowing ratios at this location, the coolant core temperature is higher at B.R.=1.2 (θ= 0.66) compared to B.R.=0.8 (θ= 0.62). This indicates more mixing at B.R.=1.2. The projection of the coolant path on the surface (Figure 3.11b) clearly shows that the coolant deviates more from the hole centerline at higher blowing ratios. Figure 3.11b quantifies the deviation of the coolant from the surface and from the centerline based on hole diameter.

To obtain a better understanding of the thermal behavior of the coolant core, variations of the time averaged temperature profile with distance from the surface (*n/d*) downstream of the coolant hole is shown in Figure 3.12. The profile passes through the coolant core at three planes of *s/d*=0.0, 1.0, and 3.0 for all blowing ratio. At the exit, (*s/d*=0.0) the coolant temperature (at *n/d*=0.0) is affected by the mainstream temperature at B.R.=0.4, in contrast to the other two cases. The profile at *s/d*=0.0 also shows that the coolant jet penetrates more into the mainstream at B.R.=1.2. Local peaks close to the wall at *s/d*=1.0 are indicative of the mainstream entrainment, which moves the coolant core (with the minimum values of temperature) away from the surface. It is noticeable how the temperature of the core increases with blowing ratio, not only due to the entrainment, but also by the more intensified mixing in the shear layer between the coolant and the mainstream. Between *s/d*=2.0 and 3.0, entrainment is weakened considerably for B.R.=0.4 and some coolant diffuses to the wall, whereas, mixing and entrainment still dominant the evolution of the temperature profile at the larger blowing ratios.

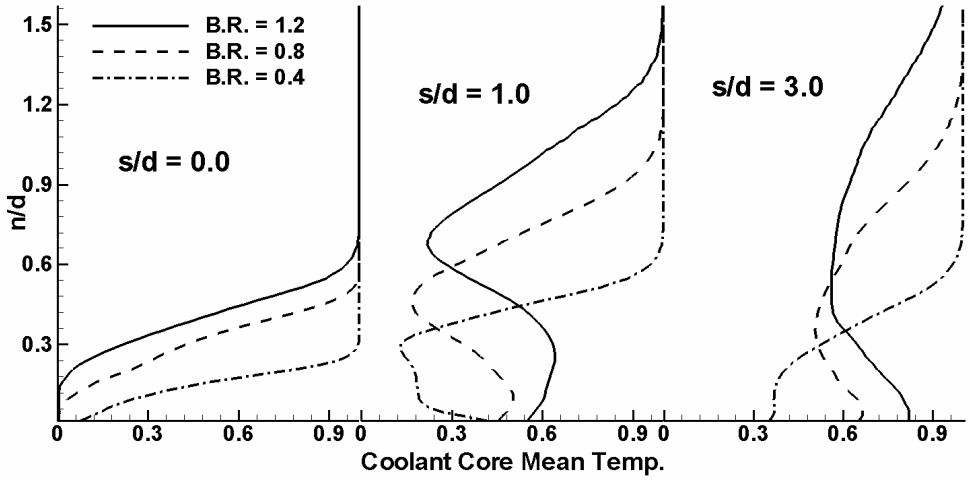

Figure 3.12 - Coolant core time averaged temperature downstream of the hole

To obtain an overall estimate of the thermal field, the span-wise and time averaged temperature is shown in Figure 3.13 at the same three planes as in Figure 3.12. Based on the definition of adiabatic effectiveness (equation 3.5), the lower values of temperature at the surface (*n/d* = 0.0) downstream of the coolant hole is indicative of better coverage and higher effectiveness. At *s/d*=0.0 the surface temperature is lowest at B.R.=1.2. This is because mainstream penetration into the coolant jet exit is minimal at the high blowing ratio. The local minimums at *s/d* = 1.0 and 3.0 are indicative of the hot mainstream entrainment, which is highest at B.R. = 1.2 as observed in Figure 3.12. An interesting observation is the almost linear variation of the thermal boundary layer with the blowing ratio. It seems that the thermal boundary layer becomes twice and three times greater at B.R. = 0.8 and 1.2 when compared to its thickness at B.R. = 0.4.

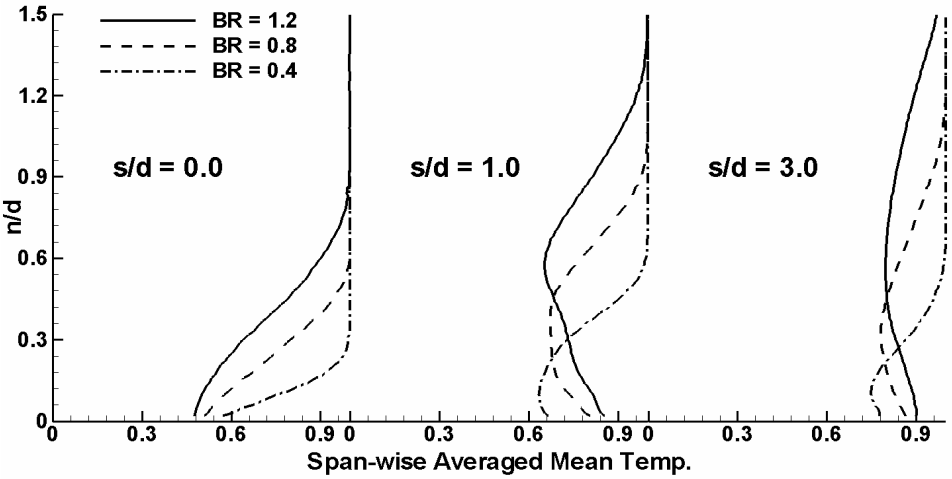

Figure 3.13 - Span-wise averaged profile of the mean temperature downstream the coolant hole

3.5.5 Turbulent statistics and kinetic energy

Figure 3.14 shows the spanwise distribution of turbulent kinetic energy (T.K.E.) at *s/d*=1. First it is noted that the effect of jet-mainstream interaction is felt on a much larger spatial scale as the blowing ratio increases. Three characteristic regions of high T.K.E. can be clearly identified at B.R.=1.2, the boundaries of which merge as the blowing ratio decreases. The largest T.K.E. is experienced in the primary entrainment vortex at $z/d \approx 0.2$, followed by outer and inner regions of shear interaction between the jet and the mainstream. The three regions, while still identifiable at B.R.=0.8, tend to merge together at B.R.=0.4.

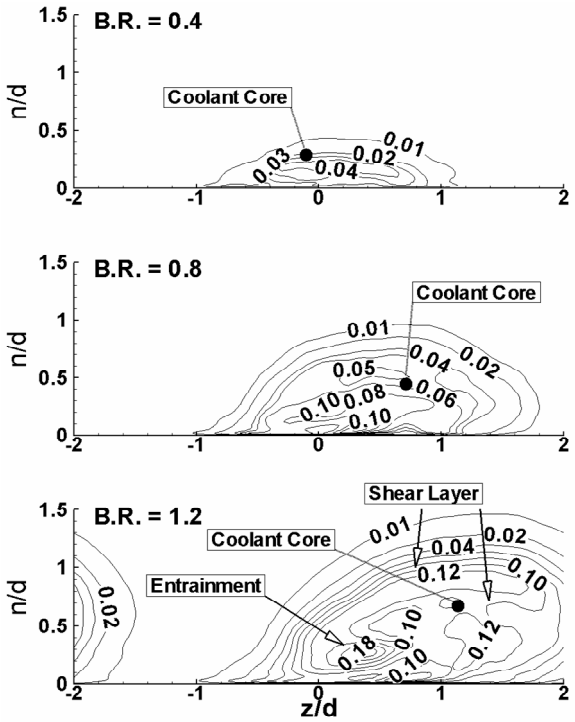

Figure 3.14 - T.K.E. Distribution at s/d=1.0 downstream the hole

Figure 3.15 shows the surface normal distribution at three streamwise locations at a z-location passing through the core of the jet as defined by the location of minimum temperature. At the hole exit, the coolant at B.R. = 1.2 has the most energetic interaction with the mainstream, which results in very high T.K.E at *s/d*=0.0. At *s/d*=1.0, the three peaks in the T.K.E. profiles are attributed to the same three mechanisms as in Figure 3.14, except that the peak in the primary vortex is not fully captured at the z-location of the core. Similar peaks are also identifiable for B.R.=0.8. At *s/d*=0.3, a peak in the very close vicinity of the wall indicates the development of a classical turbulent boundary layer, while the T.K.E. profiles in the jet are now more diffused with a single broad peak at the central core of the jet. The values of T.K.E. increase with blowing ratio indicating a much more intense interaction with the mainstream and greater mixing. This is consistent with previous observations on the evolution of temperature profiles for the three cases.

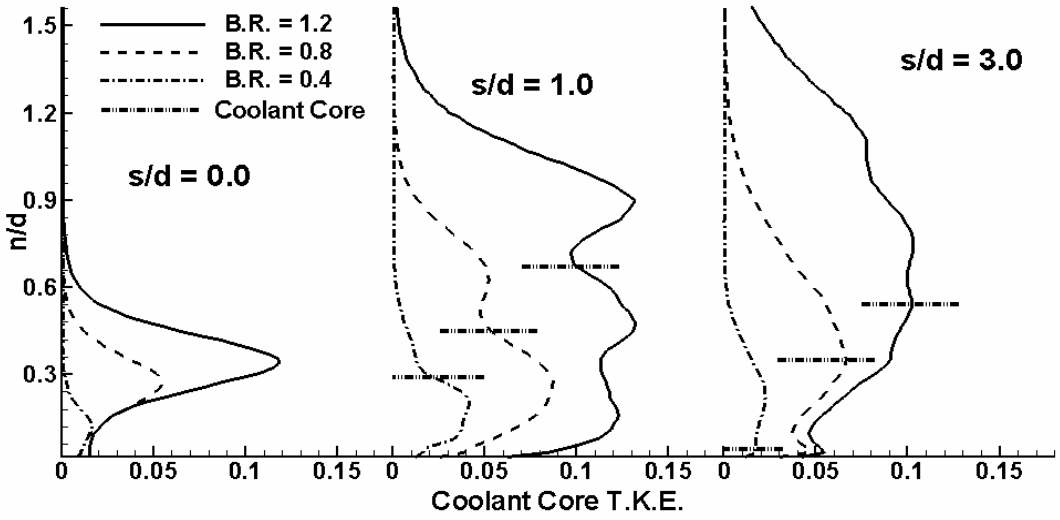

Figure 3.15 - Coolant core T.K.E. downstream of the hole

The distribution of each rms component of velocity is shown in Figure 3.16 at *s/d*=1. The streamwise component of U_{rms} exhibits maximum values in the vicinity of the primary vortex core where most of the entrainment takes place at B.R.=0.4 and 0.8, however the maximum shifts to the outer shear interaction zone between the jet and the mainstream at B.R.=1.2. Similar trends are observed in the V_{rms} and W_{rms} data, which display maximum values as high as 30-40% in the region of the primary entrainment vortex. At B.R.=1.2, as with U_{rms}, there is an increase in both V_{rms} and W_{rms} in the outer shear interaction region between the jet and the mainstream.

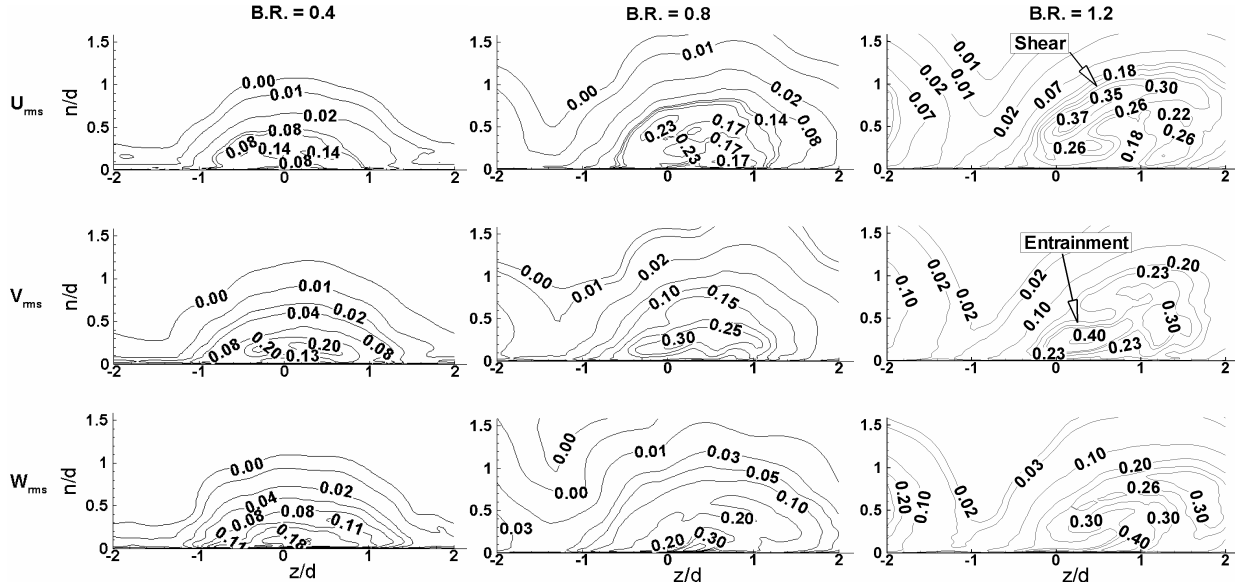

Figure 3.16 - Velocity *rms* distribution at x/d=1.0 downstream of the coolant hole

3.5.6 Adiabatic Effectiveness

Adiabatic effectiveness distribution on the surface is shown in Figure 3.17 for all blowing ratios. As discussed in previous sections, the lateral momentum of the coolant at B.R. = 1.2 pushes it further to the fore-side when compared to the other two cases. At higher blowing ratios, the combined effect of greater jet penetration, larger entrainment and larger turbulent intensities decreases the surface coverage of the coolant and the adiabatic effectiveness. The lowest values of adiabatic effectiveness are located at the aft and leeward edge of the coolant hole, where most of the entrainment occurs. At B.R.=0.4, the effect of the vortex tube at the fore-side can be identified in the surface distribution of effectiveness.

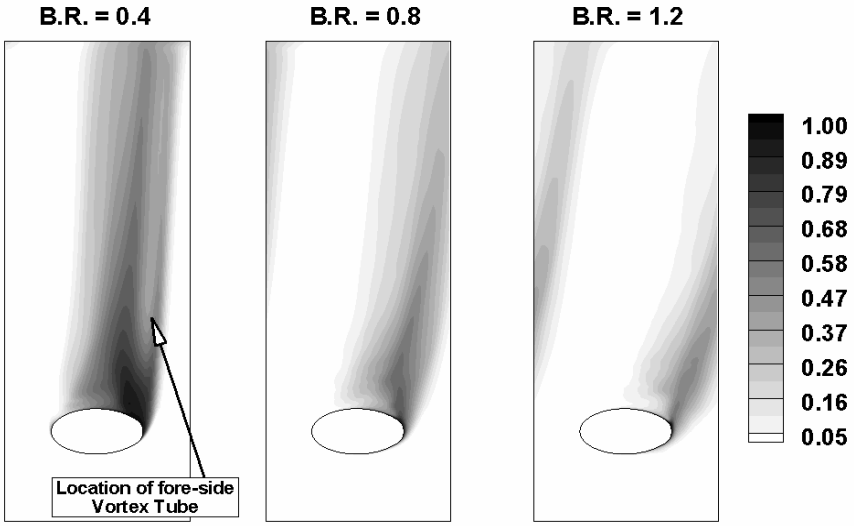

Figure 3.17 - Adiabatic effectiveness distribution

The span-wise averaged effectiveness is shown in Figure 3.18. While good agreement is observed for blowing ratios of 0.4 and 0.8, the calculated effectiveness at B.R. = 1.2 with LES shows lower values than the experimental data of Ekkad et al. (1998). A closer look at the experimental surface distribution of effectiveness in Figure 3.19, indicates a higher effectiveness between jets for B.R.=1.2 than B.R.=0.8, which is inconsistent with the physics. It is our belief that in the transient liquid crystal measurement technique used in the experiments, two-dimensional conduction errors increase with an increase in blowing ratio which adversely affect the measurement of effectiveness and heat transfer coefficients. Another potential source of the discrepancy could be the coolant jet condition. However, the much higher effectiveness at B.R.=1.2 in the experiments would point to a laminar coolant jet, which seems implausible given that a turbulent jet in the computations gives better agreement with experiments at lower blowing ratios. Considering the consistent trends of the numerical results with other studies on the effect

of blowing ratios in the literature [Mehendale and Han (1992), Ekkad et al. (2004)], the large discrepancy at B.R.=1.2 is attributed to increased measurement uncertainty.

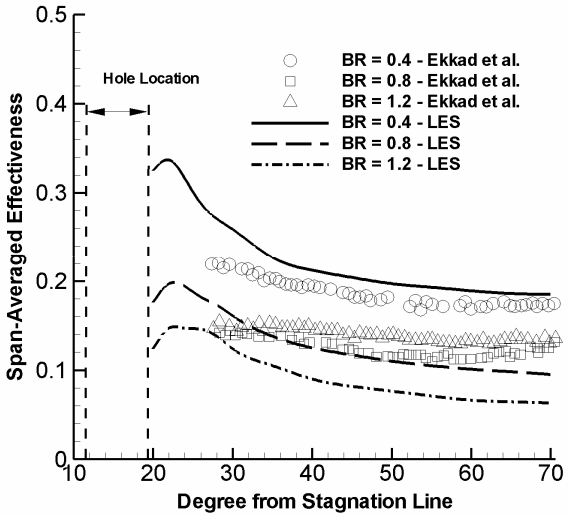

Figure 3.18 - Span-wise averaged adiabatic effectiveness distribution

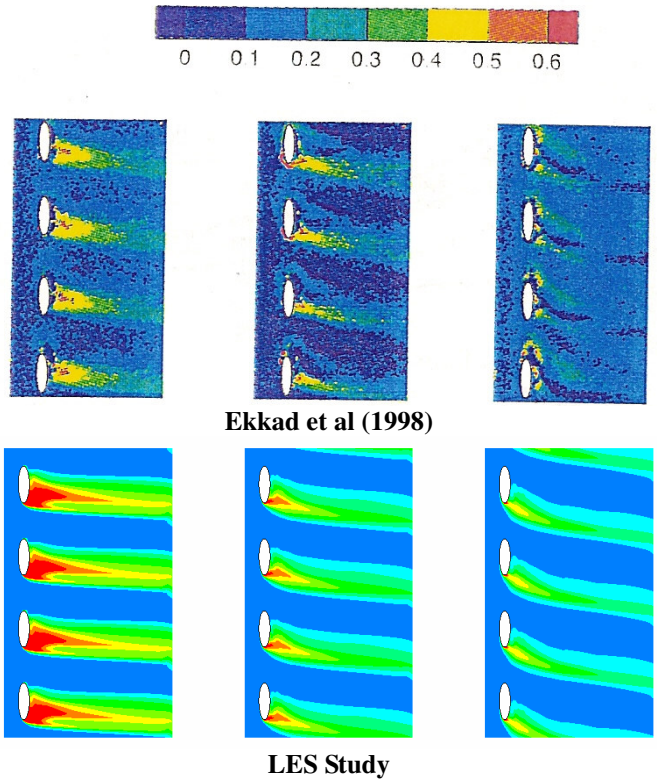

Figure 3.19– LES and Experimental adiabatic effectiveness surface distribution

3.5.7 Heat transfer coefficient

It was shown in a previous study [Rozati and Tafti, (2007c)] that at B.R.=0.4, in addition to the primary vortex, the vortex tubes at the aft- and fore-side of the coolant jet correlated with the regions of high heat transfer. Surface distribution of the Frossling number ($Nu/Re^{0.5}$) is shown in Figure 3.19. With an increase in the blowing ratio, vortex tubes break down immediately into small scale turbulence after formation and do not have an individual effect on the heat transfer coefficient. Instead, with much stronger entrainment, the primary vortex plays a dominant role in heat transfer and regions of high heat transfer coefficient strongly correlate with this structure. The area of the high heat transfer coefficient and magnitude at the aft-side of the jet increase with blowing ratio.

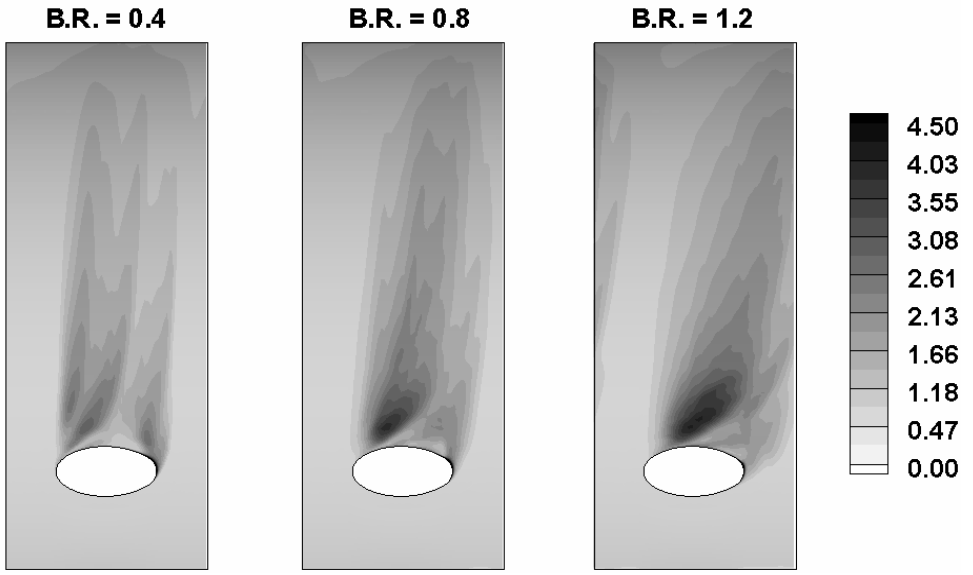

Figure 3.20 - Frossling number distribution

The span-wise averaged Frossling number distribution in Figure 3.20 shows excellent agreement with the experimental data for B.R.= 0.4 and 0.8. In the experimental study, an overall ±4.5% uncertainty in heat transfer coefficient measurement is reported, which is locally even higher close to the coolant hole (up to ±17%). Considering these facts and

the mismatch in adiabatic effectiveness, at B.R.=1.2, an acceptable agreement is achieved (maximum difference with the experimental data is 10% about 1.5d* downstream of the coolant hole).

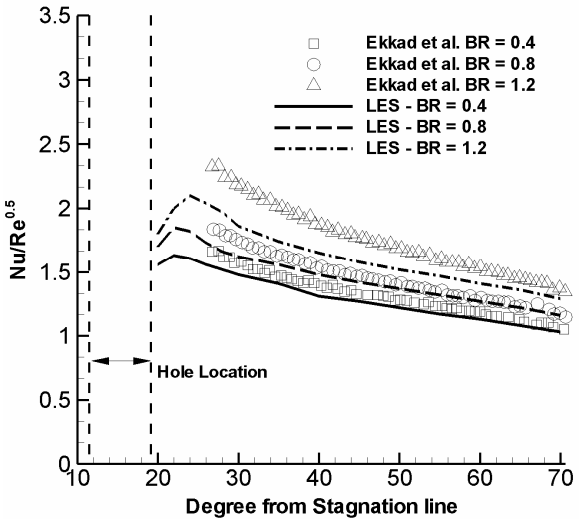

Figure 3.21 - Span-wise averaged Frossling number distribution

3.6. Summary and Conclusions

Film cooling on a cylindrical leading edge with a 30˚ compound angle of injection is simulated with LES technique to analyze the effect of coolant-to-mainstream blowing ratio on the flow field and heat transfer. A new method is used to generate a turbulent coolant jet by placing turbulators in the form of concentric ribs in the coolant pipe to produce turbulent characteristics comparable to that of a fully developed pipe flow at the exit of the coolant into the mainstream flow.

At B.R.=0.4, three types of coherent structures form; primary entrainment vortex at the lee-side of the hole, vortex tubes at the windward side of the coolant hole, some of which extend downstream of the hole, and hairpin vortices typical of turbulent boundary layers produced by the turbulent interaction of the coolant and mainstream downstream of injection. As the blowing ratio increases, flow structures are less coherent and

degenerate quickly into turbulence. At B.R. = 0.8 and 1.2, coherent vortex tubes are no longer discernable, whereas the primary vortex structure gains in strength.

Mixing between coolant and mainstream flow increases considerably with blowing ratio. In all cases, the bulk of the mixing occurs by entrainment which takes place at the leeward aft-side of the coolant jet. This region is characterized by a low pressure core and a primary vortex which draws in mainstream flow from the aft-side of the jet. At B.R.=0.4, the fore and aft vortex tubes also contribute to entrainment. While the bulk of the mixing occurs due to entrainment, turbulent shear interaction between the jet and the mainstream also contributes to the dilution of the coolant jet. The turbulent shear interaction between coolant jet and mainstream increases with blowing ratio as indicated by the high values of turbulent kinetic energy in the core of the jet away from the surface at B.R. = 1.2. Turbulent energy is highest in the core of the primary aft-side vortex.

As a result of the increased mixing between coolant jet and mainstream, coolant coverage on the surface is reduced as the blowing ratio increases. Despite the experimental data, which shows an increase in effectiveness at B.R.=1.2 compared to 0.8, the numerical results shows that the effectiveness decreases at B.R.=1.2, which is consistent with other studies in the literature. Because of the increased turbulent intensities near the surface as a result of the increased entrainment and more intense shear interaction with mainstream, the heat transfer coefficient increases with an increase in blowing ratio. Except the adiabatic effectiveness at B.R. =1.2, the numerical results show good agreement with experiments.

3.7. References

Adami, P., Montomoli, F., Martelli, F., Saumweber, C., 2002. “Numerical investigation of internal cross flow film cooling”. ASME paper No. GT-2002-30171

Azzi, A., Lakehal, D., 2001. “Perspective in modeling film cooling of turbine blades by transcending conventional two-equation turbulence model”. Proceedings of IMECE’01, November 11-16, 2001, New York, NY

Chernobrovkin, A., Lakshminarayana B., 1999. “Numerical simulation and aerothermal physics of leading edge film cooling”. Proc Instn Mech Engrs, Vol. 213, Part A, pp-103-118

Chong, M.S, Perry, A.E., Cantwell, B.J., 1990. A general classification of three dimensional flow fields. Phys. Fluids A 2, No. 5, 765-777.

Cruse, M.W., Yuki, U.M., Bogard, D.G., 1997. “Investigation of various parametric influences on leading edge film cooling”. ASME paper No. 97-GT-296

den Toonder, J. M. J., Nieuwstadt, F. T. M., 1997. Reynolds Number Effects in a turbulent Pipe Flow for Low to Moderate Re. Journal of Physics of Fluids 9, No. 11, 3398-3409.

Ekkad, S.V., Han, J.C., Du, H., 1998. “Detailed film cooling measurement on a cylindrical leading edge model: effect of free-stream turbulence and coolant density”. Journal of Turbomachinery, Vol. 120, pp 799-807

Ekkad, S.V., Ou, S., Rivir, R.B., 2004. ” A transient infrared thermography method for simultaneous film cooling effectiveness and heat transfer measurements from a single test”. Journal of Turbomachinery, Vol. 126, pp 597-603

Germano, M., Piomelli, U., Moin, P., and Cabot, W.H., 1991. A dynamic subgrid-scale eddy viscosity model. Phys. Fluids 3, 1760-1765

Guo, X., Schroder, W., Meinke, M., 2006. “Large-eddy simulation of film cooling flows”. Computers and Fluids, pp 587-60665

Han, J.C., Dutta, S., Ekkad, S., 2000. “Gas turbine heat transfer and cooling technology”. Taylor & Francis, New York, page 179

Honami, S., Shizawa, T., 1992. “Behavior of the laterally injected jet in film cooling: measurement of surface temperature and velocity/temperature field within the jet”. ASME paper No. 92-GT-180

Iourokina, I.V., Lele, S.K., 2005. “Towards large eddy simulation of film cooling flows on a model turbine blade leading edge”. AIAA paper No. 2005-670

Iourokina, I.V., Lele, S.K., 2006. “Large eddy simulation of film cooling above a flat surface with a large plenum and short exit holes”. AIAA paper No. 2006-1102

Johnston, C.A., Bogard, D.G., McWaters, M.A., 1999. “Highly turbulent mainstream effects on film cooling of a simulated airfoil leading edge”. ASME paper No. 99-GT-261

Kelly, G.B., Bogard, D.G., 1991. “An investigation of the heat transfer for full coverage film cooling”. ASME paper No. GT2003-38716

Lakehal, D., Theodoridis, G.S., Rodi, W., 1998. “Computation of film cooling of a flat plate by lateral injection from a row of holes”. International Journal of Heat and Fluid Flow, No. 19, pp 418-430

Lavrich, P.L., Chiappetta, L.M., 1990. “An investigation of jet in a cross flow for turbine film cooling application”. United Technologies Research Center, UTRC report No. 90-04

Lin, Y.-L., Shih, T.I.-P, 2001. “Film cooling of a cylindrical leading edge with injection through rows of compound-angle holes”. Journal of Heat Transfer, Vol. 123, pp 645-654

Liu, K., Pletcher, R.H., 2005. “Large eddy simulation of discrete-hole film cooling in a flat plate turbulent boundary layer”. AIAA paper No. 2005-4944

Mayhew, J.E., Baughn, J.W., Byerley, A.R., 2004. “The effect of free stream turbulence on film cooling heat transfer coefficient and adiabatic effectiveness using compound angle holes”. ASME paper No. GT2004-53230

Mehendale, A.B., Han, J.C., 1992. “Influence of high mainstream turbulence on leading edge film cooling heat transfer”. Journal of Turbomachinery, Vol. 114, pp 707-714

Moin, P. Squires, K., Cabot, W., Lee, S., 1991. A Dynamic Sub-Grid-Scale Model for Compressible Turbulence and Scalar Transport. Phys. Fluids A, 3-11, 2746- 2757.

Mouzon, B.D., Terrell, E.J., Albert, J.E., Bogard, D.G., 2005. “Net heat flux reduction and overall effectiveness for a turbine blade leading edge”. ASME paper No. GT2005-69002

Muldoon, F., Acharya, S., 2004. “Direct numerical simulation of a film cooling jet”. ASME paper No. GT2004-53502

Ou, S., Rivir, R.B., 2001. “Leading edge film cooling heat transfer with high free stream turbulence using a transient liquid crystal image method”. International Journal of Heat and Fluid Flow, No. 22, pp 614-623

Roy, S., Kapadia, S., Heidmann, J.D., 2003. “Film cooling analysis using DES turbulence model”. ASME paper No. GT-2003-38140

Rozati, A., Tafti, D.K., 2006. “Large-Eddy Simulations of leading edge film cooling: analysis of flow structures, effectiveness, and heat transfer coefficient”. Submitted (under review) to International Journal of Heat and Fluid Flow

Rozati, A., Tafti, D.K., 2007a. “Large eddy simulation of leading edge film cooling part-I: computational domain and effect of coolant inlet condition”. ASME paper No. GT2007-27689

Rozati, A., Tafti, D.K., 2007b. “Large eddy simulation of leading edge film cooling part-II: Heat transfer and effect of blowing ratio”. Journal of Turbomachinery, *in press*

Rozati, A., Tafti, D.K., 2007c. “Large-Eddy Simulations of Leading Edge Film Cooling: Analysis of Flow Structures, Effectiveness, and Heat Transfer Coefficient”. International Journal of Heat and Fluid Flow, in press

Saumweber, C., Schulz, A., Witting, S., 2003. “Free stream turbulence effects on film cooling with shaped holes”. Journal of Turbomachinery, Vol. 15, pp 65-73

Schmidt, D.L., Bogard, D.G., 1996. “Effects of free stream turbulence and surface roughness on film cooling”. ASME paper No. 96-GT-462

Shyy, W., He, X., Thakur, S., 1999. “Jets and free stream interaction around a low-Reynolds-number airfoil leading edge”. Numerical Heat Transfer, Part A, No. 35, pp 891-902

Sinha, A.K., Bogard, D.G., Crawford, M.E., 1991. “Film cooling effectiveness Downstream of a single row of holes with variable density ratio”. Journal of Turbomachinery, Vol. 113, pp 442-449

Tafti, D.K., 2001. “GenIDLEST – A scaleable parallel computational tool for simulating complex turbulent flows”. Proc. ASME Fluid Engineering Division, FED-vol. 256, ASME-IMECE, New York, 2001

Theodoridis, G.S., Lakehal, D., Rodi, W., 2001. “Three-dimensional calculations of a flow field around a turbine blade with film cooling injection near the wall”. Flow, Turbulence and Combustion, No. 66, pp 57-83

Tyagi, M., Acharya, S., 2003. “Large eddy simulation of film cooling flow from an inclined cylindrical jet”. Journal of Turbomachinery, Vol. 125, pp 734-742

York, D.W., Leylek, J.H., 2002. “Leading-edge film-cooling physics: Part-I Adiabatic effectivemess”. ASME paper No. GT-2002-30166

York, D.W., Leylek, J.H., 2002. “Leading-edge film-cooling physics: Part-I Adiabatic effectivemess”. ASME paper No. GT-2002-30167

Chapter 4 : Effects of Syngas Ash Particle Size on Deposition and Erosion of a Film Cooled Leading Edge[7]

Abstract

The paper investigates the deposition and erosion caused by Syngas ash particles in a film cooled leading edge region of a representative turbine vane. The carrier phase is predicted using Large Eddy Simulation for three blowing ratios of 0.4, 0.8 and 1.2. Three ash particle sizes of 1, 5, and 10 microns are investigated using Lagrangian dynamics. The 1 micron particles with momentum Stokes number St = 0.03 (based on approach velocity and cylinder diameter), follow the flow streamlines around the leading edge and few particles reach the blade surface. The 10 micron particles, on the other hand with a high momentum Stokes number, St = 3, directly impinge on the surface, with blowing ratio having a minimal effect. The 5 micron particles with St=0.8, show the largest receptivity to coolant flow and blowing ratio. On a mass basis, 90% of deposited mass is from 10 micron particles, with 5 micron particles contributing the other 10%, and 1 micron particles making a negligible contribution to deposition. Overall there is a slight decrease in deposited mass with increase in blowing ratio. About 0.015-0.03% of the total incoming particle energy can potentially be transferred as erosive energy to the surface and coolant hole, with the contribution coming from only 5 micron particles at B.R. = 0.4 and 0.8, and both 5 and 10 micron particles at B.R.=1.2.

[7] This chapter is submitted for publication as an article to ASME Turbo Expo 2008, "Effects of Syngas Ash Particle Size on Deposition and Erosion of a Film Cooled Leading Edge", *under review*, Rozati, A., Tafti, D.K., Copyright ASME, 2008

Nomenclature

B.R.	Blowing ratio (u_∞/u_j)
C_D	Drag Coefficient
d	Coolant hole diameter, particle diameter
D	Leading edge diameter
F	Forces acting on particles
h	convective heat transfer coefficient
h_r	radiative heat transfer coefficient
k	Thermal conductivity
l	Coolant pipe length
L_c	length scale
m	mass
Nu	Nusselt number
p	Coolant hole span-wise pitch
P	Pressure
Re	Reynolds number ($u_\infty D/\nu$)
Re_p	Particle Reynolds number ($[u_\infty-u_p]d_p/\nu$)
St	Stokes number
t	time
T	temperature
U,u	velocity
V	particle impact velocity
x	Particle location

ρ Density

τ_v Momentum response time

τ_{conv} Convective response time

τ_{rad} Radiative response time

μ Dynamic viscosity

θ non-dimensional temperature

Subscripts

f Fluid

j Coolant

∞ Free Stream

Subscripts

p Particle

4.1. Introduction

A severe operating environment and residual foulants in fuels derived from alternative sources such as coal and biomass, necessitates taking appropriate measures to reduce the detrimental effects of Deposition, Erosion, and Corrosion (DEC) on the gas turbine engine lifespan. In general, particulate matter in the form of dust, sand, and combustion products pose a severe threat to the durability of hot gas path engine components over a prolonged life span of 1000s of operational hours. According to Wenglarz (1985), the particulate matter transports to the blade surface through various mechanisms: i) inertial impaction, due to the inertia of the particles which is dominant when the particle diameter is more than a few microns; ii) turbulent eddy diffusion,

where the particles are drawn into the turbulent eddies and transported to the surface; iii) thermophoresis, where the temperature difference between the cooled surface and hot gases drives the particles with diameters in the submicron range as large as 0.5 micron; iv) brownian diffusion by random particle impacts with gas molecules for particle diameters in the range of 0.05-0.1 microns. The damage to the blade surface is not only dependent on the impact mechanism of the particles, but also on particle condition upon impact. Particles can be in the solid, molten, or condensed liquid phase. Studies have shown that corrosion most likely takes place when condensed combustion products impact the surface in the presence of film cooling jets [Krishnan et al. (2003)]. Erosion and deposition are competitive processes where the dominancy of each depends on the fraction of molten particles in gas. This fraction, in turn, is affected by the particle material composition and gas temperature.

Hamed (1988) chose sand particle diameter size of 150 micron to represent the dust laden atmosphere in helicopter engines, and 15 micron diameter ash particles to represent fuel combustion products. Trajectory of the particles showed that while the sand particles deflected from the top blade pressure side and impacted on the bottom blade suction side, the ash particles just hit the pressure side of one blade at the initial row. They also showed the surface impact distribution of sand and fly ash on a two stage engine on the pressure and suction side. In a study by Raubenheimer (1990) on land based industrial and marine gas turbine filtration, particles in the range of 0.001-1μm were found to be products of combustion (permanent pollutants). Particles in range of 1-1000μm were ingested from the outside (temporary pollutant), such as sand. Smialek et al. (1992) studied the deposition and composition of the particles ingested in helicopter engines

which operate in the Persian Gulf. Their analysis concluded that the particles found in the cooling passages are in the size range of 1-10μm and of the same material composition of small sand particles. The melting temperature of these deposits was measured at 1135˚C, based on which, the sand is expected to be molten in the external hot gas path and solid in the coolant flow.

A series of experimental studies have been conducted in the University of Cincinnati [Hamed and Tabakoff (1994)]. In these studies the rate of erosion was measured for various blade and coating materials based on different particle speed and impingement angle. They also measured the restitution coefficient of the particle which measures the amount of kinetic energy lost by the particle during impact. Particle dynamics and trajectory were modeled and simulated numerically. In general, they found that the small sized particles are more affected by the flow field and approached the gas velocity quickly, while the larger particles are affected by the blade passage geometry. These larger particles generally impacted the suction side of the blade surface due to their negative incidence angle. They also observed that the larger particles bounced back and forth between the blades before they passed through the blade passage. Overall erosion increased the blade tip clearance and blade roughness. Deposition in the cooling flow passage and cooling holes on the blade surface and leading edge leads to blockage of the cooling passages and reduced the efficiency of the internal and film cooling of the blade.

Study of Metwally et al. (1995) predicted the blade erosion in an automotive gas turbine engine. They observed that the number of impacts was more significant on the pressure side of guide vane, stator, and rotor blades. On the suction side, impacts mostly took place at the leading edge of the blades. They quantified the blade mass erosion rate

by ‘blade mass removal per unit area of the blade surface per unit mass of the ingested particles’. The results of erosion rate reduced considerably for the coated blade. They also reported the frequency of impact, impact angle and impact velocity, which had almost similar patterns for coated and uncoated blades. The maximum rate of erosion for the rotor blade was observed at the trailing edge area.

Walsh et al. (2006) studied the internal blockage of a single array of cooling holes to investigate the effects of pressure ratio (total coupon pressure to atmospheric pressure), sand amount and distribution, number of holes and metal temperature. Increasing the pressure ratio decreased the chance of blockage by increasing the velocity of the particles. Increasing the amount of sand naturally increased the blockage. The most effective parameter was found to be the coupon metal temperature. As the temperature exceeds 1000˚C, particles would be mostly molten and adhere to the surface.

Bons et al. (2005) investigated the deposition rate and thickness for ash from different alternative synfuels: coal, petroleum coke, and biomass. Results showed that the same distribution and size of the particle (10-20 microns) results in an order of magnitude larger deposition for coal and petcoke when compared to biomass. The biomass deposit appeared to adhere to the surface while coal and petcoke deposit could be removed from the surface after shutdown of the system. However, this characteristic could be specific to the operating conditions of the conducted tests in the study. For all alternative fuels, evidence of deposit penetration in to the TBC was found. Crosby et al. (2007) studied the “Effects of particle size, gas temperature, and metal temperature on high pressure turbine deposition in land based gas turbine from various synfuels”. Two synfuels were selected for the tests. To study the effect of particle size, four different particles diameters were

selected. The target coupon was thermal barrier coated (TBC). As the particle became larger, the TBC spallation became more significant. Particle deposition rate decreased with decrease of the gas temperature (temperature threshold was 960˚C). As the surface was cooled, the deposition to the TBC increased.

Sundaram and Thole (2006) studied the effects of deposition upstream and downstream of the coolant hole. They found that thin deposition downstream of the leading edge endwall cooling hole augmented the adiabatic effectiveness. They speculated that this enhancement was due to the limited lift off of the coolant jet as a result of the deposits. With increase in height of the deposition, adiabatic effectiveness decreased. Coolant hole blockage and TBC spallation both decreased adiabatic effectiveness. This negative effect increased with increase in number of partially blocked holes or percentage of spallation. Shah and Tafti (2007) investigated potential erosion and deposition of particles in an internal turbine blade ribbed channel. The fully developed turbulent channel flow was predicted by LES and the particle dynamics were investigated in a Lagrangian frame work. They presented the impact distribution of the particles, impingement velocity and angle, and fractional energy transfer from the particle for each surface (of channel and rib).

From the literature review it is evident that all past studies pertaining to deposition have assumed *ad hoc* or field observed blockages or deposition patterns. There has been no study investigating the detailed dynamics of deposition formation under representative hydrodynamic and thermal conditions in the leading edge region of a turbine blade with film cooling jets.

4.2. Objective

The present study is the first investigation of the complex two-phase dynamics of deposition formation of residual Syngas ash particulate matter in the leading edge region of a simulated vane with film cooling. The study combines high resolution LES calculations [Rozati and Tafti (2007a-b)] for the carrier phase with detailed Lagrangian particle dynamics [Shah and Tafti (2007)]. The effect of jet blowing ratio and particle size or particle Stokes number on deposition and erosion is presented for three particle diameters of 1, 5 and 10 microns with three coolant-to-mainstream blowing ratios of 0.4, 0.8 and 1.2.

4.3. Problem Definition

4.3.1 Computational Domain, Boundary Conditions and Mathematical Model for Carrier Phase

The physical system and conditions which are simulated are defined in Table 4.1. In the computational domain, the leading edge of the blade is represented by a semi-cylinder with a flat after body. Coolant is injected into the mainstream through coolant jets with 30˚compound angle injection. Two rows of film cooling holes are located at ±15˚ from the stagnation line. The diameter of the cylindrical leading edge and the free stream velocity are selected as the characteristic length and velocity scales, respectively, to define the free stream Reynolds number of 100,000. The non-dimensional temperature is defined as $(T^*-T^*_j)/(T^*_\infty-T^*_j)$, where T^*_∞ is the free-stream temperature and T^*_j is the coolant jet temperature. The blade surface is assumed adiabatic, thereby only the coolant

and mainstream temperature and their interaction affect the surface temperature distribution. A periodic boundary condition is assumed in the span-wise direction which represents adjacent holes in the row. A symmetry boundary condition is applied along the stagnation line. Figure 4.1 illustrates the computational domain. The grid consists of 72 hybrid structured/unstructured blocks with a total of 3,866,624 computational cells.

Table 4.1 - Flow properties and leading edge-jet geometry

Leading Edge Geometry	
Blade leading edge diameter (D^*) [m]	0.01
Coolant pipe diameter (d^*), [m]	6.3×10^{-4}
Span-wise pitch (p^*/d^*)	4
Flow Properties	
Free stream velocity (u^*_∞), [m/s]	118
Free stream temperature (T^*_∞), [K]	1500
Free stream pressure (P^*_∞), [atm]	20
Free stream density (ρ^*_∞), [kg/m^3]	4.7
Coolant temperature (T^*_j), [K]	800
Coolant-to-mainstream density ratio	1
Coolant-to-mainstream blowing ratio (u^*_j/u^*_∞)	0.4,0.8,1.2

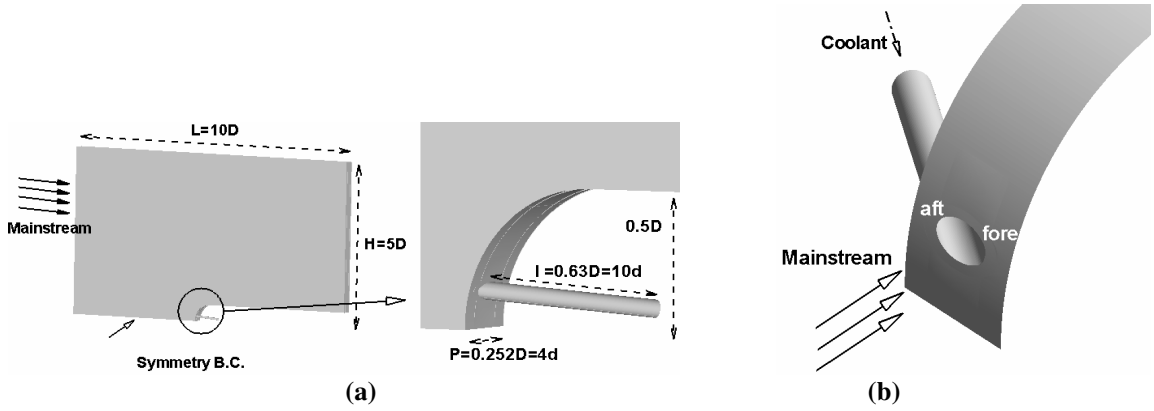

Figure 4.1 - (a) Computational domain; (b) Close-up view of compound angle film cooling jet

The transformed non-dimensional time-dependent incompressible Navier-Stokes and energy equations are solved in a generalized body-fitted coordinate system using Large Eddy Simulations. The turbulent eddy-viscosity is obtained by the dynamic Smagorinsky

model. The governing equations of momentum and energy are discretized with a conservative finite volume formulation using a second-order central difference scheme. The temporal advancement is performed with a two-step, semi-implicit predictor-corrector algorithm. The adequacy of grid resolution, accuracy of the results, validity of the assumptions and boundary conditions are discussed and established in earlier publications by the authors [Rozati and Tafti (2007a-b)].

4.3.2 Properties, Initial Conditions and Mathematical Model of Dispersed Phase Ash Particles

Properties of Syngas ash vary significantly with coal composition and plant-operating conditions. The common materials in coal ashes are (by wt): 5-70% Al_2O_3, 0-50% SiO_2, 0-70% Fe_2O_3 0-40% CaO, 0-10% MgO, 0-6% K_2O, 0-10% P_2O_5, 0-10% Na_2O, 0-3% TiO_2 and 0-24% SO_3 [Seggiani and Pannocchia (2003)]. In the current study three ash particle sizes are investigated, 1, 5 and 10 microns with representative density ρ_p=2500 kg/m^3 and specific heat C_p = 250 J/kgK. An important element in ash deposition is its fusibility which is characterized by the initial deformation temperature (IDT), softening temperature (ST), hemispherical temperature (HT), and fluid temperature (FT) [Seggiani and Pannocchia (2003)]. These temperatures vary up to 300-400^{o}C between different ash samples. In the present study a ST of 1100˚K is assumed. It is assumed that ash above this temperature is in a state which facilitates its sticking or depositing on the surface. Any ash particle below this temperature is taken to be in a solid phase and is considered erosive. Erosive ash particles are modeled with elastic collisions with the surface. The velocity and angle of the impact are used to calculate the energy of the impact which could potentially contribute to erosive wear of the surface.

The particle equation of motion is integrated in a Lagrangian frame of reference. The model implementation in an unstructured multiblock multiprocessor framework and validation in turbulent channel flow has been reported in [Shah (2005)]. Application to particulate transport and erosion potential in ribbed internal cooling ducts has been reported in [Shah and Tafti (2007)]. The following equations are used to calculate the particle location and velocity:

$$m_p^* \frac{du_i^{*p}}{dt^*} = \sum F_i^{*p}$$
$$\frac{dx_i^{*p}}{dt^*} = u_i^{*p} \tag{4.1}$$

The typical forces acting on the particle are drag, gravitational forces, Saffman lift force caused by the shear of the surrounding fluid, added mass, pressure and viscous forces, Basset forces due to fluid acceleration, Magnus lift force due to particle rotation, forces due to interparticle collisions, Brownian motion, and thermophoresis forces due to temperature gradients.

For the current study, Brownian motion and thermophoresis forces, which are important only for submicron sized particles, are neglected for the range of particle sizes investigated in this study (1-10 microns). Basset forces are also negligible due to the substantially greater density of ash particle compared to the carrier phase. Elgobashi and Truesdell (1992) showed that for particles with considerably large particle-fluid density ratio, the only significant forces are the Stokes drag, the buoyancy, and the Basset forces, and that the Basset force was always an order of magnitude smaller than the drag and buoyancy forces. Saffman lift force [Saffman (1965)] is caused by the shear of the surrounding fluid which results in a non-uniform pressure distribution around the particle.

This force assumes non-trivial magnitudes only in the viscous sublayer. McLaughlin (1989) showed that even in the viscous sublayer it is an order of magnitude smaller than the normal component of the Stokes drag force. Wang et al. (1997) also have shown that neglecting the lift force results in a slight decrease in the deposition rate. Due to the dilute suspension of particle laden flow in the turbine inlet section (roughly 0.02 ppmw), the interaction between the particles can be ignored. Experiments by Kulick et al. (1994) and Kaftori et al. (1995) have shown that for low volume fractions the turbulence modifications due to the effect of particles on the flow are also negligible. Also, in the near-wall region where the particle concentration may be locally large, the turbulence intensities are only modified by a very small amount and can be neglected [Marchioli and Soldati (2002)]. Therefore, particles effects on the fluid turbulence are neglected in the current study.

With the stated assumptions, the drag force is considered to be the dominant component. The simplified equation of particle motion can be written as:

$$\frac{du_i^{*p}}{dt^*} = -\frac{\rho_f^*}{\rho_p^*}\frac{3}{4}\frac{C_D}{d_p^*}\left|u^{*p} - u^{*f}\right|\left(u_i^{*p} - u_i^{*f}\right) \tag{4.2}$$

The drag coefficient is given by Clift et al. (1978) and is valid for particle Reynolds number up to 700:

$$C_D = \frac{24}{\mathrm{Re}_p}\left(1 + 0.15\,\mathrm{Re}_p^{0.687}\right)$$

Using the free-stream velocity u^*_∞ and the leading edge diameter D^* as the characteristic velocity and length scale, respectively, same as the carrier phase, the particle equations take the non-dimensional form:

$$\frac{du_i^p}{dt} = -\frac{1}{St_p}\left(1+0.15\,\mathrm{Re}_p^{0.687}\right)\left(u_i^p - u_i^f\right)$$
$$\frac{dx_i^p}{dt} = u_i^p \qquad (4.3)$$

where St_p is the particle Stokes number, which is the ratio of the particle time scale τ_v^* to the flow time scale (D^*/u^*_∞),

$$St_p = \frac{\tau_v^*}{D^*/u_\infty^*} = \frac{\rho_p^* d_p^{*2}/18\mu^*}{D^*/u_\infty^*}$$

A large Stokes number indicates that the particle's inertial response to the surrounding fluid is slow, whereas a Stokes number much smaller than unity indicates that the particle closely follows changes in the surrounding carrier phase.

The characteristic equation of particle heat transfer between the two phases is:

$$\frac{dT^{*p}}{dt^*} = \frac{6h^*}{\rho_p^* c_p^* d_p^*}\left(T^{*f} - T^{*p}\right) + \frac{6\varepsilon\sigma}{\rho_p^* c_p^* d_p^*}\left(\left(T_\infty^*\right)^4 - \left(T^{*p}\right)^4\right) \qquad (4.4)$$

where the first term constitutes the convective heat transfer between the particle and the carrier phase, and the second term constitutes radiative heat transfer which assumes black body radiation between the particle and the surroundings. The convective heat transfer coefficient is obtained from the Ranz and Marshall correlation [Incropera et al. (2007)] given by:

$$\frac{h^* d_p^*}{k_f^*} = Nu = 2.0 + 0.6\sqrt{\mathrm{Re}_p}\,\mathrm{Pr}^{1/3}$$

Appropriate non-dimensionalization of equation (4.4) results in:

$$\frac{d\theta^p}{dt} = \frac{1}{St_{conv}}\left(\theta^f - \theta^p\right) + \frac{1}{St_{rad}}\left(1-\theta^p\right) \qquad (4.5)$$

where θ, the non-dimensional temperature is given by $(T^*-T^*_j)/(T^*_\infty-T^*_j)$, and the thermal convective and radiative Stokes numbers are given by:

$$St_{conv} = \frac{\tau^{*p}_{conv}}{D^*/u^*_\infty} = \frac{(\rho^*_p c^*_p d^*_p)/6h^*}{D^*/u^*_\infty}; \qquad St_{rad} = \frac{\tau^{*p}_{rad}}{D^*/u^*_\infty} = \frac{(\rho^*_p c^*_p d^*_p)/6h^*_r}{D^*/u^*_\infty}$$

,respectively (h_r^* is the radiative heat transfer coefficient). Similar to the momentum Stokes number, the thermal Stokes numbers represent the thermal inertia of the particle to heat transfer from the carrier phase through convection and radiation.

Table 4.2 lists the particle Stokes numbers based on the outer flow time scale (D^*/u^*_∞)[8]. At Stokes numbers much less than unity, the particle velocity and temperature respond rapidly to changes in the carrier phase. Based on the values of St_{rad} and equation (4.5), one can conclude that the effect of radiation is much smaller than convection in the energy equation. The particle equations are integrated using a third-order Adams-Bashforth method.

Table 4.2 - Particle diameter and Stokes numbers

d_p (micron)	St_p	St_{tconv}	St_{rad}[9]
1	0.029	0.006	9.635
5	0.739	0.154	48.17
10	2.955	0.615	96.35

A total number of 351,609 particles are injected for each particle size. These particles are uniformly injected at 0.5*D* upstream of the blade leading edge in a band of *p*×0.3*D*, such that their direct line of travel cover the leading edge surface from the stagnation line to 3*d* downstream of the coolant hole. However, as the particles approach the blade surface, their distribution elongates with the flow in the vicinity of the stagnation line,

[8] *The convective Stokes number is calculated assuming Nu ≈ 2 for Re_p<1.*

[9] *These are the minimum possible values of radiative Stokes number when $T_p=T_\infty$.*

such that they cover up to 7d downstream of the coolant hole. At injection, the particles are in equilibrium with the carrier phase, which is close to the free-stream condition of uniform velocity u_∞ and temperature θ_∞. This is a close approximation to the actual conditions at which the particles would approach the leading edge.

The injected particles result in a loading of 0.52 milligrams of syngas ash particles in the calculation domain. Extrapolating the small spatial extent of the injection of particles in the calculation domain to a power generation turbine section with approximately 45 stator vanes and about 20 film cooling holes in a row across the height of the vane, the computational particle loading roughly represents 50 seconds of operating time of a 11MW gas turbine (such as GE10) with ash ingestion of 0.02 ppmw. The total particle mass for this gas turbine for total operation time of 10,000 hrs is roughly 34.2kg.

4.4. Results

There are two separate mechanisms which affect the deposition and erosion at the leading edge. The first is the interaction of the particles with the outer flow around the cylindrical leading edge and is governed by the outer fluid time scale (D^*/u^*_∞) or the outer Stokes number. The interaction determines whether the particles are transported to the vicinity of the leading edge surface and the coolant jets. The second is the additional interaction of those particles near the surface with the coolant jets, which is determined by the blowing ratio and/or the time scale of turbulent eddies.

For particles with large outer Stokes numbers, if the inner time scale is smaller than the outer time scale, the particles exhibit even larger Stokes numbers in the inner region. Hence it is very likely that particles with high Stokes numbers which penetrate to the surface will result in inertial impact unless the jet blowing ratio is high enough to slow

the particles enough to avoid impaction. Particles with outer Stokes numbers much less than unity, with little inertia, react to the change in flow path around the leading edge almost instantaneously and follow the flow streamlines, eliminating any contact with the surface. However, in this case, particles traveling close to the surface are receptive to the influence of turbulent eddies generated by coolant jet-mainstream interaction. Between the two extremes is a range of particles which have just enough inertia to penetrate into the inner layer but which are also receptive to turbulent eddies in the inner layer.

Except for particles with large Stokes numbers which are completely driven by inertia, the dynamics of deposition and erosion is strongly influenced by the turbulent structure of the coolant-jet mainstream interaction. A key feature of leading edge film cooling flow which influences the flow field and heat transfer is the entrainment of the hot mainstream gases from the aft-side of the coolant jet. The entrainment, which is due to the formation of a low pressure region immediately downstream of the coolant hole, is shown in Figure 4.2. To show the three-dimensional nature of entrainment, the time averaged streamlines are imposed on the temperature iso-surface with value of 0.7 (to represent the coolant) at B.R.=1.2. As illustrated, the aft-side vortex structure draws the mainstream flow underneath the coolant. At this blowing ratio the low pressure region is strong enough to create a slight reversed flow, where the mainstream is drawn towards the fore-side and leeward edge of the coolant hole. In spite of being weaker, the dynamics of entrainment at B.R. = 0.4 and 0.8 follows the same general pattern. The entrainment of hot gases also affects the dynamics of deposition and erosion on the surface.

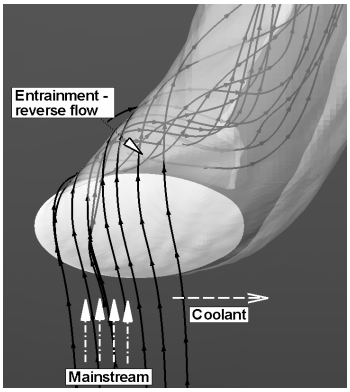

Figure 4.2 - Entrainment of hot mainstream

4.4.1 Deposition

Figure 4.3 shows the surface distribution of the deposited particles. The contours are indicative of the percentage of injected particles of each size that impact the surface and result in deposition. An immediate observation is the relative insensitivity of deposition pattern and density of 10 micron particles on the presence of the coolant jet and the blowing ratio. These particles are driven by their free stream momentum and due to their relatively large Stokes number, (both momentum and thermal) they neither react to the flow field nor to the temperature near the leading edge and more than 85% of the injected particles deposit on the surface (Figure 4.6). Only at B.R.=1.2, a small distortion in the surface deposition is observed.

For the 1 micron particles, because of the low Stokes number, the particles follow the outer flow streamlines around the leading edge. Particles traveling in the vicinity of the coolant jet-mainstream interaction region are easily entrained and this interaction becomes the driving force for deposition. As the blowing ratio increases and the jet penetrates more into the mainstream, it entrains more particles to the surface, which

increases deposition especially at the aft side of the coolant hole as indicated by the entrainment dynamics in Figure 4.2.

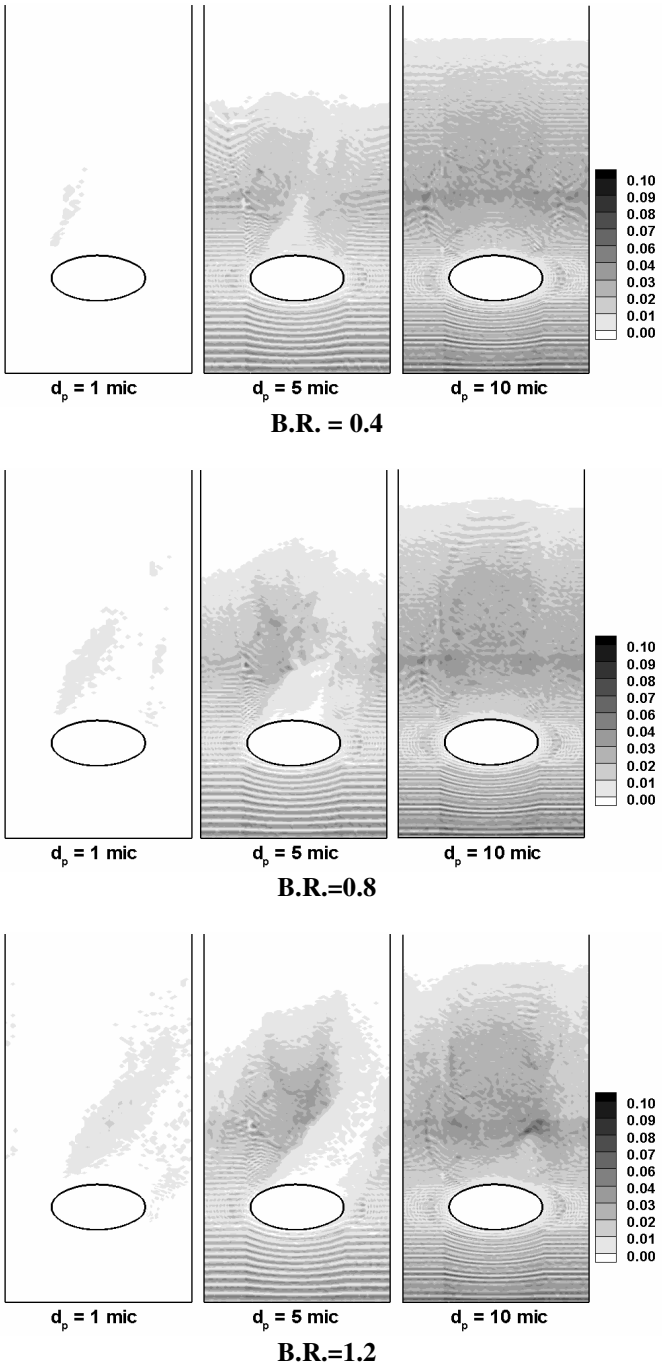

Figure 4.3 - Distribution of %deposited particles of each particle size on the surface

The 5 micron particles are also sensitive to the blowing ratio. With an increase in blowing ratio, the momentum of the coolant succeeds in pushing some particles away from the surface in its direct path; at the same time, entrainment on the aft-side results in more deposition in this region. It is noteworthy that an increase in blowing ratio increases the number of deposited 1 micron particles, but decreases this number for 5 and 10 micron particles.

Deposition in the coolant hole is also dependant on the particle size. 1 micron particles result in no deposition in the hole. Their small momentum Stokes number prevents them from having any contact with the hole surface. Results in Figure 4.4 shows that the 10 micron particles have the highest rate of deposition on the foreside-downstream wall of the coolant hole, which is in the direct line-of-sight of the oncoming free stream flow. These particles carry their mainstream momentum and enter the coolant hole. Due to their high thermal Stokes number and small residency time within the coolant, they maintain a temperature higher than the ST at impact and mainly result in deposition rather than any erosion (only at B.R.=1.2 do some of the particles become erosive). The rate of deposition decreases slightly with the increase in blowing ratio. The 5 micron particles result in both deposition and erosion in the hole. Deposition occurs in the same place as for the 10 micron particles, and decreases considerably with an increase in the blowing ratio.

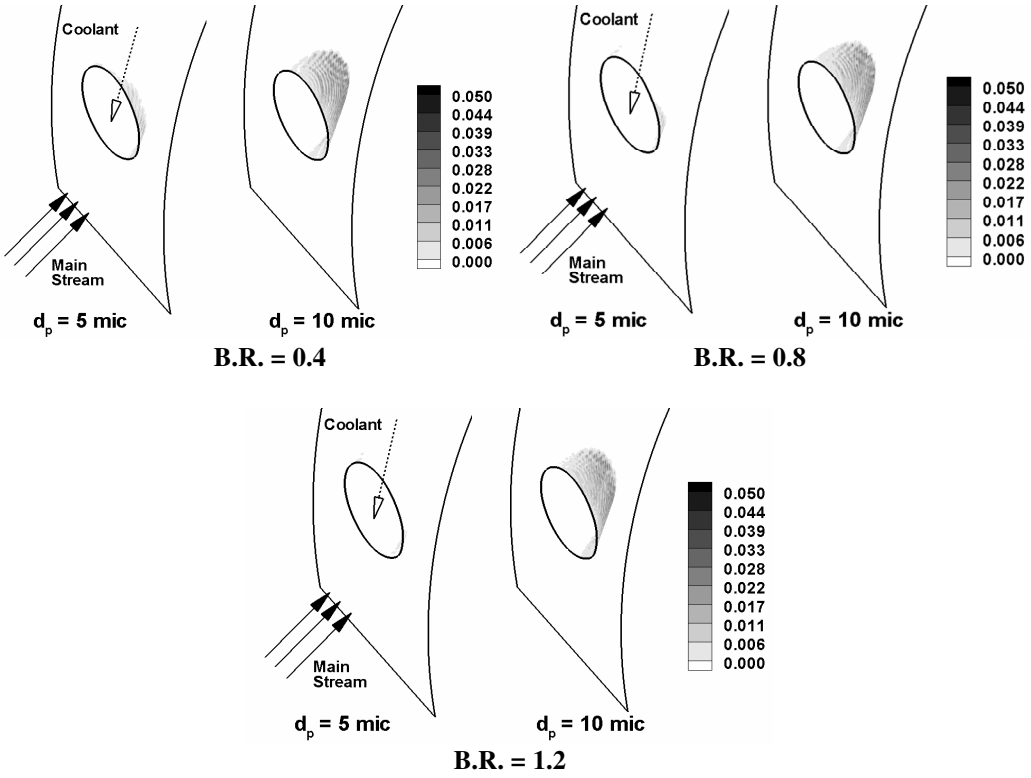

Figure 4.4 - Distribution of %deposited particle of each particle size in the coolant hole

Table 4.3 summarizes the above results by listing the amount of deposited mass on the blade surface and in the coolant hole out of the total injected particle mass. Based on these results, 4-5% of the incoming particle mass (injected in front of the leading edge) deposits in the coolant hole, and 80% deposits on the blade surface. Detailed results show that 10 micron particles account for most of coolant hole deposition, whereas 1 micron particles do not deposit in the hole. As blowing ratio increases, the deposition is reduced for all surfaces, although this reduction is not significant.

Table 4.3 - Deposited mass in the leading edge region

B.R.	0.4	0.8	1.2
Total Injected Mass (mg)	0.518	0.518	0.518
Mass Deposited in the Coolant Hole(mg)	0.0262	0.0250	0.0233
Mass Deposited on the Surface(mg)	0.4154	0.4112	0.4013
Total Deposited Mass (mg)	0.4416	0.4362	0.4246

Figure 4.5 shows the percentage mass deposition contribution of each particle size to the total deposited mass at each blowing ratio. These results show that 93-94% of the total deposited mass consists of 10 micron particles, 5-6% of 5 micron particles, and less than 1% of 1 micron particles. Although the mass deposition of 1 micron particles is insignificant, the effect of the blowing ratio is more evident for these particles. Blowing ratio also affects the 5 micron particles but has a minimal impact on 10 micron particles.

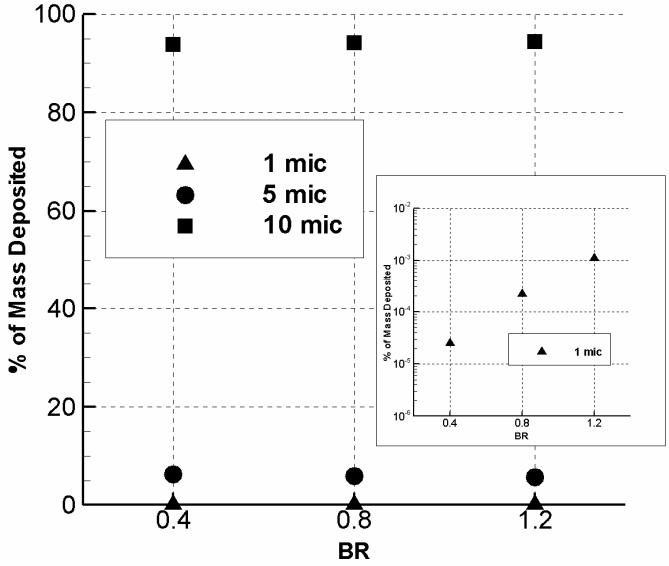

Figure 4.5 - Percentage contribution of each particle size to total deposited mass at each blowing ratio

To obtain a clearer picture of how the particles react to the main flow and near coolant flow structures, the portion of deposited particles (by %numbers not %mass) is shown in Figure 4.6. The data shows that 41-47% of the 5 micron particles deposit on the surface, but due to the particle size, they only account for 5% of the deposited mass. Increase in blowing ratio increases the number of deposited 1 micron particles by nearly two orders of magnitude. However, due to their extremely small mass, they have an insignificant effect on the total deposition, which was shown in Figure 4.5. Results also

show that unlike 1 micron particles, 5 and 10 micron particles have slightly less number of particles depositing as blowing ratio increases, due to a stronger coolant jet which blow them away from the surface.

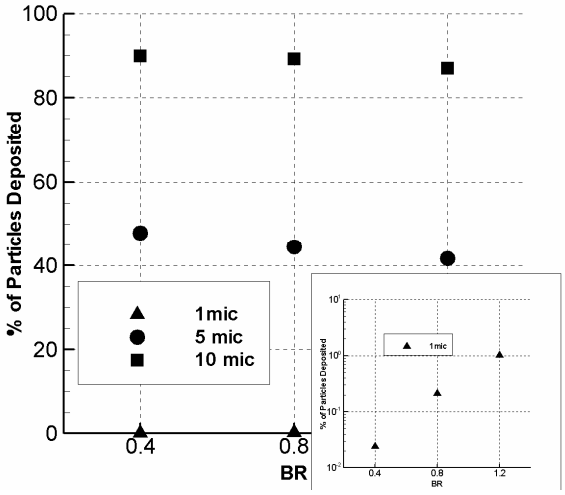

Figure 4.6 - Percentage of deposited particles of each size (#deposited/#injected)

4.4.2 Erosion

In this study, particles with temperatures less than the threshold ST value are assumed to be in a solid state and erode the surface at impingement. Erosion at the surface depends on a number of factors including material characteristics of the surface and particle, impingement velocity, and impingement angle. Characterizing the actual erosion is outside the scope of this paper. Here, the number of particles impacting the surface at a given location, the impact velocity, and impact angle are used to estimate the potential erosive wear by calculating the fraction of incoming particle energy impacting the surface; assuming that on impact all the particle energy is imparted to the surface.

Out of the investigated particle sizes, only the 5 micron particles are found to be erosive on the surface. Both 1 and 10 micron particles only resulted in deposition on the

blade surface as shown earlier. Figure 4.7 shows the surface distribution of 5 micron erosive particles. The contour shows the percentage of erosive particles out of the total number of 5 micron particles in the flow field. The increase of blowing ratio decreases the number of erosive particles by two means: i) stronger coolant jet pushes the particles away from the surface and ii) particles which are drawn to the surface by mainstream entrainment react to the temperature of the entrainment flow which is higher than the coolant core. Therefore the temperature of these particles does not drop below the ST value and they mainly deposit on the aft-side of the jet as shown in Figure 4.3. As a result, with increase in the blowing ratio erosion occurs on the fore-side of the coolant jet, where coolant remains close to the surface.

Figures 4.8 and 4.9 show the impact velocity and angle for 5 micron particles. At the low blowing ratio, the impact angle is a function of the leading edge curvature and decreases downstream of the coolant hole, indicating direct impacts. As blowing ratio increases, the particles impact the surface at much shallower angles on the fore-side due to the entrainment. In all cases, the impact velocity increases downstream of the coolant hole, due to the accelerated flow.

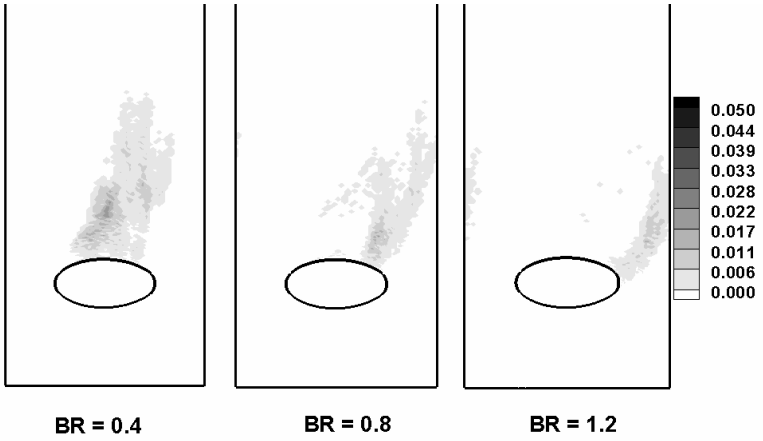

Figure 4.7 - Percentage of 5 micron erosive particle on the surface (out of all 5 micron particles)

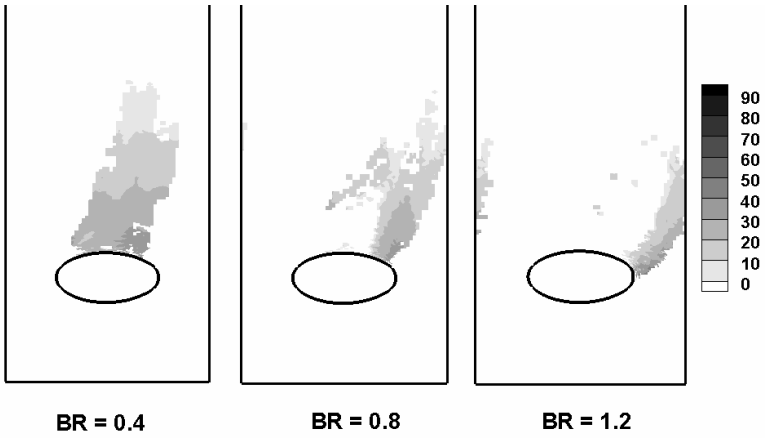

Figure 4.8 - Impact angle of 5 micron erosive particles

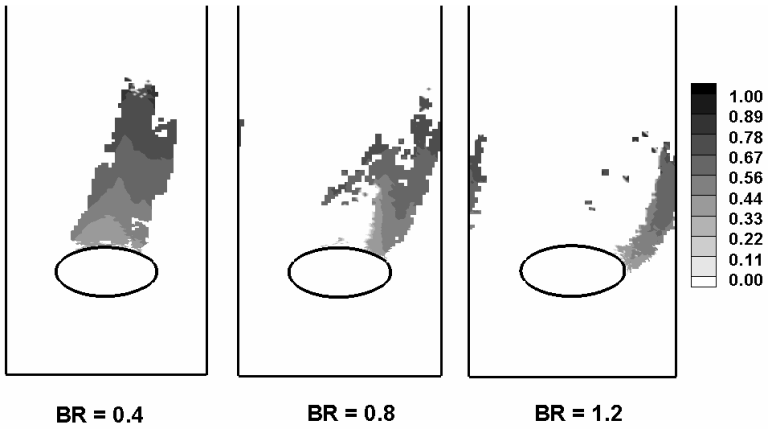

Figure 4.9 - Impact velocity (normalized by u_∞) of 5 micron erosive particles

The 5 micron particles also contribute to the erosive wear inside the coolant hole (Figure 4.10). These particles, on entry in to the coolant jet, have enough residence time to solidify before impacting on the coolant hole walls. Increase in blowing ratio decreases the number of erosive hits, as it did for the deposited particles. This is due to the stronger momentum of the coolant jet which prevents particles with a small momentum Stokes number to enter the coolant hole. The impact angle at lower blowing ratio is slightly higher on the wall facing the flow due to the almost normal impact of the particles which enter the coolant hole from the upstream edge. Some particles which enter the hole are

blown out again and impact the upstream lip of the coolant hole (Figure 4.11). The impact velocities range from 0.10 to 0.4 (Figure 4.12).

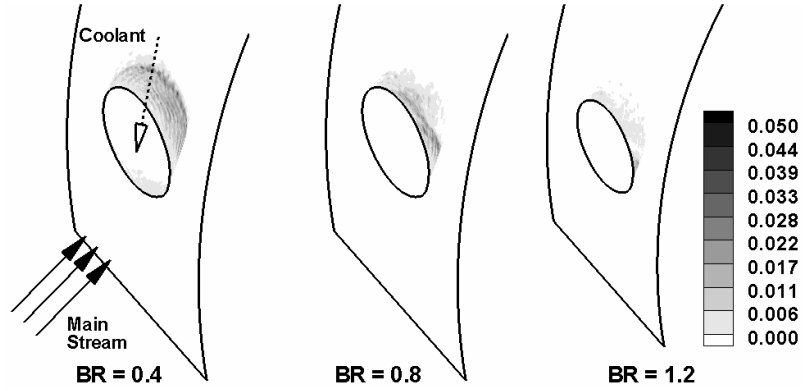

Figure 4.10 - Percentage of 5 micron erosive particle in the coolant hole (out of all 5 micron particles)

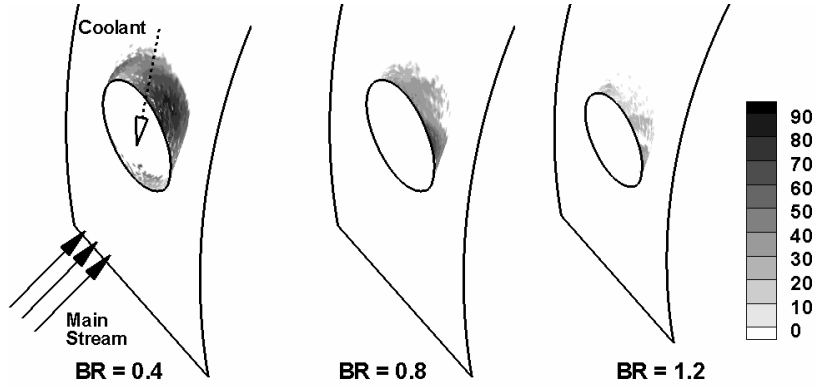

Figure 4.11 - Impact angle of 5 micron erosive particles

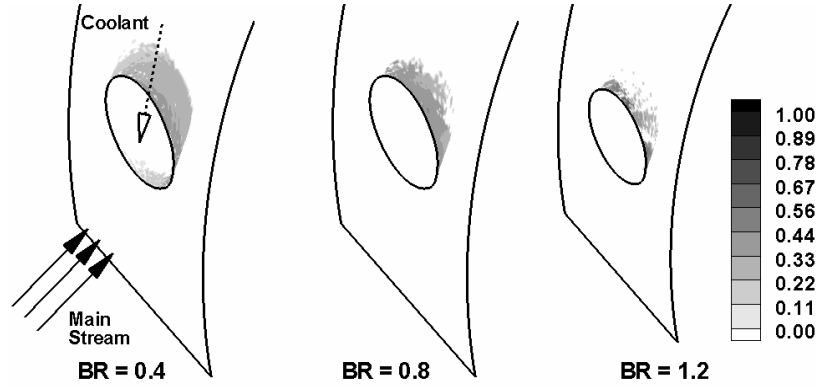

Figure 4.12 - Impact velocity of 5 micron erosive particles

Although the 10 micron particles do not contribute to any erosion on the surface, at BR=1.2, the coolant jet momentum slows a small fraction of 10 micron particles enough to increase their residency time and allowing them to solidify. Due to their large momentum Stokes number, these particles travel further into the coolant hole before they are washed out by the coolant flow. Therefore, unlike the 5 micron particles the effects of these erosive particles are observed at about 1*d* into the coolant hole as shown in Figure 4.13. The impact angle of these particles is also found to be high due to the circulation of these particles inside the coolant hole.

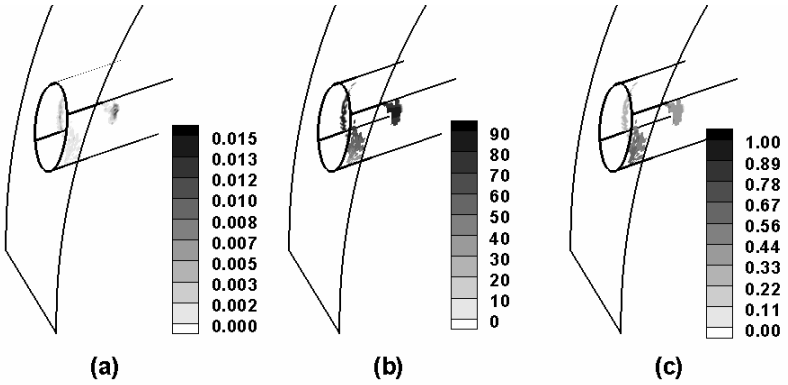

Figure 4.13 - (a) Percentage of 10 micron erosive particle in the coolant hole (out of all 10 micron particles); (b) Impact angle; (c) Impact velocity of at B.R.=1.2

Figure 4.14 illustrates the overall percentage of the erosive particles for 5 and 10 micron particles. As stated before, the percentage of 5 micron erosive particles decreases linearly with an increase in the blowing ratio. Only less than one percent of the 10 micron particles become erosive when they enter into the coolant hole.

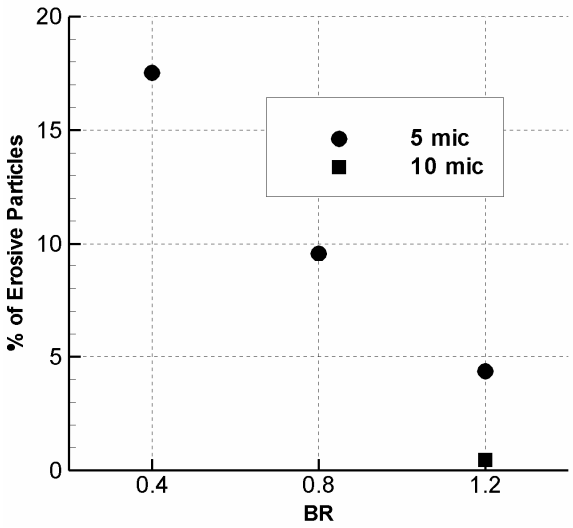

Figure 4.14 - Percentage of erosive particles out of total particles of each size

The Energy Fraction of Erosive Particles (EFEP) is calculated as the kinetic energy of erosive particles that could potentially be transferred to the surface on impact normalized by the total incoming kinetic energy of the particles over all sizes:

$$EFEP = \frac{\sum_{surface} \sum_{time} 1/2 m_{erosive} V_{normal}^2}{\sum 1/2 m_{total} U_\infty^2} \tag{4.6}$$

where V_{normal} is the surface normal component of the impact velocity, and m is the mass of particles.

Table 4.4 illustrates the percentage of EFEP at each blowing ratio. The potential for erosive wear is higher in the coolant hole than on the surface. The potential for erosion is highest in the coolant hole at a B.R.=1.2. This is due to the solidification of the 10 micron particles contain a considerable fraction of the total erosive energy at this B.R [10]. On the surface, erosive wear is mostly caused by 5 micron particles, but is an order of magnitude (or more) smaller than that inside the coolant hole. Overall, surface erosion decreases

[10] *At inflow, particles of 1, 5, and 10 microns account for 0.09, 11.10, and 88.81% of the total energy, respectively.*

with an increase in the blowing ratio except for BR=1.2, where there is a sudden increase in the erosion due to 10 micron erosive particles.

Table 4.4 - Percentage of EFEP.

B.R.	0.4	0.8	1.2
Erosion in the Coolant Hole	0.0228	0.0139	0.0225
Erosion on the Blade Surface	0.0067	0.0026	0.0020
Total Erosion	0.0295	0.0165	0.0245

4.5. Summary

The paper investigates the deposition and erosion caused by Syngas ash particles in a film cooled leading edge region of a representative turbine vane. The carrier phase is predicted using Large Eddy Simulation and three ash particle sizes of 1, 5, and 10 microns are investigated. A threshold ash softening temperature is assumed to determine the state of particles on impact and hence, distinguish between deposition and erosion.

The 1 micron particles with momentum Stokes number St = 0.03 (based on approach velocity and cylinder diameter), follow the flow streamlines around the leading edge and few particles reach the blade surface – only when entrained by the coolant jets. The 10 micron particles, on the other hand with a high Stokes number, St = 3, directly impinge on the surface, with blowing ratios (0.4, 0.8 and 1.2) having a minimal effect. The 5 micron particles with St=0.8, show the largest receptivity to coolant flow and blowing ratio once the particles penetrate into the region of coolant injection.

More than 90% of the injected 10 micron particles deposit on the surface and in the coolant hole upon impact. 1 micron particles, on the other hand, respond to the entrainment on the aft-side of the coolant jet and their rate of deposition increases with increase of the blowing ratio. The deposition of 5 micron particles, on the other hand

decreases with an increase in B.R. On a mass basis, 90% of deposited mass is from 10 micron particles, with 5 micron particles contributing the other 10%, with 1 micron particles making a negligible contribution to deposition. Overall there is a slight decrease in deposited mass with increase in blowing ratio.

Particles which have low thermal inertia or low thermal Stokes numbers cool below the softening temperature and contribute to erosive wear. In this respect, 5 micron particles contribute almost exclusively to erosive wear on the surface and in the coolant hole. While most 1 micron particles are relegated to the outer flow, the larger 10 micron particles with higher thermal inertia result exclusively in deposition on the surface and in the coolant hole. A notable exception is at B.R.=1.2, when 10 micron particles are slowed sufficiently in the coolant hole to allow them to solidify and become erosive. Overall about 0.015-0.03% of the total incoming particle energy can potentially be transferred as erosive energy to the surface and coolant hole, with the contribution coming from only 5 micron particles at B.R. = 0.4 and 0.8, and both 5 and 10 micron particles at B.R.=1.2.

4.6. References

Bons, J.P., Crosby, J., Wammack, J.E., Bentley, B.I., Fletcher, T.H., 2005. "High pressure turbine deposition in land based gas turbines from various Synfuels". ASME paper No. GT2005-68479

Clift, R., Grace, J.R., and Weber, M.E., 1978. "Bubbles, Drops and Particles". Academic Press, New York

Crosby, J., Lewis, S., Bons, J.P., Weiguo, A., Fletcher, T.H., 2007. "Effects of particle size, gas temperature, and metal temperature on high pressure turbine deposition in land based gas turbine from various synfuels". ASME paper No. GT2007-27531

Elgobashi, S., and Truesdell, G.C., "Direct simulation of particle dispersion in a decaying isotropic turbulence", Journal of Fluid Mechanics. 242, 655, 1992.

Hamed, A., 1988. “Effect of particle characteristics on trajectories and blade impact patterns”. Journal of Fluid Engineering, Vol. 110, pp 33-37

Hamed, A., Tabakoff, W., 1994. “Experimental and Numerical Simulation of Ingested Particles in Gas Turbine Engines". AGARD (NATO) 83rd Symposium of Propulsion and Energetics Panel on Turbines, Rotterdam, Netherlands, 25-28 April 1994.

Incropera, F.P., Dewitt, D.P., Bergman, T.L., Lavine, A.S., 2007. “Fundamentals of heat and mass transfer”. Wiley, 6th edition, pp 434

Kaftori, D., Hetsroni, G., and Banerjee, S., “Particle behavior in the turbulent boundary layer. I. Motion, deposition, and entrainment”, Physics of Fluids 7, 1095-1106, 1995

Krishnan, V., Kapat, J.S., Sohn, Y.H., Desai, V.H., 2003. “Effect of film cooling on low temperature hot corrosion in a coal fired gas turbine”. ASME paper No. GT2003-38593

Kulick, J.D., Fessler, J.R., and Eaton, J.K., “Particle response and turbulence modification in fully developed channel flow”, J. Fluid Mech., 277, 109-134, 1994.

Marchioli, C., and Soldati, A., “Mechanisms for particle transfer and segregation in a turbulent boundary layer”, J. Fluid Mech, 468, 283-315, 2002.

McLaughlin, J. B., “Aerosol particle deposition in numerically simulated channel flow.” Physics of Fluids A 1, 1211-1224, 1989.

Metwally, M., Tabakoff, W., Hamed, A., 1995. “Blade erosion in automotive gas turbine engine”. Journal of Engineering for Gas Turbine and Power, Vol.117, pp 213-219

Raubenheimer, D.S.T., 1990. “Selection and operation of gas turbine air filters”. Turbomachinery International, Vol. 31, No. 1, Jan/Feb. Issue, pp 26-33

Rozati, A., Tafti, D.K., 2007a. “Large-eddy simulations of leading edge film cooling: Analysis of flow structures, effectiveness, and heat transfer coefficient”. Intl Journal of Heat and Fluid Flow, *in press*

Rozati, A., Tafti, D.K., 2007b. “Effect of Coolant-Mainstream Blowing Ratio on Leading Edge Film Cooling Flow and Heat Transfer International Journal of Heat and Fluid Flow”. Intl Journal of Heat and Fluid Flow, Accepted for publication

Saffman, P. G., “The lift on a small sphere in a slow shear flow.”, Journal of Fluid Mech. 22, 385-400, 1965

Seggiani M., Pannocchia G., 2003. “Prediction of coal ash thermal properties using partial least squares regression”. Ind. Eng. Chem. Res., Vol. 42, No. 20, pp 4919-4926

Shah, A., Tafti, D.K., 2007. “Transport of particulates in an internal cooling ribbed duct”. Journal of Turbomachinery, Vol. 129, pp 816-825

Shah, A., 2005. “Development and application of a dispersed two-phase flow capability in a general multi-block Navier Stokes solver” MS Thesis, Mech. Eng., Virginia Tech

Smialek, J.L., Archer, F.A., Garlick, R.G., 1992. “The chemistry of Saudi Arabian sand: a deposition problem on helicopter turbine airfoils”. 3rd International SAMPE Metals and Metals Processing Conference, Society for the Advancement of Material and Process Engineering, Vol. 3, pp M63-M77

Sundaram, N., Thole, K.A., 2006. “Effects of surface deposition, hole blockage, and TBC spallation on Vane endwall film-cooling”. ASME paper No. GT2006-90379

Walsh, W.S., Thole, K.A., Joe, C., 2006. “Effects of sand ingestion on the blockage of film-cooling holes”. ASME paper No. GT2006-90067

Wang, Q., Squires, K.D., Chen, M., and McLaughlin, J.B., “On the role of the lift force in turbulence simulations of particle deposition”, International Journal of Multiphase flow 23, 749, 1997.

Wenglarz, R.D., 1985. “Deposition, erosion and corrosion protection for coal-fired gas turbine”. ASME paper No. 85-IGT-61

Appendix

Large Eddy Simulation of Leading Edge Film Cooling

Part-II: Heat Transfer and Effect of Blowing Ratio[11]

Ali Rozati & Danesh K. Tafti

High Performance Computational Fluid-Thermal Sciences and Engineering Lab
Mechanical Engineering Department
Virginia Polytechnic Institute and State University
Blacksburg VA 24061 USA
www.hpcfd.me.vt.edu

Abstract

Detailed investigation of film cooling for a cylindrical leading edge is carried out using Large Eddy Simulation (LES). The paper focuses on the effects of coolant to mainstream blowing ratio on flow features and consequently on the adiabatic effectiveness and heat transfer ratio.

With the advantage of obtaining unique, accurate and dynamic results from LES, the influential coherent structures in the flow are identified. Describing the mechanism of jet-mainstream interaction, it is shown that as the blowing ratio increases, a more turbulent shear layer and stronger mainstream entrainment occur. The combined effects, lead to a lower adiabatic effectiveness and higher heat transfer coefficient. Surface distribution and span-averaged profiles are shown for both adiabatic effectiveness and heat transfer (presented by Frossling number). Results are in good agreement with the experimental data of Ekkad *et al.* [12].

[11] This article was published in Transaction of ASME Turbo Expo 2006, "Large-Eddy Simulations of Leading Edge Film Cooling: Part-II: Heat Transfer and effect of blowing ratio", Rozati, A., Tafti, D.K., Copyright ASME

Nomenclature

A	Area
$B.R.$	Blowing Ratio (u_c/u_∞)
D	Leading edge diameter
d	Coolant hole diameter
L	Coolant hole length to diameter ratio
k	Thermal conductivity
n	Normal wall distance
Nu	Nusselt number
q''	Heat flux
Re	Reynolds number
T	Temperature
u	Cartesian velocity vector/streamwise velocity
w	Wall
x	Stream-wise direction (parallel to the surface)
θ	Nondimensional temperature
η	Adiabatic effectiveness

Subscripts

ad	Adiabatic
b	bulk
c	coolant
∞	free stream

1. Introduction

Detailed knowledge of film cooling flow physics is necessary to improve cooling efficiency. The dynamics of coolant and mainstream mixing are dependent on various factors such as mass flux ratio, mainstream turbulence, angle of injection, and shape of the coolant hole. Among these factors, investigation of the effect of mass flux ratio is not only important to obtain the maximum film cooling effectiveness, but is also essential to determine the minimum amount of coolant flow needed for effective surface protection from hot free stream gases.

Early studies investigated the effects of blowing ratio on flat plate film cooling, such as the experimental study of Honami and Shizawa [1], in which the coolant was laterally injected on a flat plate. Time averaged data of the temperature field was measured on the cross-sectional planes downstream of the coolant hole. This data showed the existence of an asymmetric coolant jet, with mainstream hot gas entrainment occurring from the coolant jet's aft-side. They observed that mainstream entrainment strengthened as the mass flux ratio increased and caused more coolant lift-off from the surface downstream of the coolant hole, resulting in lower effectiveness. Mayhew *et al.* [2] also investigated the effect of blowing ratio on a flat plate with compound angle of injection. Their observations on film cooling effectiveness were similar to that of Honami and Shizawa. They suggested that the asymmetric counter rotating vortex pair governs the enhancement of heat transfer coefficient. In low free stream turbulence, as blowing increased, the counter rotating vortex pair became stronger and augmented the heat transfer coefficient.

In another study on flat plate film cooling with stream-wise coolant injection, Kaszeta and Simon [3] investigated the transport of turbulence by measuring the eddy diffusivity of momentum in the span-wise and cross-stream directions. The primary structure of counter rotating vortex pair appeared to be slightly asymmetric. The cross-stream to span-wise eddy

diffusivity ratio showed values up to 2.5, which indicated an anisotropic flow even for the stream-wise injection. Their results showed that the anisotropy in the turbulent transport is too complex to be modeled by simple anisotropy models such as Bergeles Model of anisotropy [4], although previous studies had shown some success ([5] and [6]).

The experimental set-up of Honami and Shizawa was also simulated by Lakehal *et al.* [7] and they showed that a standard k-ε model could not predict the flow accurately. Namely, it under-predicted the lateral coverage of the coolant and the strength of the vortex pair. A two layer approach was used to resolve the near-wall region with a one-equation model. However, it led to over-prediction of the strength of the vortex pair, while the lateral coverage was still under-predicted. Muldoon and Acharya [8] applied Direct Numerical Simulation method on a flat plate film cooling flow field to compare the exact and modeled turbulent diffusion. The comparison showed that k-ε models tend to over-predict the eddy viscosity. They proposed a damping function to reduce the eddy viscosity.

Understanding the details of flow physics of flat plate film cooling sheds some light on the phenomenon. However, to investigate film cooling physics on the blade leading edge, the geometry should represent the complexity of the region, while maintaining domain simplicity to enable conducting experimental measurements and numerical simulations. A cylindrical leading edge with a flat after-body provides such features. Mouzon *et al.* [9], Yuki *et al*. [10], and Cruse *et al.* [11] used an experimental set-up of a cylindrical leading edge with three rows of film cooling holes placed at stagnation and ±25˚ from the stagnation line to investigate leading edge film cooling. Film cooling adiabatic effectiveness measurements were conducted by [9] and [11] with a coolant to mainstream density ratio of 1.8, and heat transfer measurements by [9] and [10] were conducted at a density ratio of 1.0. Additionally, Mouzon *et al.* used fan-shaped holes in

their study. Despite this difference, results showed that the heat transfer coefficient increased with increase in the blowing ratio for both low and high freestream turbulence. At density ratio of 1.8, adiabatic effectiveness increased with increase of blowing ratio, but the augmentation was not considerable in the presence of high free stream turbulence.

Ekkad *et al.* [12] observed that the jet-mainstream interaction and Frossling number increased with increase of the blowing ratio. Adiabatic effectiveness dropped with an increase in blowing ratio at a density ratio of 1.0. However, as observed in [9] and [11], at a density ratio of 1.5 an increase in blowing ratio increased the effectiveness.

Azzi and Lakehal [13] observed that applying an isotropic k-ε model to predict leading edge film cooling resulted in an exaggerated size of the kidney shape vortex and an under-prediction of the lateral spreading of the coolant. The discrepancies with experimental results grew with an increase of the blowing ratio. This problem arises due to the stronger transport of turbulence in the lateral direction rather than normal to the wall. They improved their results by applying a two layer approach which resolves the near wall region with a one equation DNS based anisotropic model. However, this method required high grid resolution near the surface and therefore their results for the leading edge film cooling were not as satisfactory as the results for flat plate film cooling.

Based on the limitations and inaccuracies in film cooling simulations with RANS models an alternative approach to simulate this phenomenon is Large Eddy Simulation (LES) which resolves the large anisotropic turbulent scales of the flow field while only modeling the smaller isotropic scales. The availability of accurate time-dependent results from LES enables the identification of key elements in the flow physics and their contribution to film cooling efficiency.

2. Objective of the Study

Large Eddy Simulation is proposed to investigate the leading edge film cooling flow. The primary goal is to achieve a thorough understanding of the film cooling dynamics with the temporal resolution provided by LES. In particular, identifying coherent structures and their role in driving the hot gas entrainment is of interest. Since all previous numerical studies at the leading edge have applied RANS models to simulate the flow field, this investigation is the first to report on the dynamic flow structures which are not resolved with the same clarity in steady simulations.

Additionally, the effects of the coolant to mainstream blowing ratio on adiabatic effectiveness and heat transfer are investigated. These effects have been studied experimentally and numerically (using RANS method) before. However, the current work elucidates how the variation in blowing ratio affects the flow features and consequently the adiabatic effectiveness and heat transfer coefficient.

3. Solution Methodology

The governing flow and energy equations are non-dimensionalized by the characteristic length and velocity scales of cylinder diameter (D) and free stream velocity (u_∞), respectively. Characteristic temperatures of (T_∞ -T_c) and $q''_w D/k$ are selected when calculating the adiabatic effectiveness and heat transfer coefficient, respectively. The dynamic Smagorinsky model is used to obtain the eddy viscosity of the subgrid scales. The non-dimensional time dependent Navier-Stokes and energy equations in transformed coordinates are given in [14]. The governing equations of momentum and energy are discretized with a conservative finite volume formulation using a second-order central difference scheme. The temporal advancement is performed with a predictor-corrector algorithm. Detailed information can be found in Tafti [15].

The computational domain is adopted from an experimental study by Ekkad *et.al.* [12], where the leading edge is represented by a cylinder with a tailboard placed at the rear of the cylinder. Rozati and Tafti [14] established that this geometry can be represented by the domain shown in Figure 1, where a symmetry boundary condition is imposed along the stagnation line.

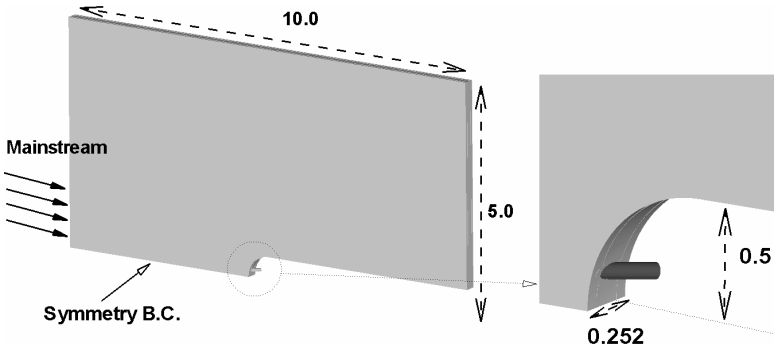

Figure 1. Computational domain

The free stream Reynolds number is 100,000 based on the cylinder diameter, coolant to mainstream blowing ratios are 0.4 and 0.8, and density ratio is unity. In calculations of the adiabatic effectiveness, the non-dimensional temperature of coolant and mainstream are set to zero and unity, respectively. An adiabatic no-slip wall boundary condition is imposed on the surface. Adiabatic effectiveness is defined as:

$$\eta = \frac{T_{ad,w} - T_\infty}{T_c - T_\infty} = 1 - \theta_{ad,w} \qquad \text{(eq. 1)}$$

where ɵ is the non-dimensional temperature:

$$\theta = \frac{T - T_c}{T_\infty - T_c} \qquad \text{(eq. 2)}$$

In calculation of the heat transfer coefficient, both the coolant and mainstream non-dimensional temperatures are set to zero while the blade surface has a constant non-dimensional

heat flux of unity. The local Nusselt number is calculated as the local temperature difference between the surface and reference temperature:

$$Nu = \frac{1}{\theta_i - \theta_{ref}} \qquad \text{(eq. 3)}$$

where the free stream temperature is selected as the reference temperature and $\theta_{ref} = 0.0$.

The coolant pipe inlet boundary condition is provided from an auxiliary fully developed, time dependent, turbulent pipe flow calculation, from which time-dependent profiles of the velocity field are extracted and fed into the coolant pipe inlet. Effects of the coolant inlet velocity profile, accuracy and validity of the auxiliary calculation are given in [14]. The grid contains 62 hybrid structured/unstructured blocks with the total size of 3,211,264 cells. The grid is highly resolved in the vicinity of the coolant hole, coolant pipe and normal to the cylinder blade surface. *a-posteriori* results show that the value of y^+ at the first point from the surface is less than one and adequate numbers of grid points lie within the distance of $0< y^+<10$ [14].

4. Results and Discussion

The calculations are carried out on Virginia Tech's Terascale computing facility, SystemX, on 2.3 GHz PowerPC 970FX processors on 62 processors. The non-dimensional time step is set to 2×10^{-5}. Each time step takes approximately 4.5*s* of wall clock time. The flow is allowed to develop for approximately 3 time units before averaging for time-mean quantities is activated. The results explain the flow physics of film cooling, coherent structures, adiabatic effectiveness and heat transfer coefficients for two blowing ratios of 0.4 and 0.8.

4.1 Coherent structures

The dominant coherent structures for a classical jet in cross flow are: counter-rotating vortex pair in the wake of the jet, horseshoe vortex on the windward side of the jet, and shear layer vortices ([16],[17]). To identify the coherent structures in the present study, the vortex eduction

technique proposed by Chong *et al.*[18] is used. In this method, in regions dominated by vortical motion the velocity gradient tensor exhibits two eigenvalues which are complex conjugate. The magnitude of the eigenvalue is indicative of the strength of the vortex. The structures identified by this method are referred to as "coherent vorticity" in this paper, and the magnitude of the eigenvalue as the strength of the vortices.

The following definition is used to describe the location of flow/structures: in the lateral direction, the side that the jet blows from is specified with prefix "aft" and the side the jet blows to, specified with prefix "fore". In the stream-wise direction along the blade surface, "leeward" is used to denote the downstream side of the jet and "windward" the upstream side of the jet. Figure 2 shows an instantaneous snapshot of coherent vorticity for *B.R.=0.4*. An immediate observation is the complete absence of a horseshoe vortex. This is due to the combination of the low injection ratio and the compound angle injection. Immediately downstream of the coolant hole a low pressure region exists which was shown in [14] and is repeated in Figure 3. The existence of a low pressure region was also observed in a flat plate film cooling study by Muldoon and Acharya [8]. This low pressure region is responsible for creating a strong counter rotating vortex pair which entrains hot mainstream gases underneath the jet. The primary structure forms immediately at the leeward edge of the hole (Figure 2) and is transported downstream to form packets of hairpin vortices. This agrees with the observations of Tyagi and Acharya [16] for a jet in cross flow in a flat plate boundary layer. However, due to the asymmetry of the low pressure region, the strength of these counter rotating vortices is not equal, and the structure at the aft-side of the jet has considerably higher strength and size due to the lateral direction of coolant injection.

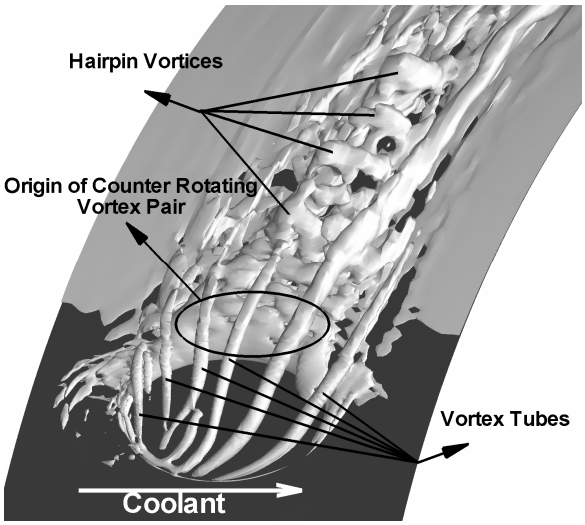

Figure 2. Coherent structures – *B.R. = 0.4* (iso-surface value = 18)

Compared to a classical jet in cross flow, additional structures in the form of vortex tubes appear at the windward side of the jet. They are instabilities produced by the interaction of the transverse jet velocity and the mainstream flow. These vortex tubes originate from the windward side of the coolant hole and bend towards the mainstream direction, on top of the hairpin vortices. It is noted that the vortex tubes are not stationary structures but constantly move fore-to-aft along the windward rim of the hole. Vortex tubes on the top of the coolant jet break down within 1 to 2 diameters downstream of the jet, while the tubes at the aft- and fore-edge of the hole are stronger and directly participate in the jet-mainstream dynamics. One of these tubes is seen to extend at least 6*d* downstream of the jet, aiding the entrainment of hot gases.

Figure 3 compares the size and magnitude of the low pressure region at *x/d*=1.0 downstream of the coolant hole for the two blowing ratios. Contours show the instantaneous distribution of pressure with the same level in coloring. As shown, with an increase of the B.R., the low pressure region is shifted to the fore-side due to higher lateral momentum of the coolant. The

pressure difference within and outside of the coolant core increases drastically at B.R.=*0.8*, which results in much stronger entrainment from the aft-side of the coolant jet.

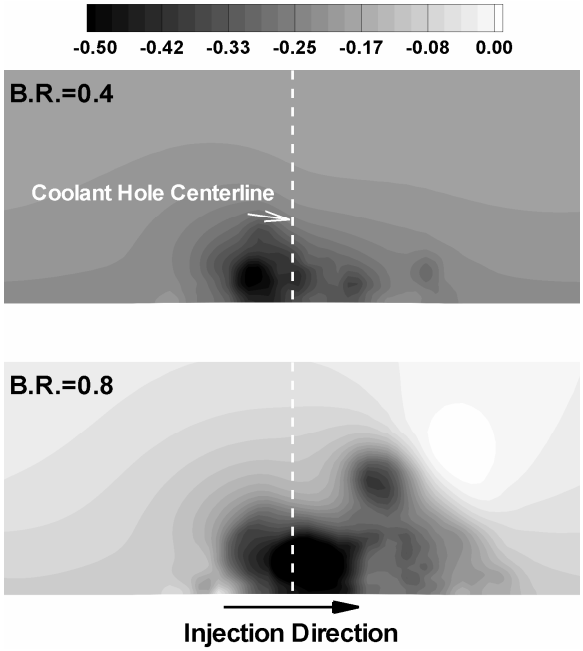

Figure 3. Pressure contour at *x/d* = 1.0 downstream of the coolant hole

A snapshot of the coherent structures at the blowing ratio of 0.8 is shown in Figure 4. The magnitude of the vorticity iso-surface is the same as for Figure 2. An intensified turbulent region with smaller scale eddies is observed at the coolant hole exit. Vortex tubes now originate inside the coolant hole versus at the jet-mainstream interface outside the hole at the low blowing ratio. Contrary to the previous case where the vortex tubes bent towards the surface, at B.R. = *0.8*, vortex tubes do not maintain their steam-wise trajectory. Strong entrainment from the aft-side of the coolant hole disrupts and twists some of the vortex tubes in that direction and the remaining take a hairpin shape and transport downstream of the coolant hole. Contrary to the results at the

lower blowing ratio, vortex tubes do not have any discernible individual effect in entraining hot gases at the aft/fore-side of the coolant jet.

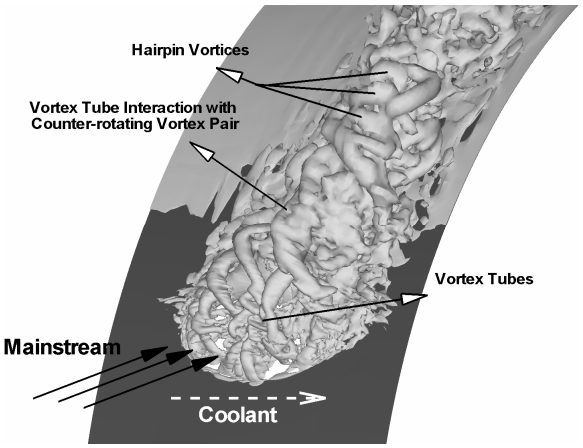

Figure 4. Coherent structures - B.R. = 0.8 (iso-surface value = 18)

4.2 Coolant-mainstream mixing mechanism

Figure 5 explains the jet-mainstream interaction mechanism by means of instantaneous temperature contours and velocity vectors in planes normal to the blade surface and downstream of the jet. At x/d = 1.0, one can identify vortex tubes on the top and sides of the counter-rotating vortex pair. The strength of the main counter-rotating vortex aided by the outer vortex tubes near the aft-side causes the bulk of the hot gas entrainment. As the jet travels downstream (x/d=2.0), the strength of the primary counter rotating vortex decreases. Eventually at x/d = 4.0 the weak component of the counter-rotating vortex pair, at the fore-side of the jet, disappears. As mentioned earlier, vortex tubes travel on the top and sides of the primary vortex structure. The tubes located at the top join with the stronger component of the counter-rotating vortex pair and contribute to entraining hot gas into the coolant from the aft-side. Vortex tubes located at the sides of the primary structure remain intact and separate. At x/d=2.0, the vortex tube on the fore-edge of the coolant is seen to entrain hot gases. The side vortex tubes periodically cause the

coolant flow to break off and join again with the main portion of the coolant jet. Due to the lateral velocity component of the coolant, it is observed that at *x/d* = 6.0 the jet completely shifts to the fore-side.

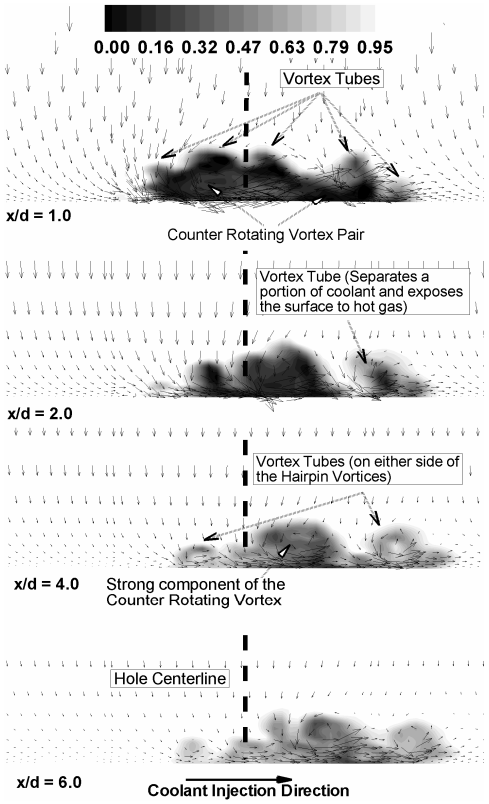

Figure 5. Temperature contour and velocity vectors on cross sectional planes normal to the surface and downstream the hole (B.R.=0.4)

The instantaneous results of temperature contours and velocity vectors are presented at the same cross sectional planes for the blowing ratio of 0.8 (Figure 6). The planes in both Figure 5 and Figure 6 have the same scale in the span-wise and cross-stream directions. One can immediately notice that at the higher blowing ratio coolant jet has a stronger infiltration into the mainstream and stronger shear interaction with the mainstream. The primary vortex is stronger

and larger compared to the same structures (aft component of the counter-rotating vortex) at the lower blowing ratio. As a result a stronger entrainment is observed from the aft-side.

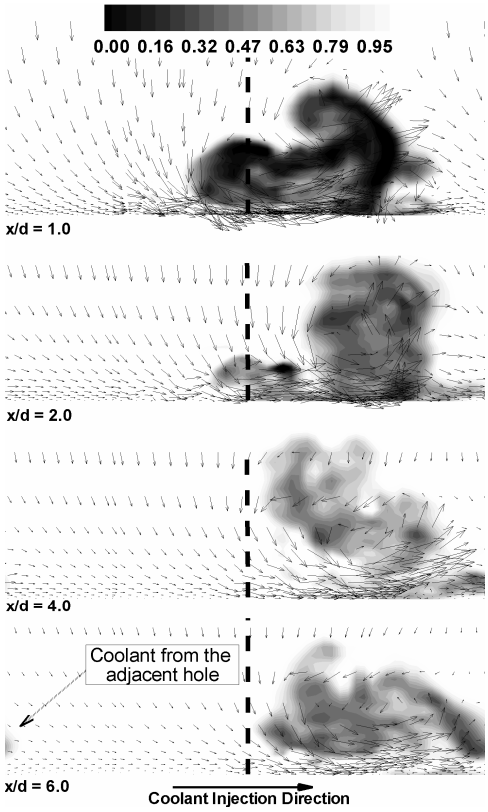

Figure 6. Temperature contour and velocity vectors on cross sectional planes normal to the surface and downstream the hole (B.R.=0.8)

Vortex tubes on the top of the coolant core merge with the primary structure at *x/d* = 2.0. At *x/d* = 4.0 the lateral momentum of the coolant shifts it to the fore-side of the coolant hole completely. Unlike for the lower blowing ratio, the coolant does not remain attached to the surface and at *x/d* = 6.0 it is completely detached from the surface due to the stronger hot mainstream gas entrainment. Stronger shear layer mixing, entrainment of hot gases, and detachment of the coolant results in lower effectiveness of leading edge film cooling at the

higher blowing ratio of 0.8 compared to 0.4. Additionally, due to the coolant jet lift-off from the surface, a narrower span-coverage exists at *x/d*=4.0, and 6.0 downstream of the hole.

4.3 Mean profiles

Figure 7 shows temperature profiles at the hole centerline and downstream of the hole for the two blowing ratios of 0.4 and 0.8. As observed in the previous section, at B.R. = 0.8 and *x/d*=2.0, the higher momentum of the coolant has pushed it to the fore-side of the coolant hole centerline. Therefore the surface temperature on the centerline is close to the mainstream temperature after *x/d*=2.0 downstream of the hole which results in low adiabatic effectiveness on the centerline. A stronger hot gas entrainment can also be observed close to the coolant hole at *x/d*=1.0. The coolant jet penetrates more into the free-stream at the higher blowing ratio with the formation of a thicker thermal boundary layer. Temperature profile at *x/d* =1.0 shows that the core of the coolant is located at the distance of 0.1-0.4*d* from the surface, where the mean temperature of the coolant core is much higher at B.R.=0.8. Temperature profile at *x/d*=1.0 also shows the stronger mixing at the coolant-mainstream shear layer for B.R.=0.8. While at B.R.=0.4 the local minimum at 0.3*d* from the surface is much lower than the local minimum at 0.1*d*, at B.R.=0.8 the two local minimums have almost the same values due to the stronger mixing.

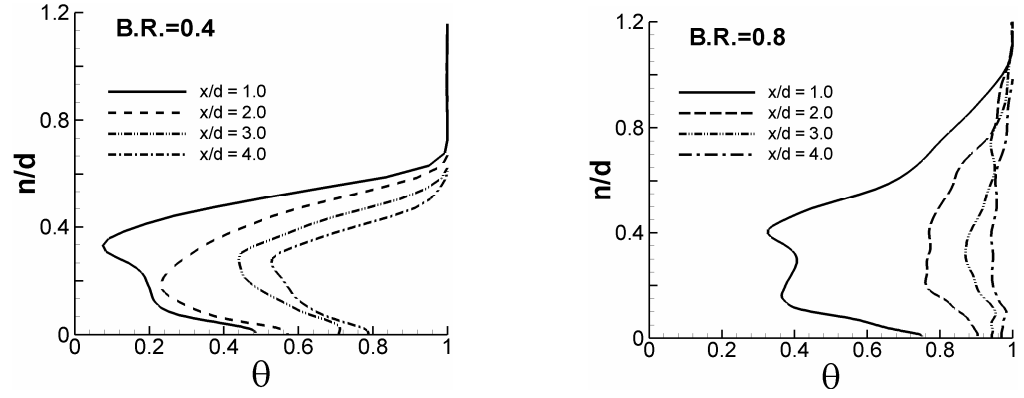

Figure 7. Time averaged temperature profile normal to the wall at jet centerline

4.4 Turbulent statistics and kinetic energy

Turbulent kinetic energy behavior along the stream-wise direction is shown in Figure 8 for both blowing ratios. The distributions are along the hole centerline, normal to the surface and are only shown at five locations downstream of the coolant hole to aid in describing the flow development and identifying the major features of the turbulent field. Compared to the results with B.R.=0.4, the primary noticeable difference at B.R.=0.8 is the significant higher values of T.K.E especially at x/d=1.0 downstream of the coolant hole. At the same location, the thickness of the turbulent layer for B.R.=0.8 is two times larger than that at B.R.=0.4. The highest values of T.K.E. at x/d=1.0 for both cases are located at a normal distance of 0.2d from the wall and are 0.03 and 0.1 for blowing ratios of 0.4 and 0.8, respectively. This peak is caused by the strong interaction of hot mainstream gases with the underbelly of the coolant jet. The peak close to the wall (0.02 and 0.055 at x/d=1.0 for B.R.=0.4 and 0.8, respectively) signals the formation of a turbulent boundary layer and is a result of the strong disturbances created by the lateral entrainment of flow. The merging and interaction of vortex tubes on the top of the primary vortex is responsible for the additional peak in the T.K.E. profile (n/d=0.45 and 0.6 for B.R.=0.4 and 0.8, respectively).

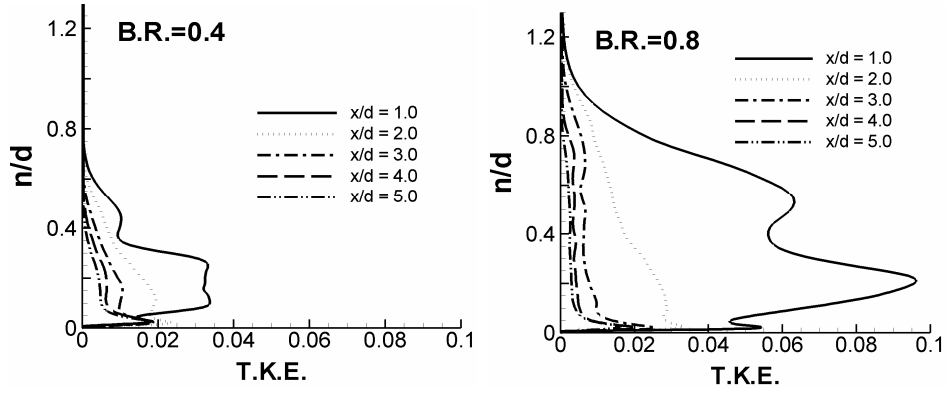

Figure 8. T.K.E profile normal to the wall at jet centerline

The low values of T.K.E. further downstream for B.R. = 0.8, are a result of the coolant core shifting to the fore-side of the centerline. However, in spite of this shift, a turbulent boundary layer is clearly represented in the profile very close to the surface, as it is for the lower blowing ratio.

4.5 Adiabatic Effectiveness

Figure 9 compares the distribution of adiabatic effectiveness at the two blowing ratios of 0.4 and 0.8. While at B.R.=0.4 a portion of the coolant remains attached at the fore-side and leeward rim of the coolant hole, at higher B.R.=0.8 it does not, due to a combination of increased mixing and jet lift-off. At low blowing ratio, mainstream momentum is much stronger than the coolant momentum and pushes the coolant towards the surface immediately downstream of the coolant hole. At higher blowing ratio, stronger momentum of the coolant causes more mixing with the mainstream and stronger entrainment of hot gases as discussed earlier. This entrainment eventually detaches the coolant from the surface and causes a narrower coverage of the coolant on the surface at B.R=0.8. Also, the stronger lateral-momentum of the coolant shifts it further to the fore-side when compared to the lower blowing ratio.

As expected the span-wise average adiabatic effectiveness decreases as the blowing ratio increases (Figure 10). Results at higher blowing ratio shows some discrepancies with the experimental data especially far downstream of the coolant hole (x/d=6-7). The experimental data show an increase in the adiabatic effectiveness at these locations. However, considering the experimental uncertainty of ±6.8 percent for the film cooling effectiveness measurements, and the unavailability of the jet inlet conditions in the experiments, the results show acceptable agreement at both blowing ratios.

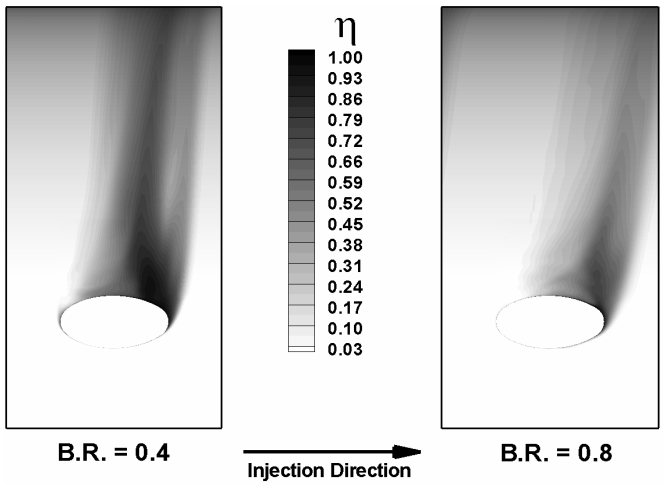

Figure 9. Surface distribution of adiabatic effectiveness

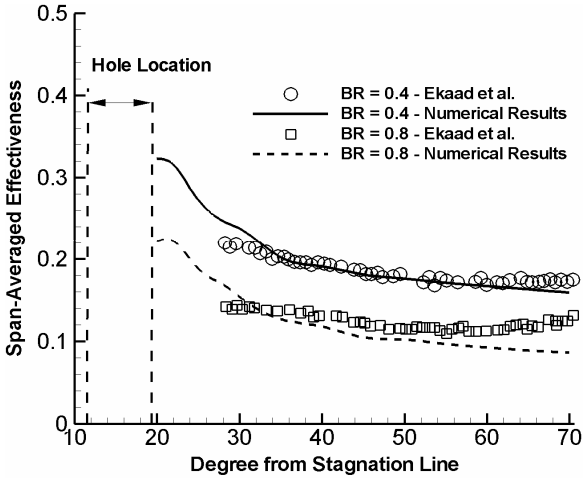

Figure 10. Span-wise averaged adiabatic effectiveness distribution

4.6 Heat transfer coefficient

Surface distribution of the Frossling number (Figure 11) shows that for both blowing ratios a small region with high heat transfer is located at the fore-side of the coolant hole rim. At B.R=0.4, the counter-rotating vortex pair and vortex tubes create high heat transfer regions at the fore- and aft-sides of the coolant hole centerline. At B.R.=0.8, the extent of the high heat transfer region is increased due to the stronger coherent structures, stronger entrainment and jet-

mainstream interaction, which lead to higher T.K.E. near the surface. In particular, compared to the lower blowing ratio, higher values of Frossling number are observed at the aft-side and close to the coolant hole. This is the direct effect of stronger entrainment of hot mainstream gases underneath the coolant at this location as illustrated before.

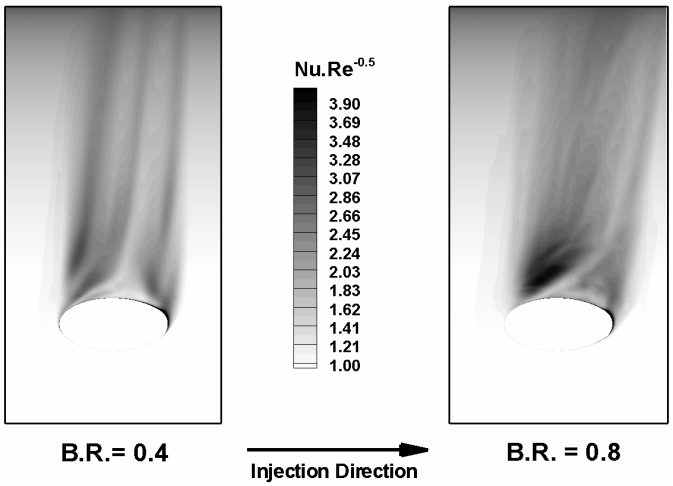

Figure 11. Surface distribution of the Frossling number

The span-wise averaged Frossling number distribution (Figure 12) shows good agreement with the experimental data (with ±4.5% uncertainty in heat transfer coefficient measurement). The heat transfer coefficient decreases downstream of injection due to the weakening of the coherent structures and the decay of near-wall turbulent intensities. An increase in blowing ratio enhances the heat transfer coefficient.

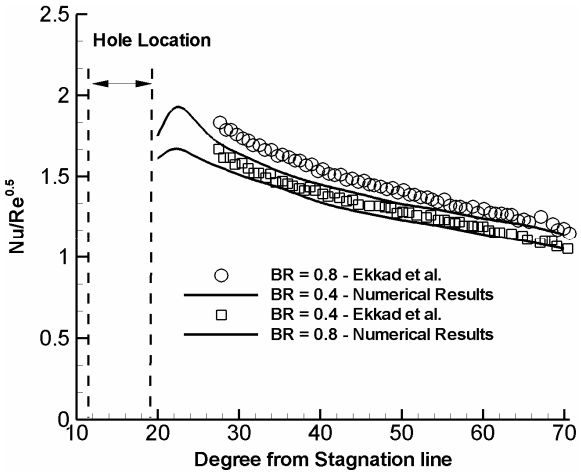

Figure 12. Span-wise averaged Frossling number distribution

5. Summary and Conclusions

LES is used to investigate leading edge film cooling for two blowing ratios. For both blowing ratios, hot mainstream gases entrain underneath the coolant from the aft-side of the coolant jet. However, this entrainment is much stronger at the higher B.R.=0.8, considered in this study. Unlike for B.R.=0.4, where the coolant remains attached to the surface, at B.R.=0.8 the larger momentum and strong entrainment of the hot mainstream gases underneath the coolant detaches it from the surface at x/d=4.0. The higher lateral momentum of the coolant shifts it to the fore-side of the hole centerline as the coolant reaches x/d=2.0. Due to the stronger ejection from the hole at B.R.=0.8, the coolant penetrates further into the mainstream.

Coherent structures are identified for both blowing ratios. At B.R.=0.4, three types of structures are identified. An asymmetric counter-rotating vortex pair forms at the leeward rim of the coolant hole due to the existence of a low pressure region. The aft-side component of this vortex pair is significantly stronger than the other component and dominants the jet-mainstream interaction further downstream of the hole. The vortex pair transport downstream in the form of

packet of hairpin vortices. At the windward rim of the hole, vortex tubes form as a result of the transverse velocity of the coolant and its interaction with the mainstream flow. The momentum of the mainstream flow bends these vortex tubes towards the counter-rotating vortex. A number of vortex tubes extend only 1.0-2.0*d* downstream of the hole. However, the vortex tubes on the fore and aft-side of the hole have an individual effect on entraining mainstream hot gases. At B.R.=0.8, vortex tubes exhibit a different behavior as they are drawn towards and merge with the strong primary vortex immediately downstream of the coolant hole. Additionally, the origin of these vortices – which have smaller scales compared to B.R.=0.4 - is from the entire surface of the coolant hole instead of only the windward rim.

At B.R.=0.8, mixing of coolant with mainstream increases due to stronger entrainment and higher values of T.K.E. in the jet-mainstream interaction region. T.K.E profile at the coolant hole centerline and 1.0*d* downstream of the hole shows peaks of 3% and 10% for blowing ratios of 0.4 and 0.8, respectively. The thickness of the turbulent boundary layer increases from 0.6*d* to 1.2*d* as well, with an increase in blowing ratio.

As a result, the averaged values of effectiveness decrease and the span-coverage of the coolant becomes narrower with an increase in the blowing ratio. Unlike the effectiveness, the span-wise average values and surface distribution of the Frossling number increases as the blowing ratio increases. The highest values of Frossling numbers are observed at the immediate downstream aft-side of the coolant jet due to the strong mainstream entrainment.

6. References

1. Honami, S., Shizawa, T., 1992. “Behavior of the laterally injected jet in film cooling: measurement of surface temperature and velocity/temperature field within the jet”. ASME paper No. 92-GT-180
2. Mayhew, J.E., Baughn, J.W., Byerley, A.R., 2004. “ The effect of free stream turbulence on film cooling heat transfer coefficient and adiabatic effectiveness using compound angle holes”. ASME paper No. GT2004-53230
3. Kaszeta, R.W., Simon, T.W., 2000. “Measurement of eddy diffusivity in film cooling flows with stream-wise injection”. *Journal of Turbomachinery*, Vol. 122, pp 178-183
4. Bergeles, G., Gosman, A.D., Launder, B.E., 1978. “The turbulent jet in a cross stream at low injection rates: a three-dimensional numerical treatment”. *Numerical Heat Transfer*, Vol. 1, pp 217-242
5. Sathyamurthy, P., Patankar, S.V., 1992. “Film cooling studies using a three-dimensional parabolic procedure”. *University of Minnesota* Supercomputer Institute Research Report 92/44
6. Xu, J.Z., Ko, S.Y., Chen, S.J., Tsou, F.K., 1990. “Computer simulation of film cooling with coolants from one and two rows of holes”. ASME paper No. 90-WA/HT-7
7. Lakehal, D., Theodoridis, G.S., Rodi, W., 1998. “Computation of film cooling of a flat plate by lateral injection from a row of holes”. *International Journal of Heat and Fluid Flow*, No. 19, pp 418-430
8. Muldoon, F., Acharya, S., 2004. “Direct numerical simulation of a film cooling jet”. ASME paper No. GT2004-53502
9. Mouzon, B.D., Albert, J.E., Terrell, E.J., Bogard, D.G., 2005. “Net heat flux reduction and overall effectiveness for a turbine blade leading edge”. ASME paper No. GT2005-69002

10. Yuki, U.M., Bogard, D.G., Cutbirth, J.M., 1998. “Effect of coolant injection on heat transfer for a simulated turbine airfoil leading edge”. ASME paper No. 98-GT-431
11. Cruse, M.W., Yuki, U.M., Bogard, D.G., 1997. “Investigation of various parametric influences on leading edge film cooling”. ASME paper No. 97-GT-296
12. Ekkad, S.V., Han, J.C., Du, H., 1998. “Detailed film cooling measurement on a cylindrical leading edge model: effect of free-stream turbulence and coolant density”. *Journal of Turbomachinery*, Vol. 120, pp 799-807
13. Azzi, A., Lakehal, D., 2001. “Perspective in modeling film cooling of turbine blades by transcending conventional two-equation turbulence model”. Proceedings of IMECE’01, November 11-16, 2001, New York, NY
14. Rozati, A., Tafti, D.K., 2007. “Large eddy simulation of leading edge film cooling part-I: computational domain and effect of coolant inlet condition”. ASME paper No. GT2007-27689
15. Tafti, D.K., 2001. “GenIDLEST – A scaleable parallel computational tool for simulating complex turbulent flows”. Proc. ASME Fluid Engineering Division, FED-vol. 256, ASME-IMECE, New York, 2001
16. Tyagi, M., Acharya, S., 2003. “Large eddy simulation of film cooling flow from an inclined cylindrical jet”. *Journal of Turbomachinery*, Vol. 125, pp 734-742
17. Iourokina, I.V., Lele, S.K., 2005. “Towards large eddy simulation of film cooling flows on a model turbine blade leading edge”. 43rd AIAA Aerospace Science Meeting and Exhibit, 10-13 January 2005, Reno, Nevada
18. Chong, M.S, Perry, A.E., Cantwell, B.J., 1990. “A general classification of three dimensional flow fields”. *Phys. Fluids A*, Vol. 2, No. 5, pp. 765-777